



(Zweitgutachter)

(Erstgutachter/Betreuer)

Current Transport in Polycrystalline Iron Based Superconductors

DISSERTATION

zur der Erlangung des akademischen Grades
Doktor der technischen Wissenschaften

eingereicht von

Dipl.-Ing. Johannes Matthias Hecher

Matrikelnummer: 0625419

eingereicht an der Fakultät für Physik der Technischen Universität Wien

unter Leitung von:

Privatdoz. Dipl.-Ing. Dr.techn. Michael Eisterer

Wien, am 24. März 2016

Abstract

The grain boundaries in polycrystalline high-temperature superconductors have intrinsic properties that limit the current flow from one grain to another. This so-called weak-link behavior is also present in iron based superconductors, but the limitations are less severe compared to other high temperature superconductors.

The motivation for the investigation of iron based superconductors is the low costs of the materials and the relative easy synthesis, which gives them a big economical advantage. In order to improve the properties of superconducting wires and tapes a deeper understanding of the involved physics of grain boundaries is necessary. The primary aim of this work was the clarification of the current transport mechanisms in polycrystalline superconductors, where two currents can be distinguished: the intra-grain current flowing within the individual grains and the inter-grain current that crosses the grain boundaries.

These currents were investigated theoretically and by various experimental techniques, including standard and advanced magnetization measurements. A scanning Hall-probe microscope was build, that enables the visualization of the inter- and intra-grain current densities. It can operated in the temperature range from 2.5 to 150 K and magnetic fields up to 8 T. The spatial resolution of the set-up is about 1 μm which is complemented by a scan range of $3 \times 3 \text{ mm}^2$. In addition to these measurement techniques, some samples were irradiated with fast neutrons in the research reactor of the *Atomintitut*. Neutron irradiation enhances the pinning within the grains. The resulting changes after the irradiation allow the validation of theoretical considerations.

Optimally doped $(\text{Ba}_{1-x}\text{K}_x)\text{Fe}_2\text{As}_2$ and $\text{Ba}(\text{Fe}_{1-x}\text{Co}_x)_2\text{As}_2$ bulks were characterized to understand the underlying mechanism of the current flow in polycrystalline iron based superconductors. Thereby, the grain size was varied systematically from about 100 nm to approximately 5 μm (radius of grains). The magnetization, transport current, and scanning Hall-probe microscope measurements offered direct evidence of a higher inter-grain current density when the absolute value of the external applied field was decreased compared to increasing fields. This hysteresis of the inter-grain current density became more pronounced in the samples with smaller grains, which was accompanied by a reduced field dependence. The reduced field dependence corresponds to a larger current density at all fields. The maximum inter-grain current density was found to increase with decreasing grain size.

The inter- and intra-grain currents were describable by the critical state model and together with an elementary field distribution model for weakly linked polycrystals the inter- and the intra-grain currents could be evaluated quantitatively from scanning Hall-probe microscope measurements.

A model was developed to account for the observed results. It uses basic assumptions on the inter-grain current density across the grain boundaries and the reversible and irreversible currents inside the grains, as well as a statistical averaging of the grain size distribution in a sample. This model extends the equations of a Josephson junction to weakly linked polycrystals and is able to explain the larger inter-grain current density in decreasing fields and its reduced field dependence in materials with smaller grains.

The good agreement between the model and multiple experiments supports its validity and points to a parameter that can help to increase the operable field range of BaFe_2As_2 wires—the grain size. The experiments confirmed the predictions of the model, that the field dependence of the inter-grain current density can be significantly reduced by reducing the grain size. This prediction is not limited to the investigated iron based superconductors and may be of interest for other high-temperature superconductors. Furthermore, the good agreement between model and experiments shows, that polycrystalline BaFe_2As_2 bulks are governed by the physics of Josephson junctions.

Kurzfassung

Die intrinsischen Eigenschaften einer Korngrenzen in polykristallinen Hochtemperatursupraleiter begrenzen den Strom der von einem Korn zum nächsten fließen kann. Sie wird deshalb auch als „weak-link“ (zu deutsch: schwache gekoppelte Verbindung) bezeichnet. Dieses Verhalten der Korngrenzen wurde auch in Eisen basierten Supraleiter nachgewiesen, allerdings scheint die Limitierung dort weniger stark zu sein als in anderen Hochtemperatursupraleiter.

Die Weiterentwicklung von Eisen basierten, supraleitenden Drähten ist vor allem wegen der geringen Materialkosten und der vergleichsweise einfachen Synthesisierung interessant. Jedoch ist ein tieferes Verständnis der involvierten Physik von Nöten um deren Eigenschaften weiter verbessern zu können. Das vorrangige Ziel dieser Arbeit war die Untersuchung des Stromtransportes in polykristallinen Supraleiter, welcher im wesentlichen von zwei Strömen bestimmt wird: dem Intra-Korn-Strom, der in den einzelnen Körnern fließt und dem Inter-Korn-Strom, der von einem Korn zum nächsten fließt.

Diese Ströme wurden in dieser Arbeit theoretisch und mittels verschiedenster Messmethoden untersucht. Unter anderem wurden Standardmessverfahren und fortgeschrittene Messtechniken verwendet um die magnetischen Beiträge von Inter- und Intra-Korn-Ström zu separieren. Weiters wurde ein „scanning Hall-probe microscope“ entwickelt, um den Stromtransport zu visualisieren. Das Instrument ist in der Lage, Temperaturen im Bereich von 2.5 bis 150 K und in magnetische Felder von bis zu 8 T zu messen. Die räumliche Auflösung beträgt 1 μm und der maximale Messbereich $3 \times 3 \text{ mm}^2$. Zusätzlich wurde der Einfluss von Neutronenbestrahlung auf die Proben untersucht. Die Bestrahlung wurde am Forschungsreaktor des *Atomintituts* durchgeführt. Schnelle Neutronen verursachen Defekte im Kristallgitter und sind in der Lage das „pinning“ (zu deutsch: die Verankerung) in den Körnern zu erhöhen. Deshalb erlauben solche Experimente Rückschlüsse oder Bestätigungen von Modellen und deren Voraussagen.

Co und K dotierte Ba-122 Proben wurden charakterisiert um die grundlegenden Mechanismen des Stromtransportes in polykristallinen, Eisen basierten Supraleiter zu untersuchen. Dabei wurden Proben mit systematisch veränderten mittleren Korngröße zwischen 100 nm und 5 μm untersucht. Mithilfe von Magnetisierungs-, Transport- und scanning Hall-probe microscope Messungen konnte beobachtet werden, dass ein größerer Inter-Korn-Strom fließt wenn der Absolutwert des extern angelegten Felds reduziert wird, als wenn er erhöht wird. Diese Hysterese nimmt zu, je kleiner die Körner der Proben sind. Mit der Zunahme der Hysterese reduziert sich auch die Feldabhängigkeit des Inter-Korn-Stroms über den gesamten Feldbereich. Zusätzlich steigt die maximalen Stromdichte mit abnehmenden Korndurchmesser.

Mithilfe bereits bekannter Modelle und zusätzlichen Annahmen für die Feldverteilung schwach gekoppelter polykristalliner Proben, konnten die Inter- und Intra-Korn-Ströme in scanning Hall-probe microscope Messungen quantitativ ausgewertet werden. Die daraus resultierenden Daten wurden mit einem Modell beschrieben, welches auf grundlegenden Annahmen des Stromtransportes über eine Korngrenze und der statistischen Verteilung der Korngröße basiert. Dieses Modell erweitert die Gleichungen die eine einzelne Josephson-Verbindung beschreiben auf Polykristalle mit schwach gekoppelte Körnern. Es ist in der Lage die unterschiedlichen Werte des Intra-Korn-Stroms und die reduzierte Feldabhängigkeit mit abnehmender Korngröße zu erklären. Die gute Übereinstimmung von Modell und Experimenten unterstützt seine Richtigkeit und deutet auf eine Größe die helfen könnte den Feldbereich, in dem Drähte aus Eisen basierte Supraleiter verwendet werden können, zu vergrößern – die Korngröße. Die Experimente bestätigten die Voraussage, dass die Feldabhängigkeit des Inter-Korn-Stroms reduziert wird, wenn die Korngröße reduziert wird. Diese Vorhersage ist dabei nicht auf die untersuchten Eisen basierte Supraleiter beschränkt, sondern kann potentiell auf alle schwach gekoppelten Polykristalle angewandt werden. Die gute Übereinstimmung von Modell und Messungen zeigt auch, dass der Stromtransport in polykristallinen Ba-122 Supraleiter durch den Mechanismus der Josephson-Kopplung beschrieben wird.

Acknowledgments

I want to thank:

Jeremy Weiss and Yujiro Hayashi for synthesizing the samples. Additionally, I want to thank Jeremy Weiss for providing data on transport current measurements on a K doped Ba-122 wire and images of the samples surfaces.

Thomas Cervinka for measurements on the Co doped samples.

My colleagues Thomas Baumgartner, David Fischer, Mayraluna Lao, Ventsislav Mishev, Wolfgang Seeböck, and Martin Zehetmayer for their help.

Michael Eisterer for the supervision of my work.

My friends Andreas Fuchs, Wilfried Mach, Robert Raab, and Tobias Rechberger.

And my family.

Contents

Explanation of Acronyms	xi
1 Introduction	1
1.1 Iron Based Superconductors	2
1.2 Grain Boundaries	3
1.3 Granularity and Current Transport	4
1.4 Motivation and Outline of Thesis	6
References	7
2 Samples and Experiments	11
2.1 Samples	11
2.1.1 Grain Size Distribution	12
2.2 Magnetization Experiments	14
2.2.1 Magnetization Loops	17
2.2.2 Residual Magnetization	18
2.3 Scanning Hall-Probe Microscope	19
2.3.1 Set-Up	20
2.3.2 Distance	22
2.3.3 Magnetic Impurities	23
2.3.4 An Exemplary Measurement	24
References	26
3 Modeling Intra-Grain Currents	27
3.1 Crystals	27
3.1.1 Reversible Properties	28
3.1.2 Irreversible Properties	29
3.2 Polycrystals	30
3.2.1 Reversible Properties	32
3.2.2 Irreversible Properties	33
References	34
4 Modeling Inter-Grain Currents	37
4.1 Josephson Junction	37
4.1.1 Josephson Current Density	38
4.1.2 Ginzburg-Landau Phase	39
4.1.3 Model of Svistunov and D'yachenko	40
4.1.4 Maximum Josephson Current Density	41
4.1.5 Fluctuations in the Josephson Junction	42
4.2 Extension to Polycrystals	44
4.3 Discussion of the Model	45
4.4 Modification of the Critical State	49

4.4.1	Field Profile	49
4.4.2	Magnetization and Currents	50
4.4.3	Residual Magnetization	52
	References	55
5	Modeling Field Profiles	57
5.1	Discretization	57
5.2	Polycrystals	60
6	Experimental Results and Discussion	63
6.1	Saturated Field Profile	64
6.1.1	Hysteresis of the Inter-Grain Current Density	64
6.1.2	Temperature Dependence	66
6.1.3	Scanning Hall-Probe Microscopy	67
6.2	Developing and Reverse Field Profiles	70
6.2.1	Characteristic Fields	70
6.2.2	Scanning Hall-Probe Microscopy	72
6.2.3	Small and Large Grained Samples	77
6.3	Residual Field Profile	78
6.3.1	Magnetization Loops	78
6.3.2	Residual Magnetization	79
6.3.3	Small and Large Grained Samples	83
6.4	Behavior of the Intra-Grain Current Density	84
6.5	Neutron Irradiation	84
6.6	Summary	86
	References	87
7	Conclusions and Outlook	89
	Bibliography	91
	Books	91
	Articles	91

List of Figures

1.1	Crystallographic structure of BaFe ₂ As ₂ and the (simplified) phase diagram with the superconducting dome (SC) and the antiferromagnetic regime (AF) for Co and K doping.	2
1.2	Examples for the grain boundary (GB) misalignment commonly encountered in polycrystalline bulks and thin films.	4
1.3	Sketch of the hysteresis of the inter-grain current density (J_c), the definition of the increasing and decreasing field branches in the respective quadrants of a magnetization measurement, and the commonly accepted explanation for the hysteresis of J_c based on the return field (H_{return}).	5
2.1	Images of the surface of the medium and large grained K doped samples (provided by J. D. Weiss) and the respective distribution densities, which were fitted by equation (2.1).	13
2.2	Hysteresis of the magnetic field inside a superconductor in dependence of an external applied field (H_{ext}) and the corresponding magnetization (M) for the critical state model and the extended critical state model, where the inter-grain current density (J_c) is field dependent. The vertical dotted lines in the left plots define the sample edges.	14
2.3	Graphical introduction of the terms defined in the text. The graphs show the development of Spatial variation of the magnetic field.s (field profiles) inside a superconducting crystal in dependence of an external applied field (H_{ext}) and the maximum applied field (H^{max}).	15
2.4	Magnetization loops (M) corresponding to the field profiles in the developing and reverse state. The dotted curve in A represents the field dependence of the magnetization of Field profile of a sample, when the global current and the currents in the grains have the same orientation. (saturated field profile), while the vertical dotted lines in B and C define the sample edges.	17
2.5	Approach and the typical visualization of the results of the measurement of the residual magnetization (M_{res}) for the critical state (J_c) and the extended critical state model ($J_c(H)$). M_{max} represents the magnetization recorded at the maximum additional applied field ($H_{\text{add}}^{\text{max}}$).	19
2.6	Setup of the scanning Hall-probe microscope.	21
2.7	Position dependence of the Wheatstone bridge circuit voltage (left axes) and the magnetic field above the center of the medium grained sample (right axes). Inter-grain current density (J_c) is dominant in A, because the measurement was conducted for a saturated field profile on the Field branch, in which the absolute value of the external applied field is decreasing. (decreasing field branch) at 0.03 T and 5 K. In contrast to this, the measurement in B shows the z -dependence of the field at one point above a saturated field profile on the Field branch, in which the absolute value of the external applied field is increasing. (increasing field branch) at 0.17 T, where the contributions of the intra-grain current density (J_{intra}) are dominant.	22
2.8	Scan of an area in close proximity to the surface near the center of the medium grained sample and a line scans of the same sample with varying distance to the surface. The measurements were carried out at 5 K and the external applied field was ramped from -0.15 to 0.15 T, where the measurements were carried out. H_{mean} in A is the mean value of all data points.	24
2.9	scanning Hall-probe microscope measurement of a niobium thin-film used to trap Rubidium atoms. The rectangle in the large area scan indicates the scan area shown in the more	

detailed scan. The field distribution above the film is compared to the distribution of the trapped atoms in C. (The image titled „trapped atoms“ was provided by F. Diorico and S. Minniberger.)	25
3.1 Comparison of the reversible magnetization (M_{rev}) of type-I and type-II superconductors and the M_{rev} of type-II materials for different κ	28
3.2 Two dimensional and one dimensional field profile above a square crystal, that originates from the reversible magnetization. The dashed line in A represent the position where the magnetic field is zero and the horizontal line indicates the position of the line plotted in B.	29
3.3 Two dimensional and one dimensional field profile corresponding to the irreversible current density of a crystal, similar to figure 3.2.	30
3.4 Magnetic induction (B) inside the sample and the graphical definition of the weighting function $g(\delta)$	31
3.5 Numerically calculated global response of the magnetization originating from the representative reversible intra-grain current density ($M_{\text{rev}}^{\text{G}}$) in a polycrystalline sample with a constant inter-grain current density (J_c) and the change in the residual reversible magnetization of the grains ($M_{\text{res,rev}}^{\text{G}}$) at different background fields (H_{bg}).	32
3.6 Connection of the formation of the inter- and Global field profile that is generated by the grains of a polycrystal.s (intra-grain field profiles) in a polycrystalline cylinder.	33
3.7 Residual magnetic signal of the irreversible contributions of figure 3.6 and a comparison of the global response of the residual magnetization originating from all irreversible contributions of the grains ($M_{\text{res,irr}}^{\text{G}}$) in a polycrystalline sample in dependence of inter-grain current density (J_c).	34
4.1 Visualization of the coordinate system used to model the Josephson current density across a grain boundary (GB).	38
4.2 Superposition of the reversible (representative reversible intra-grain current density ($J_{\text{rev}}^{\text{G}}$)) and irreversible contributions (representative irreversible intra-grain current density ($J_{\text{irr}}^{\text{G}}$)) to the intra-grain current density (representative intra-grain current density (J^{G})), where $J_{\text{rev}}^{\text{G}}$ was calculated with equation (3.7) and $J_{\text{irr}}^{\text{G}}$ with equation (2.9).	41
4.3 The interference pattern of the maximum Josephson current density ($J_{\text{J,max}}$) resulting from a magnetic field. Panel A shows the result of equation (4.19). The other panels visualize the current flow inside the junction, where the text boxes refer to the applied magnetic flux (ϕ) and the arrows inside the junction denote the direction of the current flow as a function of y	43
4.4 Modification of the undisturbed maximum Josephson current density ($J_{\text{J,max}}$) by fluctuations of the properties in the junction.	44
4.5 Modeling of the grain size distribution. Examples for the slices through a grain that may be detected at the sample surface and a sketch of the inter-grain current flow in a polycrystal. The distribution density function defined by equation (2.1) is used to fit the grain size distribution density.	45
4.6 Simplified history dependence of the representative intra-grain current density (J^{G}) according to equation (4.15) for different ratios between the representative reversible intra-grain current density ($J_{\text{rev}}^{\text{G}}$) and the representative irreversible intra-grain current density ($J_{\text{irr}}^{\text{G}}$) ($ J_{\text{rev}}^{\text{G}} < J_{\text{irr}}^{\text{G}} $ top panel and $ J_{\text{rev}}^{\text{G}} > J_{\text{irr}}^{\text{G}} $ middle panel), and the impact on the inter-grain current density (J_c), as defined by equation (4.21) (bottom panel).	46
4.7 Dependence of the inter-grain current density (J_c) on the representative irreversible intra-grain current density ($J_{\text{irr}}^{\text{G}}$) and the representative reversible intra-grain current density ($J_{\text{rev}}^{\text{G}}$), as defined by equation (4.21). In A: $J_{\text{rev}}^{\text{G}} = 10^{10} \text{ A m}^{-2}$, and in B: $J_{\text{irr}}^{\text{G}} = 10^{10} \text{ A m}^{-2}$. The other parameters were $m = 1$, $d = 2 \text{ nm}$, $\lambda = 200 \text{ nm}$, and $s_0 = 1 \mu\text{m}$	47
4.8 Dependence of the inter-grain current density (J_c) on the magnetic penetration depth (λ) and the distribution function parameter (u). If a respective parameter was invariant, it had the value: $m = 1$, $J_{\text{irr}}^{\text{G}} = 1.5 \cdot 10^{10} \text{ A m}^{-2}$, $J_{\text{rev}}^{\text{G}} = 10^{10} \text{ A m}^{-2}$, $d = 2 \text{ nm}$, $\lambda = 200 \text{ nm}$, and $s_0 = 1 \mu\text{m}$	47
4.9 Impact of the characteristic thickness of the GBs (d) and the characteristic grain size (s_0) on the inter-grain current density (J_c). If a respective parameter was invariant, it had the value: $m = 1$, $J_{\text{irr}}^{\text{G}} = 1.5 \cdot 10^{10} \text{ A m}^{-2}$, $J_{\text{rev}}^{\text{G}} = 10^{10} \text{ A m}^{-2}$, $d = 2 \text{ nm}$, $\lambda = 200 \text{ nm}$ and	

	$s_0 = 0.5 \mu\text{m}$	48
4.10	Graphical illustration of the modified Global field profile that is generated by the inter-grain current density.s (inter-grain field profiles) for constant values of J_c on the increasing field branch ($J_{c,\text{inc}}$) and J_c on the decreasing field branch ($J_{c,\text{dec}}$) with $J_{c,\text{inc}} < J_{c,\text{dec}}$. The solid lines represent field profiles corresponding to additional applied fields and the dashed lines indicate the Field profile, that remains in the sample after cooling it at a certain field, then applying an additional field, and going back to the initial field. (residual field profile).	51
4.11	Magnetization curves of the inter-grain currents dependent on the background field (H_{bg}) and an iterative calculation of J_c and J^G for a field loop with a saturated field profile.	51
4.12	Residual magnetization originating from the inter-grain current ($M_{\text{res,inter}}$) in dependence of the background field (H_{bg}), where $a = b = 1 \text{ mm}$ with the inter-grain current density on the increasing field branch: $J_{c,\text{inc}} = 1.5 \cdot 10^8$, and on the decreasing field branch: $J_{c,\text{dec}} = 3.5 \cdot 10^8 \text{ A m}^{-2}$	52
4.13	Residual magnetization of the reversible ($M_{\text{res,rev}}^G$) and irreversible contribution of the grains ($M_{\text{res,irr}}^G$) in dependence on the ratio between J_c on the increasing field branch ($J_{c,\text{inc}}$) and J_c on the decreasing field branch ($J_{c,\text{dec}}$), where the background field (H_{bg}) is zero. The sample dimensions are $a = b = 1 \text{ mm}$ and the dimensions of the grains are $a^G = b^G = 1 \mu\text{m}$	53
4.14	Same as figure 4.12, but here the reversible ($M_{\text{res,rev}}^G$) and irreversible intra-grain contributions ($M_{\text{res,irr}}^G$) are shown for different background field (H_{bg}), where the J_c on the increasing field branch ($J_{c,\text{inc}}$) and the J_c on the decreasing field branch ($J_{c,\text{dec}}$) as well as the sample and grain dimensions were the same as in figure 4.13.	53
4.15	Residual magnetization (M_{res}) of the irreversible inter- ($M_{\text{res,inter}}$) and intra-grain contributions ($M_{\text{res,irr}}^G$) for different entry field into the grains (H_{entry}^G). The current densities were $J_{c,\text{inc}} = 10^8$, $J_{c,\text{dec}} = 3 \cdot 10^8$, and $J^G = 2 \cdot 10^{10} \text{ A m}^{-2}$, with the sample geometry: $a = b = 1 \text{ mm}$ and $c = 0.2 \text{ mm}$, and the geometry of the grains: $s_0 = 4 \mu\text{m}$	54
5.1	Sketch of the construction of a trapezoid and the corresponding field profile for a current flowing in positive x -direction, where the dashed-dotted lines indicates zero field. The figures C and D show how basic matrix operations can be applied to orientate the trapezoid. The other figures show examples of how the correct configuration of trapezoids can be used to calculate the field profile of more complex samples.	59
5.2	Model of the intra-grain current flow in a polycrystal and the comparison between the field profile originating from a current flowing only at the sample edges and the field profile corresponding to a polycrystal with 10^5 grains. The distance to the sample surface is equal to the edge length of the grains: $2s_0$	60
5.3	Examples of fits to the field profiles of the medium grained K doped sample on the decreasing (A) and the increasing field branch (B). The dotted vertical lines indicate the sample edges. The scans were performed across the sample center.	61
6.1	Hysteresis of the inter-grain current density (J_c) and the ratio between the increasing ($J_{c,\text{inc}}$) and decreasing field branch ($J_{c,\text{dec}}$). (Data provided by J. D. Weiss.)	64
6.2	Magnetization (M) of K and Co doped Ba-122 polycrystals with different grain sizes as a function of external applied field (H_{ext}). The background signal, measured 5 K above the superconducting transition temperature of the respective samples, was subtracted from the measurements. The insets show the dependence of the maximum inter-grain current density (J_c) on the characteristic grain size (s_0). The measurements were carried out at 5 K in a vibrating sample magnetometer.	65
6.3	Temperature dependence of the magnetization (M) of the K doped Ba-122 polycrystals with different characteristic grain size (s_0), from similar measurements as in figure 6.2.	67
6.4	Scanning Hall-probe microscope (SHPM) measurements of the small grained K doped sample and the corresponding magnetization (M) at 10 K, where the contribution of the inter-grain current density (contribution of J_c to the magnetization, which was evaluated from SHPM measurements ($M_{\text{inter}}^{\text{SHPM}}$)) is shown. The magnetization obtained from Hall-scans is compared to the magnetization measured by a superconducting quantum interference device (SQUID) magnetometer (M^{SQUID}). The sample was cooled in zero field, then the field was ramped to 3 T. During the subsequent run to -3 T the field profile of the sample	

	was measured at certain external applied field (H_{ext}), which are indicated by the labels in A. The spatial extent of the samples is given by the vertical dotted lines. The Hall-probe was at a constant z -position, and the distance to the sample surface was approximately 20 μm during the scans.	68
6.5	Scanning Hall-probe microscope (SHPM) measurements of the large grained K doped sample and the corresponding magnetization values (M) at 5 K, where the contribution of the inter-grain current density ($M_{\text{inter}}^{\text{SHPM}}$) and the contribution of the intra-grain current density (contribution of J^{G} to the magnetization, which was evaluated from SHPM measurements ($M_{\text{intra}}^{\text{SHPM}}$)) are shown together with their combined value (magnetization, which was evaluated from SHPM measurements (M^{SHPM})). The magnetization obtained from Hall-scans are compared to the magnetization measured by a SQUID magnetometer (M^{SQUID}). The sample was cooled in zero field, then the field was ramped to 3 T. During the subsequent run to -3 T the field profile of the sample was measured at certain external fields, which are indicated by the labels in A. The spatial extent of the samples is given by the vertical dotted lines. The Hall-probe was at a constant z -position, and the distance to the sample surface was approximately 20 μm at the left edge and 3 μm at the right edge because of a tilted sample surface.	69
6.6	Scanning Hall-probe microscope (SHPM) measurements of the medium grained sample, at 5 K, where the dashed curves are the fits to the data near the sample edge. The evaluated magnetization of the contribution of the inter-grain current density (J_c) to the magnetization, which was evaluated from SHPM measurements ($M_{\text{inter}}^{\text{SHPM}}$) and the contribution of the representative intra-grain current density (J^{G}) to the magnetization, which was evaluated from SHPM measurements ($M_{\text{intra}}^{\text{SHPM}}$) are plotted together with their combined value (M^{SHPM}). The dotted line is the magnetization measured by a SQUID magnetometer (M^{SQUID}). The errors correspond to one standard deviation of the fits.	71
6.7	Same data as in figure 6.6. The curve labeled magnetization corresponding to J_c that was evaluated with the model presented in this thesis ($M_{\text{inter}}^{\text{model}}$) denotes the fit with equation (4.21) to the values evaluated from scanning Hall-probe microscope (SHPM) measurements ($M_{\text{inter}}^{\text{SHPM}}$), where the evaluated representative intra-grain current density (J^{G}) from the SHPM measurements was used in equation (4.21).	71
6.8	Comparison between the developing and Part of the field profile, where the sign of the local field gradients at the sample edges was changed by a previous change of the external applied field. (reverse field profile) in magnetization (M) measurements on the medium grained sample. The dotted line represents the saturated magnetization (M_{sat}). The field values in the plots correspond to the external applied fields (H_{ext}) at which the measurements started.	72
6.9	Scanning Hall-probe microscope measurements from the medium grained sample at 5 K on the increasing and decreasing field branch, where the solid lines show the developing and the dashed lines the reverse field profiles. All measurement series start at 0.2 T.	73
6.10	Selected field profiles from figure 6.9A, where H_{meas} defines the external applied field in which the measurements were conducted.	73
6.11	Magnetization corresponding to the inter- ($M_{\text{inter}}^{\text{SHPM}}$) and intra-grain currents ($M_{\text{intra}}^{\text{SHPM}}$) calculated from the fits to the field profiles measured by the scanning Hall-probe microscope (SHPM) in figure 6.9, and the results for inter-grain current density (J_c) according to equation (4.21), where the evaluated intra-grain current density from the SHPM measurements and the parameters from the fit in figure 6.7 (here, J_c has a sign to allow a comparison with the data from the SHPM). The lines in A and B represent $M_{\text{inter}}^{\text{SHPM}} + M_{\text{intra}}^{\text{SHPM}}$. The errors correspond to one standard deviation of the fits.	75
6.12	Similar to figures 6.11B and 6.11D. The measurements started at 0.5 T.	76
6.13	Same measurements as in figure 6.8, where the vertical dotted lines indicate the first penetration field (H_1^*) of the inter-grain field profile. H_1^* in the individual measurements were estimated from scanning Hall-probe microscope measurements.	76
6.14	Magnetization measurements of a small ($3.47 \times 0.98 \times 0.50 \text{ m}^3$) and the large grained sample. The dotted line in the insets represent the J_c in A and representative intra-grain current density (J^{G}) in B. The „x“s in A are evaluations from the measurements in the main plot while the dots (\bullet) are evaluations from measurements that are not shown in the main plot. The circles (\circ) correspond to the same data multiplied by a certain factor.	77

6.15	Dependence of the inter- ($M_{\text{inter}}^{\text{peak}}$) and intra-grain magnetization peak ($M_{\text{intra}}^{\text{peak}}$) on the maximum applied field (H^{max}). The development of $M_{\text{inter}}^{\text{peak}}$ and the shift from the increasing to the decreasing field branch ($H_{\text{inter}}^{\text{peak}}$) with increasing H^{max} are displayed in B.	78
6.16	Residual magnetization (M_{res}) at various background fields (H_{bg}) as a function of the maximum additional applied field ($H_{\text{add}}^{\text{max}}$), as well as the logarithmic derivative of M_{res} , measured at 5 K. The respective H_{bg} of a measurement is given by the labels, the legends and the insets in A.	79
6.17	Evolution of the residual field profile of the medium grained sample at three different background fields (H_{bg}). The temperature was 5 K and the distance between the Hall-probe and the surface was 1 to 5 μm . The left figures show the field profiles at the maximum additional applied field ($H_{\text{add}}^{\text{max}}$) and the corresponding residual state (represented by dots and lines of the same color). In the right figures only the residual field profiles are plotted.	80
6.18	Data of the residual magnetization (M_{res}) from figure 6.16 and the inter- ($M_{\text{res,inter}}^{\text{SHPM}}$) and intra-grain contribution ($M_{\text{res,intra}}^{\text{SHPM}}$), which were evaluated from the scanning Hall-probe microscope (SHPM) measurements in figure 6.17 for selected background fields (H_{bg}). $M_{\text{res}}^{\text{SHPM}}$ represent their combined value. The curve labeled residual magnetization corresponding to J_c that was evaluated with the model presented in this thesis ($M_{\text{res,inter}}^{\text{model}}$) denotes the expected residual magnetization according to the presented model, where the evaluated representative intra-grain current density (J^{G}) from the SHPM measurements was used in equation (4.21) to calculate the inter-grain current density (J_c). The dashed curves show the expected residual magnetization originating from J_c ($M_{\text{res,inter}}$) according to the extended critical state model, where the field dependence of J_c was determined by fitting the evaluated current densities from developing magnetization curves.	82
6.19	Residual magnetization (M_{res}) of the small (geometry: $3.90 \times 0.68 \times 0.47 \text{ mm}^3$) and large grained sample as a function of the maximum additional applied field ($H_{\text{add}}^{\text{max}}$). The background fields in which the samples were cooled are written next to the curves and are indicated in the insets, where a magnetization loop from 7 to -7 T is displayed for the respective sample.	83
6.20	Magnetization loops (A) and measurements of the residual magnetization (M_{res}) at various background fields (H_{bg}) of a small grained K doped Ba-122 sample ($3.90 \times 0.68 \times 0.47 \text{ mm}^3$) before and after exposing it to different fast neutron fluences ($\Phi\Delta t$). The measurements were carried out at 5 K.	85

Explanation of Acronyms

Abbreviations

FL Flux line.

GB Grain boundary.

HTS High-temperature superconductor. In this thesis this term refers to cuprates and iron based superconductors.

JJ Josephson junction.

LTS Low-temperature superconductor. Superconductors that are described by standard theories (i.e. BCS theory).

SC Superconductor.

SHPM Scanning Hall-probe microscope.

SQUID Superconducting quantum interference device.

VSM Vibrating sample magnetometer.

Definitions

developing field profile Field profile, where a change of the external applied field leads to the development of local field gradients that replace the initial field profile.

decreasing field branch Field branch, in which the absolute value of the external applied field is decreasing.

extended critical state model Critical state model with a field dependent critical current density.

field profile Spatial variation of the magnetic field.

increasing field branch Field branch, in which the absolute value of the external applied field is increasing.

initial field profile Field profile after the sample was cooled below the transition temperature.

inter-grain field profile Global field profile that is generated by the inter-grain current density.

intra-grain field profile Global field profile that is generated by the grains of a polycrystal.

residual field profile Field profile, that remains in the sample after cooling it at a certain field, then applying an additional field, and going back to the initial field.

reverse field profile Part of the field profile, where the sign of the local field gradients at the sample edges was changed by a previous change of the external applied field.

saturated field profile Field profile of a sample, when the global current and the currents in the grains have the same orientation.

Nomenclature

d Characteristic thickness of the GBs. Parameter that defines half the thickness of a Josephson junction, i. e. a grain boundary.

H_{add} Additional applied field. Difference between the field in which a sample was cooled below the transition temperature and the external applied field.

$H_{\text{add}}^{\text{max}}$ Maximum additional applied field. Defines the difference between the field in which a sample was cooled below the transition temperature and the external applied field at which the field ramp changed.

H_{bg} Background field. Field in which a sample was cooled below the transition temperature.

H_{c1} Lower critical field. Defines the Meißner state in the reversible magnetization of a type-II superconductor.

H_{c2} Upper critical field. Defines the transition from the mixed state to the normal conducting state in a type-II superconductor.

H_{ext} External applied field. Field set by the operator.

$H_{\text{entry}}^{\text{G}}$ Entry field into the grains. Field that describes the delayed entry of flux lines into the grains, because of the finite dimensions of the grains.

H^{max} Maximum applied field. Define the external applied field at which the field ramp changed.

$H_{\text{inter}}^{\text{peak}}$ Field at which the maximum J_c is observed.

H_{return} Return field. Reversed field component at the grain boundaries. The direction of this field is reversed compared to the external applied field.

H^* Penetration field. Field at which a field gradient replaces the flat field distribution at the sample center (critical state model).

H_1^* First penetration field. Field at which a field gradient replaces the Field profile after the sample was cooled below the transition temperature. (initial field profile) (extended critical state model).

$H^{*\text{G}}$ Representative penetration field of the grains. Field at which the flat field distribution of all grains are replaced by a field gradient (critical state model).

$H_1^{*\text{G}}$ First representative penetration field of the grains. Field at which the flat field distribution of all grains are replaced by a field gradient (extended critical state model).

$H_2^{*\text{G}}$ Second representative penetration field of the grains. Field that has to be applied in order to completely replace a certain field distributions inside the grains (extended critical state model).

H_2^* Second penetration field. Field that has to be applied in order to completely replace a certain field distribution (extended critical state model).

- I_c Critical transport current.
- J_c Inter-grain current density. Current density that crosses the grain boundaries in a polycrystal. Also referred to as global or transport current density.
- $J_{c,dec}$ J_c on the decreasing field branch. This current density is introduced to distinguish between the increasing and decreasing field branch.
- $J_{c,inc}$ J_c on the increasing field branch. This current density is introduced to distinguish between the increasing and decreasing field branch.
- J_{c0} Maximum inter-grain current density. Maximum inter-grain current density found in a polycrystal.
- J^G Representative intra-grain current density. Current density that describes the global behavior of all grains best, and is thus a representative value for all individual grains.
- J_{irr}^G Representative irreversible intra-grain current density. Current density that describes the global behavior of all irreversible contributions of the grains best, and is thus a representative value for all individual grains.
- J_{rev}^G Representative reversible intra-grain current density. Current density that describes the global behavior of all reversible contributions of the grains best, and is thus a representative value for all individual grains.
- J_{intra} Intra-grain current density. Current density inside a grain, that does not cross the grain boundaries.
- J_J Josephson current density. Tunneling current density through a Josephson junction.
- $J_{J,max}$ Maximum Josephson current density. Maximum tunneling current density through a Josephson junction.
- λ Magnetic penetration depth.
- u Distribution function parameter. Parameter that defines the width of the distribution density function of the grain size in a polycrystal.
- M_{inter} Magnetization originating from J_c . Contribution to the magnetization of a polycrystal caused by the inter-grain current density.
- $M_{res,inter}$ Residual magnetization originating from J_c . Contribution of the inter-grain current density to the residual magnetization.
- M^G Magnetization from all grains. This value incorporates all reversible and irreversible contributions of the representative intra-grain current density.
- M_{irr}^G Magnetization originating from J_{irr}^G . Contribution of the representative irreversible intra-grain current density to the magnetization from all grains.
- M_{res}^G Residual magnetization of the grains. Contribution of the representative intra-grain current density to the residual magnetization.
- $M_{res,irr}^G$ Residual magnetization originating from all irreversible contributions of the grains. Contribution of the representative irreversible intra-grain current density to the residual magnetization.
- $M_{res,rev}^G$ Residual magnetization originating from all reversible contributions of the grains. Contribution of the representative reversible intra-grain current density to the residual magnetization.

- $M_{\text{rev}}^{\text{G}}$ Magnetization originating from $J_{\text{rev}}^{\text{G}}$. Contribution of the representative reversible intra-grain current density to the magnetization from all grains.
- $M_{\text{inter}}^{\text{model}}$ Magnetization corresponding to J_c that was evaluated with the model presented in this thesis.
- $M_{\text{res,inter}}^{\text{model}}$ Residual magnetization corresponding to J_c that was evaluated with the model presented in this thesis.
- $M_{\text{inter}}^{\text{peak}}$ Peak in the magnetization that corresponds to J_c .
- $M_{\text{intra}}^{\text{peak}}$ Peak in the magnetization that corresponds to J^{G} .
- M_{res} Residual magnetization. Denotes the history dependent magnetization at a specific field.
- M_{rev} Reversible magnetization. Denotes the magnetization of a superconductor without defects, i. e. very clean crystals.
- M_{sat} Saturated magnetization. Magnetization of (polycrystalline) superconductors, where the global field profile above the samples (and the local field profiles of the grains) are completely developed.
- M^{SHPM} Magnetization, which was evaluated from SHPM measurements.
- $M_{\text{inter}}^{\text{SHPM}}$ Contribution of J_c to the magnetization, which was evaluated from SHPM measurements.
- $M_{\text{res,inter}}^{\text{SHPM}}$ Contribution of J_c to M_{res} , which was evaluated from SHPM measurements.
- $M_{\text{intra}}^{\text{SHPM}}$ Contribution of J^{G} to the magnetization, which was evaluated from SHPM measurements.
- $M_{\text{res,intra}}^{\text{SHPM}}$ Contribution of J^{G} to M_{res} , which was evaluated from SHPM measurements.
- M^{SQUID} Magnetization measured by a SQUID magnetometer.
- s Length of a JJ. Parameter that defines half the length of a Josephson junction, i. e. a grain boundary.
- s_0 Characteristic grain size. Defines the maximum in the distribution density function of the grain size (i. e. the mode). The parameter can describe either half the length of a Josephson junction or half the grain diameter.
- T_c Superconducting transition temperature.

Chapter 1

Introduction

Get your facts first, then you can distort them as you please.

— Mark Twain

The main application of superconductors (SCs) is to provide high magnetic fields, which are necessary in many scientific and medical equipments. The improvement and exploration of magnetic field technologies is often accompanied by the need for more powerful magnets. For instance, the resolution of magnetic resonance tomography images is better the higher, and more homogeneous, the magnetic field of the magnet coils is [Wen97]. In future fusion reactors high magnetic fields are essential to operate, sustain, and confine the created plasma, in which the hydrogen isotopes deuterium and tritium are reacted to form helium. This reaction releases energy which can be used for the production of electricity. The hydrogen isotopes are abundantly available and the fusion products are not contributory to the greenhouse effect, wherefore great hopes are pinned on such power plants to provide a sustainable and nonpolluting energy source. Another famous application are particle accelerators. They that depends on high field magnets to focus and guide the charged particle beams [Bot12]. Copper magnet coils, which are capable of generating the required fields for these applications, would consume an unreasonable amount of material and energy, as well as a large space to accommodate the coils.

SCs have found their place in these elaborated scientific applications. Their ability to carry large currents in a comparatively small cross section gives them a big advantage over copper wires. The main drawback of the commercially available low-temperature superconductors (LTSs), such as Nb-Ti and Nb₃Sn, is their requirement to operate in liquid helium, because of a superconducting transition temperature (T_c) in the range of 9 to 23 K. The highest magnetic fields reached with these magnets at liquid helium temperature (4.2 K) is about 20 T.

So-called high-temperature superconductors (HTSs)* are not able to replace the established LTSs, yet, although T_c can reach more than 130 K. One problem of HTSs is the feasibility of round, polycrystalline, multi-filament wires, which are the preferred choice to build high field magnets [Lar01]. The main problems to overcome are the optimization of the growth process and the properties of the grain boundaries (GBs). Great efforts are made to reduce the misalignment between the crystallographic axes of the grains in order to prevent the limiting character of large angle GBs and thereby increase the maximum critical transport current (I_c). This has been successfully done for HTS tapes [Shi13], but their geometry is less preferable to the round cross section of wires and their fabrication process is complicated and expensive.

In 2008, superconductivity was found in iron based compounds [Kam08]. This new class of superconducting materials is usually referred to as iron based SCs. They excited much interest, because of their relative high T_c of up to 55 K, a small anisotropy of superconducting parameters between the crystallographic *ab*-plane and the *c*-axis of about 1 to 10, a high upper critical field

* In this thesis this term referres to cuprates and iron based SCs.

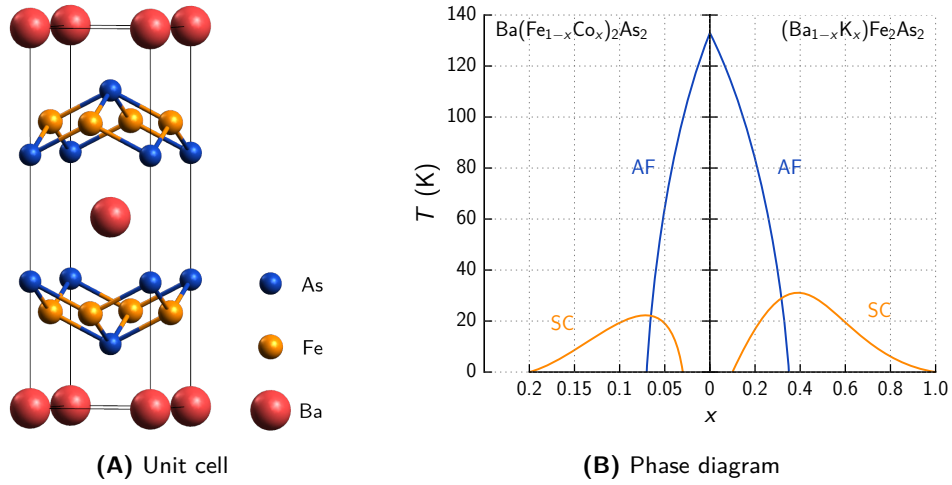


Figure 1.1: Crystallographic structure of BaFe_2As_2 and the (simplified) phase diagram with the superconducting dome (SC) and the antiferromagnetic regime (AF) for Co and K doping.

(H_{c2}) of about 100 T and more favorable GB properties, which do not limit I_c as strongly as in other HTSs [Asw10; Kat11]. Beside recent encouraging results with Bi-2212 [Lar97], the iron based SCs are promising for the production of cheap untextured wires because they exhibit a much better performance than other untextured HTS wires. The first iron based SC wires with reasonable transport current densities could be realized relatively soon after their discovery [Wei12]. However, major improvements are still necessary for these materials to become competitive to the currently established Nb-Ti and Nb_3Sn wires. The reason why further investigations of iron based SCs are important, is the low costs of the materials and the comparatively easy synthesis, which gives the iron based SCs a big economical advantage.

1.1 Iron Based Superconductors

Until 2008, all known unconventional HTSs had one or more copper-oxide planes in their structural unit cells, from which the superconductivity of the materials originates. In 2006 [Kam06], a T_c of about 4 K was reported for LaOFeP and in 2008 the same group found superconductivity at 26 K in a related compound [Kam08]. Shortly after this discovery many other families with a maximum T_c of about 55 K [Zhi08] could be identified.

Figure 1.1A displays the crystallographic structure of the BaFe_2As_2 compound. In this thesis, optimally K [Rot08] and Co doped [Sef08] bulk samples of this material are investigated. The T_c of this so-called Ba-122 phase is about 36 K for the K doped compound and approximately 24 K for the Co doped system. The figure shows a structure common to iron based SCs. The Fe and As atoms form layers which are separated by a non-iron layer. The Fe-As layer is a square lattice of iron atoms and an interlacing lattice of As atoms. The difference between the various iron based SCs is the number and the chemical element of the blocking layers (one Ba-plane in Ba-122), and the orientation of the adjacent Fe-As layers with respect to each other (opposite orientation in Ba-122).

Like the cuprates, the parent compounds of iron based SCs are not superconducting. To enable superconductivity in these materials the components are substituted, i.e. doped, with other chemical elements. The qualitative understanding of the superconducting state in these materials is still progressing, but no commonly accepted theory exists so far [Kei15]. Mainly three strategies can be applied to induce superconductivity in HTSs:

- One is the *aliovalent substitution*, where the substituted ion has a different oxidation state as the ion it is replacing (e. g. $(\text{Ba}_{1-x}\text{K}_x)\text{Fe}_2\text{As}_2$ for hole doping and $\text{Ba}(\text{Fe}_{1-x}\text{Co}_x)_2\text{As}_2$ for electron doping).
- Another is the modification of the crystallographic structure with an element of the same oxidation state as the ion it is replacing (e. g. $\text{BaFe}_2(\text{As}_{1-x}\text{P}_x)_2$), referred to as *isovalent substitution*.
- The application of *pressure* can also induce superconductivity [Eng13].

The phase diagram resulting from these methods resemble each other. In figure 1.1B the superconducting dome is visualized for K and Co doped Ba-122, where the variable x defines the fraction of the substituted element. The superconducting dome has a maximum T_c at $x = 0.4$ in case of the K doped crystals [Avc12; Cha13] and at $x = 0.06$ in case of the Co doped crystals [Chu09; Cha13]. The substitution level at which T_c has a maximum is denoted as optimally doped.

Besides their similarities, such as the phase diagram, the layered crystal structure of the superconducting planes, and the antiferromagnetism, the iron based SCs and the cuprates exhibit important differences. One is that the undoped iron based systems are (semi)metals [Ma08; Cha13] while the cuprates are insulators [Kei15]. Furthermore, the Cu and O atoms of the cuprates form a two dimensional layer, while the Fe-As layers are more three dimensional. Thus, the superconducting properties of the cuprates mirror the two dimensional character of the layers, i. e. the superconductivity is good within the Cu-layers but it is reduced between them. This large anisotropy complicates the fabrication of wires and tapes for applications. The iron based SCs have more isotropic properties compared to the cuprates [Put10].

1.2 Grain Boundaries

When superconductivity was found in the ceramic HTSs the current limiting properties of the GBs in these materials made them questionable for large scale application. In the following years the understanding of the GB properties was, and still is, one of the major research fields of HTSs.

GBs are a consequence of the growth of many nuclei during the solidification process of a sample. They form a three dimensional network which affects the current transport through the bulk material in the superconducting state [Dur11].

The effects GBs have in HTSs differ substantially from the ones encountered in LTSs. The difficulty of realizing high magnetic field technologies based on HTSs is rooted in the physics of the GBs [Hil02]. The fundamental parameter(s), which define the properties of a GB, are not utterly clear. Some parameters which may influence the properties of the current transport are the length scale of the structural disorder, non-stoichiometry, lattice strains, the screening length, and the superconducting coherence length which quantifies the spatial extent of the Cooper pairs [Gra10; Hil02].

A possible explanation may be found by considering the comparable short coherence length of those materials, however, as pointed out by Durrell et al. [Dur11], Nb_3Sn has a comparable coherence length in the zero temperature limit compared to HTSs, yet its GBs act as efficient pinning centers. A key issues of the GB physics may be the proximity of the superconducting state to the antiferromagnetic state in cuprates and iron based SCs and their low carrier density, which determines how well local electrostatic charges of the non-superconducting GB regions can be screened [Dur11].

GBs can be classified geometrically by choosing one representative crystallographic plane and the angle of the misalignment between these plains in two neighboring grains. Some examples are given in figure 1.2, where the direction of the unit cell vectors of the crystals are described by $[abc]$, where the dashed lines indicate the ab -plains while the grids indicate their orientation. In case of the $[001]$ tilt the c -axis of the crystal is the rotation axis and the angle between the differently oriented ab -planes defines the misalignment (figure 1.2A). These kind of GBs are very rarely found

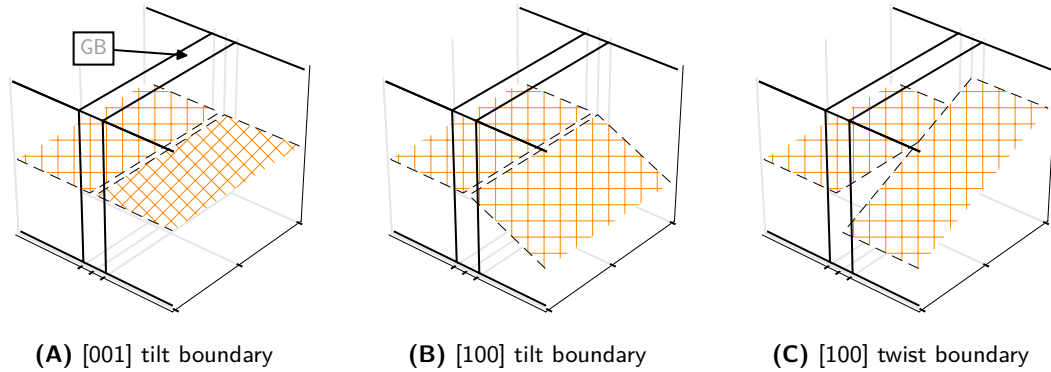


Figure 1.2: Examples for the grain boundary (GB) misalignment commonly encountered in polycrystalline bulks and thin films.

in bulks, but they are favored by epitaxial growth on the substrates of superconducting tapes [Dur11]. Although polycrystals are the primary choice for technical applications, the analysis of the behavior of the GBs is very hard to realize for them. Thus, well-defined bicrystals are grown as thin-films and investigated to deduce the GB properties.

The measurements on bicrystals reveal important properties of the GBs in HTSs. They limit the inter-grain current density (J_c) and form so-called Josephson junctions (JJs), i. e. weak-links, if the displacement angle is large [Hil02; Kat11]. The weakly link nature of HTSs is an intrinsic physical property of the GBs themselves and is not a result of material defect structures, such as voids or impurity layers that accumulate at the GBs. This does not mean that material defects are unimportant for the current transport mechanism, but rather, that the physics is characteristic of clean and structurally well-defined boundaries.

Further characteristics are found for the behavior of a GB in magnetic fields. Below a certain grain misalignment-angle the J_c across the GB is less sensitive to magnetic field changes. Above this angle, J_c decreases rapidly with increasing field and larger misalignment-angles [Hil02].

Different approaches can be applied to overcome the limiting mechanisms of the GBs. One way to increase the current transport in technological SCs is either to avoid GBs as a whole, i. e. single crystalline SCs, or to optimize the growth of the grains. Since the fabrication of kilometer long single-crystals, preferably grown as a magnet coil, is unrealistic, long wires or tapes can only be achieved with polycrystalline SCs.

The so-called coated conductors overcome the obstacles of GBs by utilizing the fact that J_c across low-angle GBs ($\lesssim 7.5^\circ$) is sufficiently large. The technical term used for this artificially induced alignment of the grains is texturing. Ion beam assisted deposition (IBAD) and rolling assisted biaxial textured substrate (RABiTS) techniques are examples for successful implementations of HTSs texturing. Although there are commercially available superconducting tapes, their production is not trivial and comparatively expensive. A better understanding of the GB mechanisms may provide an alternative to the coated conductors. [Lar01]

1.3 Granularity and Current Transport

The physics of the GB is closely related to the current transport of a sample. The transport current can flow in the whole sample when the GBs are not obstructive in a material, while it is restricted to the individual grains when the GBs block the global current, which leads to many small current loops in the sample [Dur11]. The weakly linked GBs in the HTSs drastically influence the current transport so that it cannot be defined as a single valued quantity [Eve88]. In contrast to LTSs, the current transport has to be separated into two length scales [Gur11].

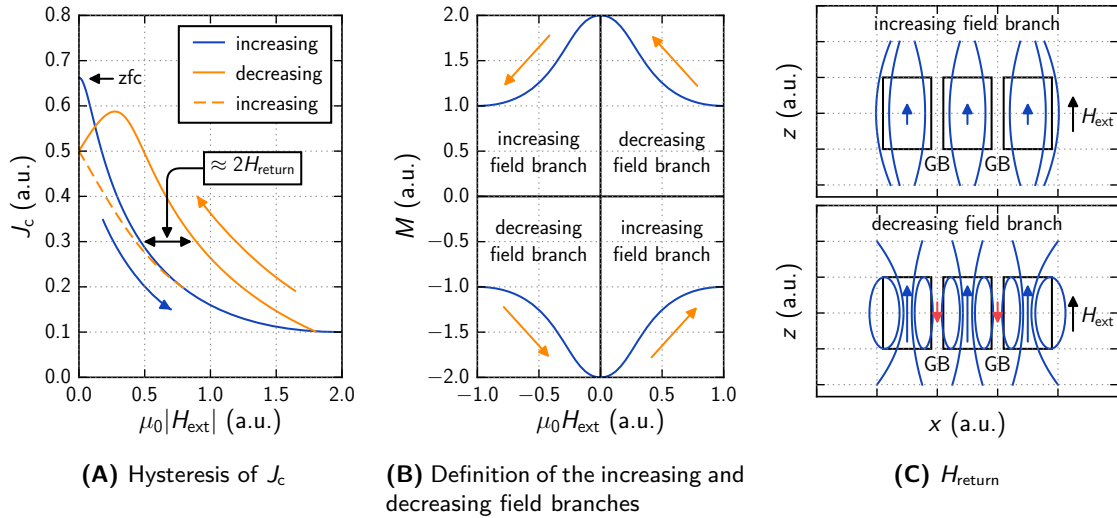


Figure 1.3: Sketch of the hysteresis of the inter-grain current density (J_c), the definition of the increasing and decreasing field branches in the respective quadrants of a magnetization measurement, and the commonly accepted explanation for the hysteresis of J_c based on the return field (H_{return}).

The larger scale is defined by the sample volume, similar to LTSs, and is referred to as global, transport, or inter-grain current density (J_c). In contrast to the LTSs a second, smaller, length scale is present, which describes the current flow within the individual grains which is referred to as the intra-grain current density (J_{intra}). These two currents occur at the same time and contribute to the total magnetic signal of the polycrystal. The quantitative separation of these current densities is the main focus of this thesis.

A feature of the weakly linked character of the GBs is a hysteresis of J_c , which is sketched in figure 1.3A. The values of J_c are found to be smaller when the absolute value of the external applied field (H_{ext}) is increased (referred to as the increasing field branch) compared to the case when $|H_{\text{ext}}|$ is decreased (decreasing field branch; cf. figure 1.3B). This hysteresis effect has been reported for $\text{YBa}_2\text{Cu}_3\text{O}_x$ [Dau92; Eve88; Kun98], $(\text{Tl}_{0.5}\text{Pb}_{0.5})(\text{Sr}_{0.8}\text{Ba}_{0.2})_2\text{Ca}_2\text{Cu}_3\text{O}_x$ and $\text{Bi}_2\text{Sr}_2\text{CaCu}_2\text{O}_x$ [Lis97], $(\text{Bi}_{0.85}\text{Pb}_{0.15})_2\text{Sr}_2\text{Ca}_2\text{Cu}_3\text{O}_x$ [Mar94], and, as an example for the iron based SCs, $\text{SmFeAs}(\text{O}_{0.8}\text{F}_{0.2})$ [Ni10], as well as the BaFe_2As_2 samples that were investigated for this thesis.

The commonly accepted explanation for this effect is based on the field arising from J_{intra} , which leads to a reversed field component at the GBs [Eve88; Pal04; Pal07], referred to as the return field (H_{return}). As proposed by Evetts and Glowacki [Eve88] the complex dependence of J_c on H_{ext} and the grain structure is describable in terms of the hysteric properties of a JJ network that is mediated by the magnetic flux trapped by the grains. This effect is illustrated in figure 1.3C, where the grains are approximated by the rectangles. On the increasing field branch, pinning hinders the penetration of the magnetic flux into the grains and more flux is concentrated at the GBs compared to grain centers. This relation is reversed on the decreasing field branch.

An intuitive way to picture H_{return} is to look at the field lines. On the decreasing field branch, the sample has a surplus of field lines inside the grains, which have to close somewhere because of the Maxwell equation: $\nabla \cdot \mathbf{H} = 0$. Since the GBs are regions of weak superconductivity some fraction of the excess field lines may close at the GBs. These field lines correspond to a field that is directed in the opposite direction of H_{ext} . This H_{return} changes the value of the local magnetic induction at the GBs relative to H_{ext} :

$$B = \mu_0(H_{\text{ext}} - H_{\text{return}}). \quad (1.1)$$

Thus, the local field at the GBs is slightly ahead of H_{ext} , which leads to a shift of the magnetic response as illustrated in figure 1.3A.

The magnitude of the J_c hysteresis is determined by the difference between the external magnetic flux and the trapped flux inside the grains. How much flux is trapped by a grain depends on the effectiveness of the pinning centers, i. e. J_{intra} , and the size of the grains, i. e. large grains can trap more flux leading to larger hysteresis effects. H_{return} can be estimated from the field necessary to compensate the shift of the magnetic response of a sample [Pal07]. However, J_{intra} would have to be about 10^{12} A m^{-2} in order to explain the observed shift in a K doped Ba-122 bulk with a characteristic grain size of approximately $0.1 \text{ }\mu\text{m}$ (radius), which is far larger than the maximum current density found in K doped Ba-122 single-crystals [Kih13].

1.4 Motivation and Outline of Thesis

Although H_{return} contributes to the hysteresis of J_c to some extent, another effect had to be responsible to explain the observed behavior, which initiated the search of a complementary mechanism.

To provide information on the properties of the GBs in a material the contributions of J_c and J_{intra} have to be identified by a suitable measurement technique. This is impossible with standard transport current measurements, where only J_c is accessible. Müller et al. [Mul94] proposed that the measurement of the remanent magnetization* could be used to detect both contributions. Such measurements were conducted, but they gave rise to more questions and indicated a complicated interaction between the global and local currents.

A possible experimental way to identify the currents is to measure the remanent magnetization of a polycrystalline sample and then grinding it to get disconnect grains. The obvious drawback is the destruction of the sample and the uncertainty if the resulting powder is crystalline. More likely, the powder will consist of grain clusters with a certain number of connected grains of varying size so that some contributions of J_c are still present. Moreover, the strong mechanical stress may change the properties of the current transport in the grains by introducing defects. This are the reasons why such an approach was avoided.

Magnetization measurements probe the global magnetic response of a sample. They provide very limited insights on the spatial distribution, as well as the contributions of J_c and J_{intra} , and their interactions. A scanning Hall-probe microscope (SHPM) allows to draw conclusions on the current flow in a SC by mapping the local magnetic induction of a sample. These so-called field maps, or field profiles, reveal important insights on the magnetic structures in a sample such as current percolation or clusters of well connected grains. In order to identify these properties an SHPM with a high spatial resolution and a large measurement area was built to enable the analysis of polycrystalline samples. The basic setup of the SHPM as well as the measurement techniques mentioned above are presented in chapter 2.

Models are necessary to analyze the magnetization and the SHPM measurements quantitatively. The inter-grain contributions modify the intra-grain signal, and vice versa, which makes a self consistent modeling very difficult. Chapter 3 discusses the influence of J_c on the intra-grain contribution. Thereby, the properties of the grains are described with the help of models utilized to describe crystals, which are briefly introduced. These models are then extended to show how the presence of J_c modifies the global magnetic response of all intra-grain contributions.

Chapter 4 reviews the description of the GB with the help of the Josephson effect and introduces the model of Svistunov and D'yachenko [Svi92] who proposed a history dependent J_{intra} to describe the anomalous hysteresis effects found in HTS polycrystals. Their idea is combined with the calculations of Gonzalez et al. [Gon01] by carrying out an integration over a distribution density describing the varying grain size in a polycrystal. This combination of models allows

* Usually, the remanent magnetization denotes the magnetization that remains in a material after removal of H_{ext} , i. e. zero field. In this thesis the term: residual magnetization (M_{res}), is introduced, which denotes the history dependent magnetization at a certain field.

predictions on the global current transport of a SC, which is interesting in view of technical applications. Therefore, the relevance of the individual parameters is discussed in detail.

The discussion of the interactions between J_c and J_{intra} is motivated by the aforementioned magnetization and the SHPM measurements, which are introduced in chapter 2 together with the measured iron based polycrystals. To evaluate the data of the SHPM, a model for the separation of J_c and J_{intra} is devised in chapter 5 and the penultimate chapter is dedicated to the presentation of the data of the various measurement techniques and their evaluation.

Some passages have been quoted verbatim from J. Hecher et al. (2016): „Small grains: a key to high-field applications of granular Ba-122 superconductors?“ *Supercond. Sci. Technol.* **29**, 025004 (open access).

References

- [Asw10] P. M. Aswathy, J. B. Anooja, P. M. Sarun, and U. Syamaprasad (2010): „An overview on iron based superconductors“ *Supercond. Sci. Technol.* **23**, 073001.
- [Avc12] S. Avci, O. Chmaissem, D. Y. Chung, S. Rosenkranz, E. A. Goremychkin, J. P. Castellan, I. S. Todorov, J. A. Schlueter, H. Claus, A. Daoud-Aladine, D. D. Khalyavin, M. G. Kanatzidis, and R. Osborn (2012): „Phase diagram of $\text{Ba}_{1-x}\text{K}_x\text{Fe}_2\text{As}_2$ “ *Phys. Rev. B* **85**, 184507.
- [Bot12] L. Bottura, G. de Rijk, L. Rossi, and E. Todesco (2012): „Advanced Accelerator Magnets for Upgrading the LHC“ *IEEE Trans. Appl. Supercond.* **22**, 4002008.
- [Cha13] A. Charnukha (2013): *Charge Dynamics in 122 Iron-Based Superconductors*. ISBN: 9783319011929.
- [Chu09] J.-H. Chu, J. G. Analytis, C. Kucharczyk, and I. R. Fisher (2009): „Determination of the phase diagram of the electron-doped superconductor $\text{Ba}(\text{Fe}_{1-x}\text{Co}_x)_2\text{As}_2$ “ *Phys. Rev. B* **79**, 014506.
- [Dau92] M. Däumling, E. Sarnelli, P. Chaudhari, A. Gupta, and J. Lacey (1992): „Critical current of a high- T_c Josephson grain boundary junction in high magnetic field“ *Appl. Phys. Lett.* **61**, 1355.
- [Dur11] J. H. Durrell, C.-B. Eom, A. Gurevich, E. E. Hellstrom, C. Tarantini, A. Yamamoto, and D. C. Larbalestier (2011): „The behavior of grain boundaries in the Fe-based superconductors“ *Rev. Mod. Phys.* **74**, 124511.
- [Eng13] J. Engelmann, V. Grinenko, P. Chekhonin, W. Skrotzki, D. V. Efremov, S. Oswald, K. Iida, R. Hühne, J. Hänisch, M. Hoffmann, F. Kurth, L. Schultz, and B. Holzapfel (2013): „Strain induced superconductivity in the parent compound BaFe_2As_2 “ *Nat. Commun.* **4**, 2877.
- [Eve88] J. E. Evetts and B. A. Glowacki (1988): „Relation of critical current irreversibility to trapped flux and microstructure in polycrystalline $\text{YBa}_2\text{Cu}_3\text{O}_7$ “ *Cryogenics* **28**, 641.
- [Gon01] J. L. Gonzalez, E. V. L. Mello, M. T. D. Orlando, E. S. Yugue, and E. Baggio-Saitovitch (2001): „Transport critical current in granular samples under high magnetic fields“ *Physica C* **364–365**, 347.
- [Gra10] S. Graser, P. J. Hirschfeld, T. Kopp, R. Gutser, B. M. Andersen, and J. Mannhart (2010): „How grain boundaries limit supercurrents in high-temperature superconductors“ *Nat. Phys.* **6**, 609.
- [Gur11] A. Gurevich (2011): „To use or not to use cool superconductors?“ *Nat. Mater.* **10**, 255.

- [Hec16] J. Hecher, T. Baumgartner, J. D. Weiss, C. Tarantini, A. Yamamoto, J. Jiang, E. E. Hellstrom, D. C. Larbalestier, and M. Eisterer (2016): „Small grains: a key to high-field applications of granular Ba-122 superconductors?“ *Supercond. Sci. Technol.* **29**, 025004.
- [Hil02] H. Hilgenkamp and J. Mannhart (2002): „Grain boundaries in high- T_c superconductors“ *Rev. Mod. Phys.* **74**, 485.
- [Kam06] Y. Kamihara, H. Hiramatsu, M. Hirano, R. Kawamura, H. Yanagi, T. Kamiya, and H. Hosono (2006): „Iron-Based Layered Superconductor: LaOFeP“ *J. Am. Chem. Soc.* **128**, 10012.
- [Kam08] Y. Kamihara, T. Watanabe, M. Hirano, and H. Hosono (2008): „Iron-Based Layered Superconductor La(O_{1-x}F_x)FeAs ($x = 0.05$ – 0.12) with $T_c = 26$ K“ *J. Am. Chem. Soc.* **130**, 3296.
- [Kat11] T. Katase, Y. Ishimaru, A. Tsukamoto, H. Hiramatsu, T. Kamiya, K. Tanabe, and H. Hosono (2011): „Advantageous grain boundaries in iron pnictide superconductors“ *Nat. Commun.* **2**, 409.
- [Kei15] B. Keimer, S. A. Kivelson, M. R. Norman, S. Uchida, and J. Zaanen (2015): „From quantum matter to high-temperature superconductivity in copper oxides“ *Nature* **518**, 179.
- [Kih13] K. J. Kihlstrom, L. Fang, Y. Jia, B. Shen, A. E. Koshelev, U. Welp, G. W. Crabtree, W.-K. Kwok, A. Kayani, S. F. Zhu, and H.-H. Wen (2013): „High-field critical current enhancement by irradiation induced correlated and random defects in (Ba_{0.6}K_{0.4})Fe₂As₂“ *Appl. Phys. Lett.* **103**, 202601.
- [Kun98] M. N. Kunchur and T. R. Askew (1998): „Hysteretic internal fields and critical currents in polycrystalline superconductors“ *J. Appl. Phys.* **84**, 6763.
- [Lar01] D. C. Larbalestier, A. Gurevich, M. D. Feldmann, and A. Polyanskii (2001): „High- T_c superconducting materials for electric power applications“ *Nature* **414**, 368.
- [Lar97] D. C. Larbalestier, J. Jiang, U. P. Trociewitz, F. Kametani, C. Scheuerlein, M. Dalban-Canassy, M. Matras, P. Chen, N. C. Craig, P. J. Lee, and E. E. Hellstrom (1997): „Isotropic round-wire multifilament cuprate superconductor for generation of magnetic fields above 30 T“ *Nat. Mater.* **13**, 375.
- [Lis97] F. A. List, D. M. Kroeger, and V. Selvamanickam (1997): „Hysteresis of the transport critical current of (Tl,Pb)-(Sr,Ba)-Ca-Cu-O and Bi-Sr-Ca-Cu-O conductors: effects of temperature and magnetic field“ *Physica C* **275**, 220.
- [Ma08] F. Ma and Z.-Y. Lu (2008): „Iron-based layered compound LaFeAsO is an antiferromagnetic semimetal“ *Phys. Rev. B* **78**, 033111.
- [Mar94] I. Martini, J. Bechtold, M. Majoros, V. Ottoboni, J.-C. Vallier, and S. Zannella (1994): „Superconducting properties of multilayered Bi(Pb)-2223/Ag tapes“ *Supercond. Sci. Technol.* **7**, 24.
- [Mul94] K.-H. Müller, C. Andrikidis, H. K. Liu, and S. X. Dou (1994): „Intergranular and intragranular critical currents in silver-sheathed Pb-Bi-Sr-Ca-Cu-O tapes“ *Phys. Rev. B* **50**, 10218.
- [Ni10] B. Ni, J. Ge, M. Kiuchi, E. S. Otabe, Z. Gao, L. Wang, Y. Qi, X. Zhang, and Y. Ma (2010): „Critical current characteristics and history dependence in superconducting SmFeAsOF bulk“ *JPCS* **234**, 012028.
- [Pal07] A. Palau, T. Puig, X. Obradors, and Ch. Jooss (2007): „Simultaneous determination of grain and grain-boundary critical currents in YBa₂Cu₃O₇-coated conductors by magnetic measurements“ *Phys. Rev. B* **75**, 054517.

- [Pal04] A. Palau, T. Puig, X. Obradors, E. Pardo, C. Navau, A. Sanchez, A. Usoskin, H. C. Freyhardt, L. Fernandez, B. Holzapfel, and R. Feenstra (2004): „Simultaneous inductive determination of grain and intergrain critical current densities of $\text{YBa}_2\text{Cu}_3\text{O}_{7-x}$ coated conductors“ *Appl. Phys. Lett.* **84**, 230.
- [Put10] M. Putti, I. Pallecchi, E. Bellingeri, M. R. Cimberle, M. Tropeano, C. Ferdeghini, A. Palenzona, C. Tarantini, A. Yamamoto, J. Jiang, J. Jaroszynski, F. Kametani, D. Abaimov, A. Polyanskii, J. D. Weiss, E. E. Hellstrom, A. Gurevich, D. C. Larbalestier, R. Jin, B. C. Sales, A. S. Sefat, M. A. McGuire, D. Mandrus, P. Cheng, Y. Jia, H. H. Wen, S. Lee, and C. B. Eom (2010): „New Fe-based superconductors: properties relevant for applications“ *Supercond. Sci. Technol.* **23**, 034003.
- [Rot08] M. Rotter, M. Tegel, and D. Johrendt (2008): „Superconductivity at 38 K in the Iron Arsenide $(\text{Ba}_{1-x}\text{K}_x)\text{Fe}_2\text{As}_2$ “ *Phys. Rev. Lett.* **101**, 107006.
- [Sef08] A. S. Sefat, R. Jin, M. A. McGuire, B. C. Sales, D. J. Singh, and D. Mandrus (2008): „Superconductivity at 22 K in Co-Doped BaFe_2As_2 Crystals“ *Phys. Rev. Lett.* **101**, 117004.
- [Shi13] Y. Shiohara, M. Yoshizumi, Y. Takagi, and Izumi T. (2013): „Future prospects of high- T_c superconductors-coated conductors and their applications“ *Physica C* **484**, 1.
- [Svi92] V. M. Svistunov and A. I. D'yachenko (1992): „A layered structure as a Josephson medium“ *Supercond. Sci. Technol.* **5**, 98.
- [Wei12] J. D. Weiss, C. Tarantini, J. Jiang, F. Kametani, A. A. Polyanskii, D. C. Larbalestier, and E. E. Hellstrom (2012): „High intergrain critical current density in fine-grain $(\text{Ba}_{0.6}\text{K}_{0.4})\text{Fe}_2\text{As}_2$ wires and bulks“ *Nat. Mater.* **11**, 682.
- [Wen97] H. Wen, T. J. Denison, R. W. Singerman, and R. S. Balaban (1997): „The Intrinsic Signal-to-Noise Ratio in Human Cardiac Imaging at 1.5, 3, and 4 T“ *J. Magn. Reson.* **125**, 65.
- [Zhi08] R. Zhi-An, L. Wei, Y. Jie, Y. Wei, S. Xiao-Li, L. Zheng-Cai, C. Guang-Can, D. Xiao-Li, S. Li-Ling, Z. Fang, and Z. Zhong-Xian (2008): „Superconductivity at 55 K in Iron-Based F-Doped Layered Quaternary Compound $\text{Sm}(\text{O}_{1-x}\text{F}_x)\text{FeAs}$ “ *Chin. Phys. Lett.* **25**, 2215.

Chapter 2

Samples and Experiments

Either write something worth reading or do something worth writing.

— Benjamin Franklin

The iron based superconductors (SCs) are a comparatively new family of high-temperature superconductors (HTSs). The discovery that superconductivity is possible in iron based materials was unexpected, because the strong ferromagnetism of elemental iron was believed to suppress superconductivity. Even more surprising was the relatively high superconducting transition temperature (T_c) of these materials. This has opened a new avenue of research, driven by the fact that the fundamental understanding of the origins of superconductivity needs significant improvement. [Pag10]

The search for the nature of superconductivity in iron based SCs, and HTSs in general, is a very exciting field of research, but is not the focus of this work. Here, the description of the current transport mechanisms in polycrystalline samples and their implications in view of applications is the main point of interest.

2.1 Samples

The investigated samples in this thesis are optimally K and Co doped BaFe_2As_2 (Ba-122) bulks, where the grain sizes were varied systematically. The synthesis of Fe-As superconductors is not an easy undertaking. Not only is As poisonous, it also has a high vapor pressure, which may lead to an explosion during the production process [Wei13]. To reduce the chance of an explosion the heating of the starting mixture is usually slow. The parent materials can be elemental or binary compounds, the latter preventing the vaporization of As.

The K doped samples were synthesized by a mechanochemical reaction introduced by Weiss et al. [Wei13]. The separate elements are ground to make Ba-122 powder for the synthesis. By controlling the grinding process the volatile elements As and K can be retained during the reaction to Ba-122. The resulting particles are of sub-micrometer size, which is advantageous because they help to produce more homogeneous, phase-pure, bulks of $(\text{Ba}_{1-x}\text{K}_x)\text{Fe}_2\text{As}_2$, where x is 0.4 in the investigated samples.

The Co doped Ba-122 polycrystalline bulk samples were synthesized using different starting powders [Hay14]. Ba, FeAs and CoAs powders were weighed in stoichiometric ratio to form $\text{Ba}(\text{Fe}_{1-x}\text{Co}_x)_2\text{As}_2$, with $x = 0.08$, for the largest grain size. Then the powder was pressed into a pellet, and heated. In case of the medium grain size, the separate elements were mixed and ground similar to the K doped samples. Elemental metals were also used for the fine grained sample.

Dopant	T_c (K)	Grain size	Geometry (mm ³)	n	Alias
K	35.7	$\approx 0.1 \mu\text{m}$	$1.96 \times 1.78 \times 0.35$	0.76	small
K	35.7	$\approx 0.1 \mu\text{m}$	$3.90 \times 0.68 \times 0.47$	0.62	small*
K	35.7	$\approx 0.1 \mu\text{m}$	$3.47 \times 0.98 \times 0.50$	0.66	small*
K	35.9	$1.0 \mu\text{m}$	$2.04 \times 2.03 \times 0.56$	0.69	medium
K	37.5	$3.1 \mu\text{m}$	$2.01 \times 1.96 \times 0.54$	0.69	large
Co	22.6	$\lesssim 1 \mu\text{m}$	$1.7 \times 1.2 \times 1.10$	0.48	small
Co	24.7	$\approx 1 \mu\text{m}$	$1.6 \times 1.2 \times 0.79$	0.55	medium
Co	26.1	$\approx 5 \mu\text{m}$	$1.8 \times 1.3 \times 0.40$	0.67	large

Table 2.1: Characteristics of the examined Ba-122 polycrystals. The grain size refers to the radius of the grains and n is the demagnetization factor for the respective sample geometries.

The grain size of the bulks is controlled by the temperature and the duration of the heat treatment of the ground powder, where higher temperatures and longer heat treatments result in larger grains. Samples synthesized at higher temperatures have a higher density and phase purity, but they were found to carry smaller transport currents [Hay14]. The reason for the small transport current may be the increase of cracks and impurity phases at the grain boundaries (GBs), which are present in these samples and are known to limit the current flow. The sample characteristics are summarized in table 2.1.

In this study, three different grain sizes are compared for each compound, namely an average grain size of below $1 \mu\text{m}$, as well as approximately 1 , and $3\text{--}5 \mu\text{m}$. If the grain size is not explicitly given, the samples will be refer to by „small“, „medium“, or „large“ for the different grain sizes. The given values represent a coarse estimation of the average grain dimensions (divided by 2), because of the statistically distributed grain sizes. The grain size of the medium and large grained samples was determined with a polarized light microscope and by electron microscopy techniques in case of the small grained samples. Most of the presented measurements of the small grained K doped samples result from the sample that is not indicated by „*.“ The sample geometry is mentioned explicitly if a measurement was conducted on one of the another samples.

The measured samples were sensitive to air. The Co doped samples degenerated within hours after opening the sealed quartz tubes in which they were shipped. Before the tubes were opened, the bulks showed a slightly metallic sheen, but immediately after the contact with air the surface turned to dark dull gray. Furthermore, the Co doped samples were prone to loose particles/grains at the surface during polishing, and they frequently broke apart after a typical temperature cycle (300 to 4 K and back).

The superconducting properties of the K doped samples also degenerated with time, but in their case this proceeded much slower. The maximum magnetization of the medium grained K doped sample was reduced by approximately 3% after six month and about 7% after two years. This deterioration of the superconductivity is the reason why the data in the various measurements slightly differ from each other, but a noticeable change of the superconducting properties was not observed.

2.1.1 Grain Size Distribution

Figures 2.1A and 2.1B show polarized light images of the sample surface of the medium and large grained K doped sample. The individual grains can be distinguished by the different shaded areas in the images. The brightness of the area depends on the orientation of the grain (confer figure 1.2), i. e. a bright shade for one orientation and a darker shade for a completely different orientation. These images were evaluated manually by choosing one column or row of the image. Along this line the brightness changes at the point where one grain is connected to another,

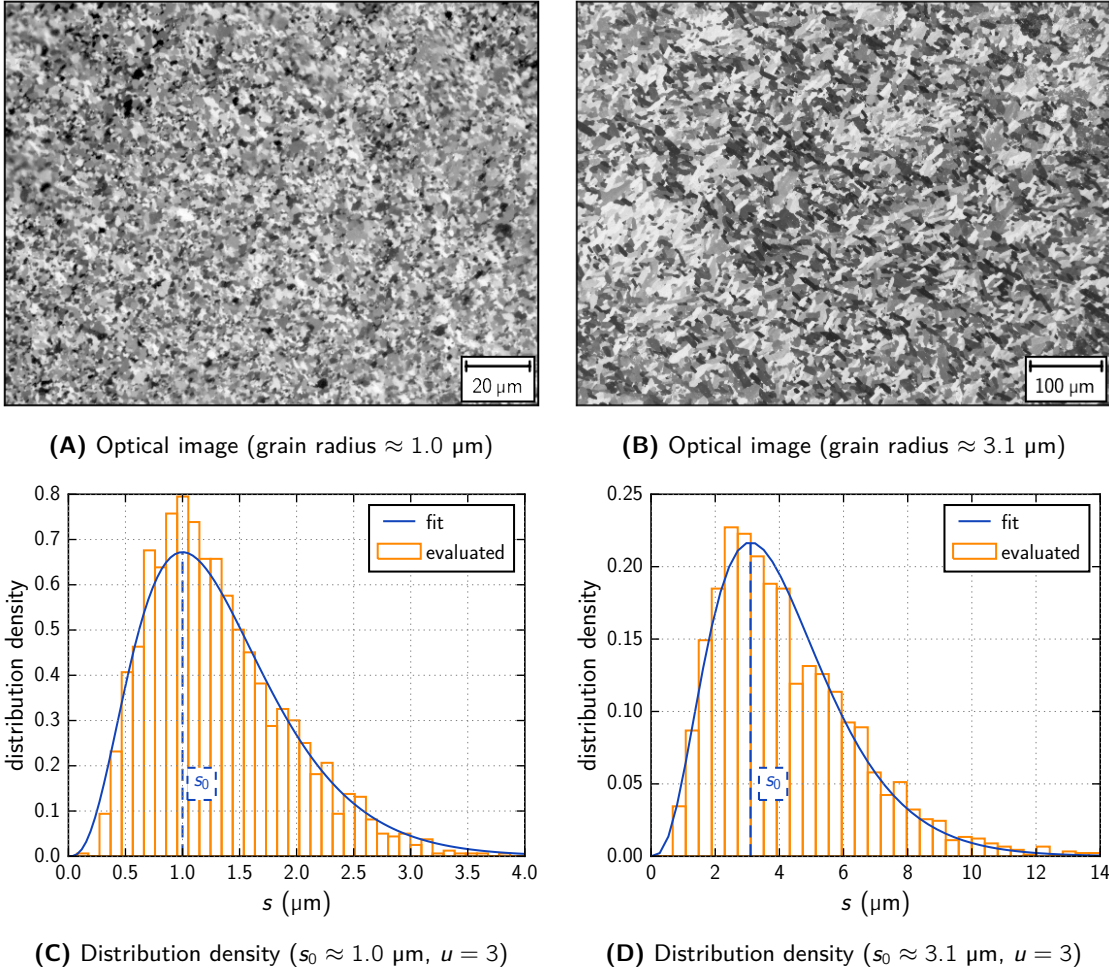


Figure 2.1: Images of the surface of the medium and large grained K doped samples (provided by J. D. Weiss) and the respective distribution densities, which were fitted by equation (2.1).

while it hardly changes inside a grain. The length s is determined by the distance between two neighboring changes in the brightness divided by 2. A multitude of lines have to be evaluated in this way to get a meaningful distribution of the grain size (about 5000 grains were identified). Figures 2.1C and 2.1D display the evaluated distribution densities of the two samples, which are fitted by the probability function:*

$$P(s, s_0, u) = \frac{1}{\Gamma(m)} \frac{s^u}{s_0^{u+1}} \exp\left(-\frac{us}{s_0}\right), \quad (2.1)$$

with $s \in [0, \infty)$, and Γ the gamma function. The parameter s_0 denotes the mode of the distribution density function, i.e. the value where P has a maximum, which is referred to as characteristic grain size in the following. In principle the dimensionless distribution function parameter (u) can take any value larger than 0, but it must be a natural number in order to get an analytical solution for the model that will be derived in chapter 4. The figures show that the distribution of the grain size can be described accurately by equation (2.1), where $u = 3$ for both grain sizes and the characteristic grain size $s_0 \approx 1.0 \mu\text{m}$ in case of the medium grained sample and $s_0 \approx 3.1 \mu\text{m}$ in case of the large grained sample.

* The equation resembles a gamma type distribution, but here the value s_0 is independent of u .

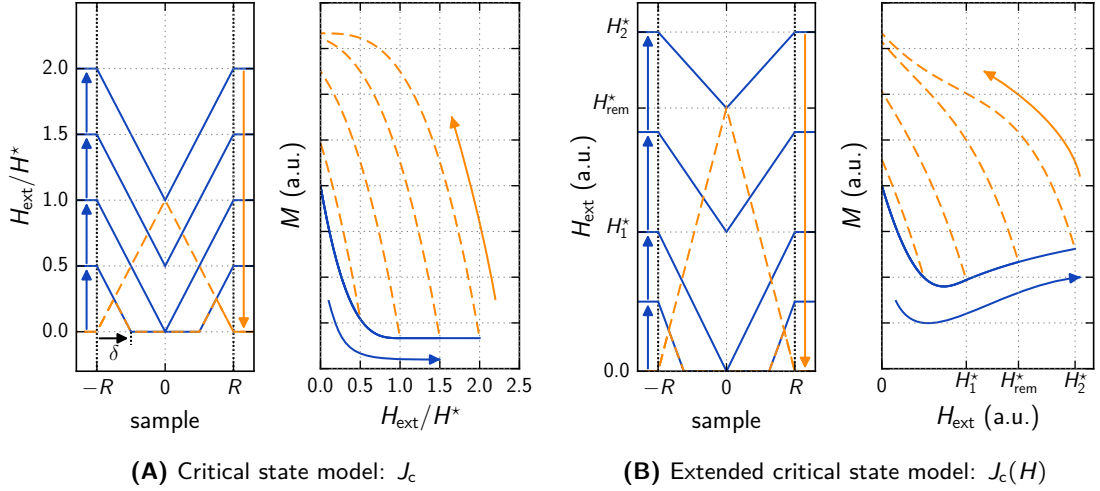


Figure 2.2: Hysteresis of the magnetic field inside a superconductor in dependence of an external applied field (H_{ext}) and the corresponding magnetization (M) for the critical state model and the extended critical state model, where the inter-grain current density (J_c) is field dependent. The vertical dotted lines in the left plots define the sample edges.

2.2 Magnetization Experiments

The magnetization of all samples were measured in a vibrating sample magnetometer (VSM) and a superconducting quantum interference device (SQUID) magnetometer. Different evaluation techniques were applied for each device, all with the aim to identify and, if possible, quantify the inter-grain current density (J_c) and intra-grain current density (J_{intra}) in the samples.

The easiest and most direct experiment to measure J_c is to apply an external current to the sample and record the current-voltage characteristic. In the superconducting state the voltage should be zero, because the resistance is zero. When J_c of the SC is reached the flux lines (FLs) start to move and a finite voltage is detected [See98]. This technique is limited to samples with a small cross section or a small J_c , otherwise very high currents are needed. In case of superconducting wires, which have a small superconducting cross section, this technique is convenient, but the investigated Ba-122 bulks would have to be cut to reduce the cross section. During this process a sample can be destroyed or its superconducting properties can be altered. Therefore, magnetization measurements are often applied for samples with large dimensions. These alternative techniques have the drawback that they do not provide the value of J_c directly. Instead, models have to be used to extract J_c (e. g. see Zehetmayer [Zeh09]).

In general, SCs exhibit a hysteresis in their magnetization, which originates from the current flow inside the sample. An instructive way to describe and visualize the hysteresis is the phenomenological model of the critical state introduced by Bean [Bea62]. In this model the current density in the Maxwell equation: $\nabla \times \mathbf{H} = \mathbf{J}$, is replaced by the constant J_c , the critical (inter-grain) current density.

Figure 2.2 shows the development of the field profile in a cylindrical sample of radius R (left graphs in the panels) and the corresponding magnetic signal (right graphs) according to the critical state model (figure 2.2A) and the extended critical state model (figure 2.2B). The difference between the models is the field dependence of J_c in the latter. After the sample is cooled below T_c (in zero field in this example), no field gradient is present because the FLs are homogeneously distributed (no FLs are present after zero field cooling). Such a field profile is referred to as an *initial field profile*, where the field distribution inside the SC is flat, as sketched in figure 2.3. FLs start to penetrate the sample at the edges when the H_{ext} is increased, as indicated

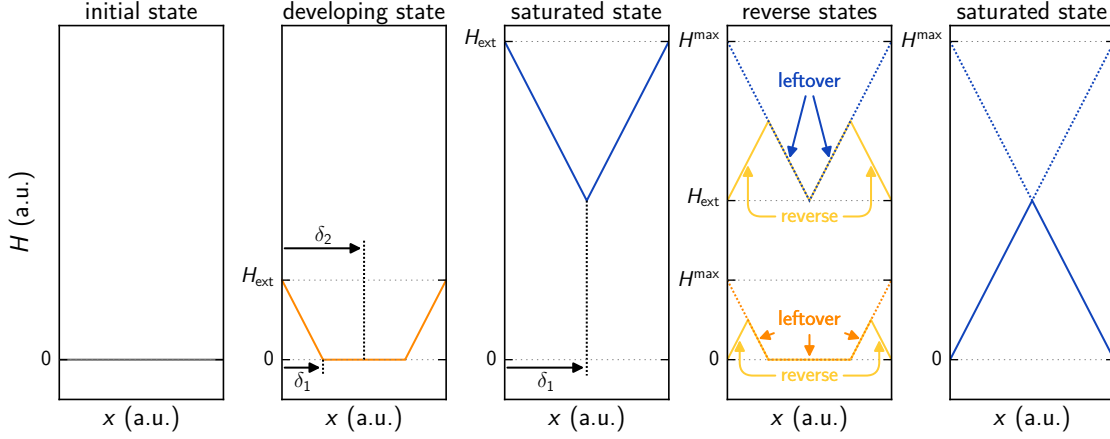


Figure 2.3: Graphical introduction of the terms defined in the text. The graphs show the development of field profiles inside a superconducting crystal in dependence of an external applied field (H_{ext}) and the maximum applied field (H^{max}).

by the upward arrows in the left graphs in figure 2.2. The FLs are driven towards the center, because the Lorentz force becomes larger than the pinning force and a FL gradient corresponding to J_c arises. The larger H_{ext} becomes, the further this FL gradient advances towards the sample center. The field range which describes the advance of the FL gradient and the disappearance of the initial field profile is referred to as a *developing field profile*, while a *saturated field profile* describes the rest of the increasing field range (cf. figure 2.3), where the change of H_{ext} has no effect on the sign of the local field gradient. The H_{ext} at which the field profile becomes saturated for the first time, is denoted as the penetration field (H^*) in the critical state model (figure 2.2A). H^* is defined by J_c and the sample radius R :

$$H^* = J_c R. \quad (2.2)$$

When H_{ext} is reduced from a certain maximum applied field (H^{max}), the FLs near the sample edges begin to move outwards because the Lorentz force originating from H_{ext} is reduced and the SC cannot contain as many FLs as at H^{max} . Similar to the case of an increasing H_{ext} , the pinning force hinders the FLs from exiting to some extent, so that J_c at the edges has the opposite sign. The reduction of H_{ext} and the resulting field profile inside the sample are indicated by the downward arrows and the dashed lines in figure 2.2. The more H_{ext} is reduced the further the reversed slope advances towards the sample center, thereby the leftover of the field profile originating from H^{max} is continuously replaced by the reversed slope. A field profile is referred to be in the *reverse state* while it has this features, as indicated by the field profiles titled „reverse states“ in figure 2.3.

To invert the saturated field profile in figure 2.2A, H_{ext} has to be reduced by at least $2H^*$, i. e. $H_{\text{ext}} \leq H^{\text{max}} - 2H^*$. When H_{ext} is reduced below $2H^*$ the field profile is saturated again (cf. figure 2.3), with the difference that the field slopes and therefore the value of the magnetization have the opposite sign. The saturated field profile is distinguished from the initial, developing and reverse field profiles, because it is independent from H^{max} and the field in which the sample was cooled below T_c , i. e. the magnetic response of the sample at a given field is always the same (except for the sign).

To determine the magnetic moment from a field profile the integral:

$$\mathbf{m} = \frac{1}{2} \int \mathbf{r}' \times \mathbf{J}(\mathbf{r}') \, d^3 r', \quad (2.3)$$

has to be solved, where the integration is carried out over the sample volume, and $\mathbf{J}(\mathbf{r}')$ defines the state of the field profile. For a cylindrical geometry with radius R and height $2c$, where H_{ext} is applied along the c -axis, and $\mathbf{J}(\mathbf{r}')$ is replaced by $J_c \mathbf{e}_\varphi$ (Bean-model), where \mathbf{e}_φ is the unit vector that defines the angular position in a cylindrical coordinate system, the (absolute) magnetic moment of a saturated field profile is given by:

$$m = J_c V \frac{R}{3}, \quad (2.4)$$

where $V = 2\pi R^2 c$ is the sample volume. The magnetic moment of a cubic sample: $2a \times 2b \times 2c$ with $a > b$, is calculated via [Wie92]:

$$m = J_c V \frac{b}{4} \left(1 - \frac{b}{3a}\right), \quad (2.5)$$

with $V = 8abc$. These equations can be used to approximate the magnetic moment of more sophisticated field profiles. The magnetic moment is rewritten as (cubic sample):

$$m_i = J_{c,i} \underbrace{8(a - \delta_i)(b - \delta_i)c}_{V_i} \frac{(b - \delta_i)}{4} \left(1 - \frac{b - \delta_i}{3(a - \delta_i)}\right) = J_{c,i} f(\delta_i), \quad (2.6)$$

where the parameter $\delta_i \in [0, b]$ defines the distance to the closest sample edge (cf. figure 2.3) and the index i identifies a slope of the field profile. A large value of δ_i indicates that the slope is closer to the sample center. The total magnetic moment of a field profile with N slopes, which are defined by $J_{c,i}$, is given by:

$$m = \sum_{i=1}^N J_{c,i} (f(\delta_{i-1}) - f(\delta_i)), \quad (2.7)$$

where $\delta_0 = 0$.

The field profiles in the left panel of figure 2.2A can be evaluated to a corresponding magnetization by applying equation (2.7), which is plotted in the right panel. Equation (2.7) becomes equation (2.5) when $\delta = b$, i. e. the magnetization saturates when the FL gradient first reach the sample center at H^* . Thus J_c can be extracted from a magnetization loop by finding the field at which m saturates:

$$J_c = \frac{H^*}{nb}, \quad (2.8)$$

where n is a dimensionless factor depending on the sample geometry [Pal07]. The respective factors for the samples can be found in table 2.1.

The critical state model is a simple and powerful tool to model the pinning of FLs in SCs, but it does not consider the dependence of J_c on the magnetic field, i. e. $J_c \rightarrow J_c(H)$. With the exception of the second peak effect [Zeh04], J_c of a type-II SC is a monotonic decreasing function of H_{ext} . Many empirical functions were devised to extend the critical state model in order to account for the field dependence of J_c . Xu, Shi, and Fox [Xu90] showed that the most prominent functions can be described by the more general equation:

$$J_c(H) = J_{c0} \left(1 + \frac{H}{H_0}\right)^{-\beta}, \quad (2.9)$$

where H_0 and β are material dependent parameters (in this chapter $\mu_0 H_0 = 1$ T and $\beta = 1$).

Figure 2.2B shows an example of how the development of the field profiles and the corresponding magnetic signal change in the extended critical state model compared to the critical state model. The characteristic penetration field H^* becomes field dependent, because of the field

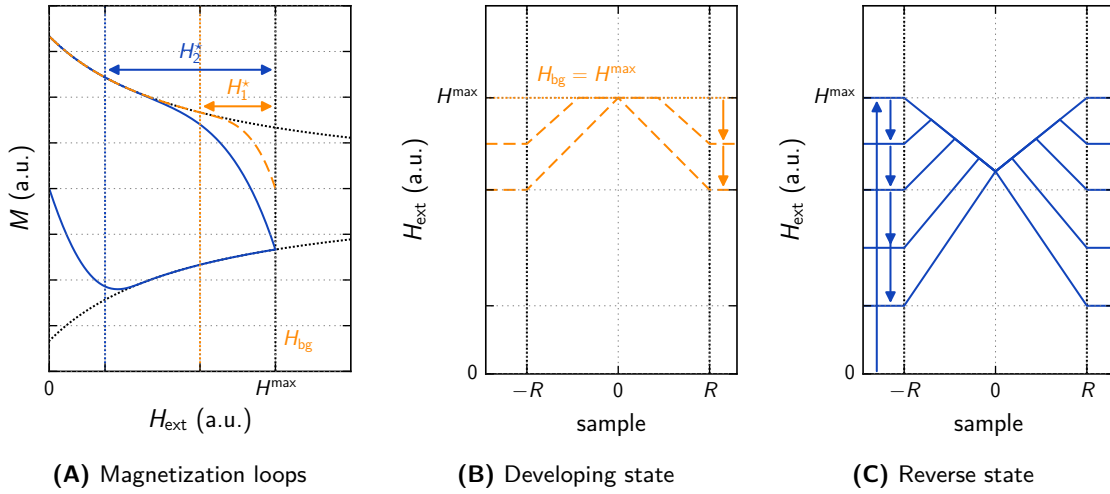


Figure 2.4: Magnetization loops (M) corresponding to the field profiles in the developing and reverse state. The dotted curve in A represents the field dependence of the magnetization of saturated field profile, while the vertical dotted lines in B and C define the sample edges.

dependence of J_c , and new values have to be defined. The first penetration field (H_1^*) describes the field at which the developing field profile becomes saturated for the first time, equivalent to H^* . This saturation of the field profile occurs shortly after the peak in figure 2.2B. Analogous to $2H^*$, the second penetration field (H_2^*) denotes the field difference between H^{max} and the field value at which a saturated field profile is completely inverted, i.e. in the field range $H^{\text{max}} - H_2^* < H_{\text{ext}} \leq H^{\text{max}}$ the field profile is in the reverse state and below $H^{\text{max}} - H_2^*$ the field profile is saturated.

2.2.1 Magnetization Loops

Until now only zero field cooling was considered. If a SC is cooled below T_c at the background field (H_{bg}), the additional applied field (H_{add}) is introduced:

$$H_{\text{add}} = H_{\text{ext}} - H_{\text{bg}}, \quad (2.10)$$

which describes the field difference between H_{bg} and H_{ext} . The definition of H_{add} is convenient because the developing state depends on H_{add} (and H_{ext} in the extended critical state model).

A SC behaves similar to other materials in its normal conducting state ($T > T_c$) when a magnetic field H_{bg} is present, i.e. the flux is more or less uniformly distributed in the sample. Then the sample is cooled below T_c and FLs begin to form out of this flux if the SC is of type-II (cf. section 3.1). If $H_{\text{bg}} > 0$ and a positive H_{add} is applied, FLs are pushed from the sample edges towards the center, similar to the discussion in figure 2.2. The difference to figure 2.2 is that H_{ext} has to be replaced by H_{add} . The critical current density on the other hand is still determined by H_{ext} and with it the characteristic fields H_1^* and H_2^* . The fact that H_1^* and H_2^* depend on H_{bg} and H_{add} can be exploited to determine $J_c(H)$.

The standard measurement to investigate the magnetic behavior of a SC is a magnetization loop. The sample is exposed to H_{ext} while the magnetic response is detected by a pick-up system. The strategy to measure $H_1^*(H)$ and $H_2^*(H)$ is evident when looking at figure 2.4. First, the field is ramped from the minimum field to the maximum field of the measurement device and back again. This field loop represents the field dependence of the saturated field profile in figure 2.4A (dotted line), i.e. if a magnetization equals this signal the field profile of the sample can be assumed to be completely saturated.

To measure H_1^* the sample is cooled below T_c at H_{bg} . Then the field is either increased or decreased. In figure 2.4B the field is decreased. The field difference between the point where the field profile becomes saturated and H_{bg} defines H_1^* , which is indicated in figure 2.4A for the corresponding magnetization measurement. J_c at the point where two magnetization loops start to overlap can be calculated with the relation:

$$J_c(H^{\max} - H_1^*) = \frac{H_1^*}{nb}. \quad (2.11)$$

H_2^* is extracted by first cooling the sample below T_c at zero field. Then, H_{ext} is ramped to a sufficient value so that a saturated field profile is present in the sample and subsequently H_{ext} is ramped back to zero, as illustrated in figure 2.4C. Here, the field difference between H^{\max} and the point at which the magnetization matches the loop of the saturated field profile corresponds to H_2^* :

$$J_c(H^{\max} - H_2^*) = \frac{H_2^*}{nb} - J_c(H^{\max}), \quad (2.12)$$

which is indicated in figure 2.4A. At high fields, the field dependence of J_c is small and equation (2.12) can be approximated by: $J_c \approx H_2^*/(2nb)$, which is sufficiently accurate for a courses estimation.

Another widely used way to extract J_c from a magnetization loop is to measure the magnetization during a run from the maximum to the minimum field (M_+), and from the minimum to the maximum field (M_-). By calculating $(|M_+| + |M_-|)/2$ only the irreversible contribution to the signal remains in a first order approximation and with equation (2.5) (rectangular sample geometry) the corresponding J_c can be estimated [Zeh09].

2.2.2 Residual Magnetization

The measurement of the residual magnetization (M_{res}) is a technique that is closely related to field loops. Figure 2.5A shows the measurement approach. After cooling the sample below T_c at H_{bg} a certain maximum additional applied field is set:

$$H_{add}^{\max} = H^{\max} - H_{bg}. \quad (2.13)$$

Then the field is reduced to its initial value, H_{bg} , where the magnetic signal, $M_{res}(H_{add}^{\max})$, is recorded. This field cycle leads to the development of a field profile in the sample when the field is ramped to H_{add}^{\max} , which is reversed at the sample edges by going back to H_{bg} (cf. figure 2.3). In principal H_{add}^{\max} can be positive or negative, but in this thesis H_{add}^{\max} is always positive while H_{bg} can take any value.

The arrows in figure 2.5A indicate one measurement circle from H_{bg} to H_{add}^{\max} and back. A complete measurement of M_{res} repeats such a loop multiple times for different $H_{add,i}^{\max}$, where $i = 1, 2, \dots$. Thereby, the value of $H_{add,i}^{\max}$ increases after each field loop, i. e. $H_{add,i+1}^{\max} > H_{add,i}^{\max}$. The saturation of M_{res} occurs at H_2^* .

A typical measurement is shown in figure 2.5B. M_{res} at H_{bg} is plotted in dependence of H_{add}^{\max} for the critical state (J_c) and the extended critical state model ($J_c(H)$). The right plot displays the corresponding derivative of M_{res} . The measurement of M_{res} provides information on the history dependence (H_{add}^{\max}) of J_c at a certain field H_{bg} : $J_c(H_{bg}, H_{add}^{\max})$, and on H_2^* .

In case of a polycrystalline sample the models that have to be used to extract J_c and the J_{intra} are more elaborated than for crystals. Some works The experiments described above consider a uniform current density in the sample. This is not true in polycrystals with weakly linked GBs, where J_c and J_{intra} may change with the position. These two current densities can influence each other, which makes their quantitative separation more sophisticated [Mul94; Ni11]. The basic principles, how J_c and J_{intra} can influence each other are discussed in chapter 3 and 4.

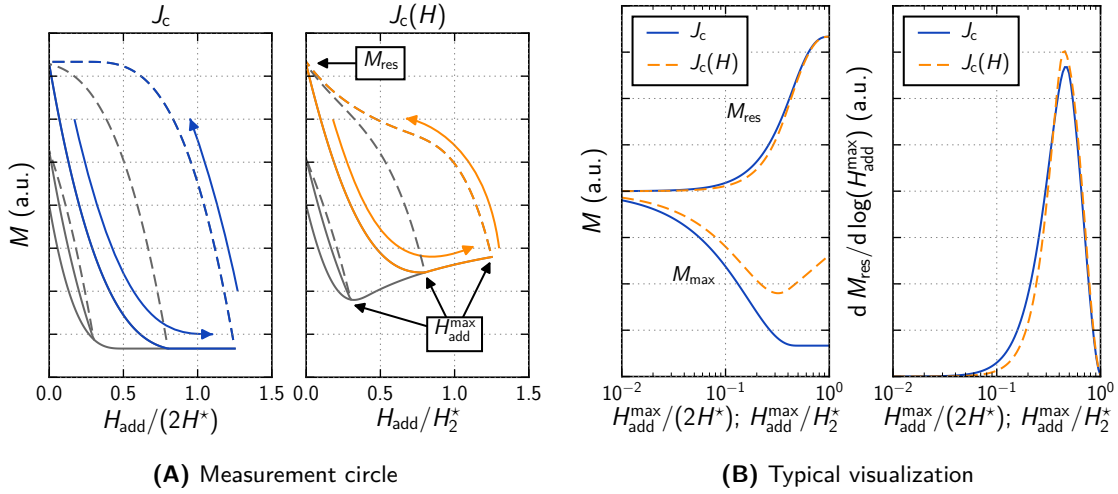


Figure 2.5: Approach and the typical visualization of the results of the measurement of the residual magnetization (M_{res}) for the critical state (J_c) and the extended critical state model ($J_c(H)$). M_{max} represents the magnetization recorded at the maximum additional applied field ($H_{\text{add}}^{\text{max}}$).

2.3 Scanning Hall-Probe Microscope

Magnetometer set-ups, such as a VSM or a SQUID, measure the global magnetic response of the sample, which can be used to estimate the magnitude of the currents, but they provide no information on the spatial distribution of the magnetic field and a separation of J_c and J_{intra} is extremely sophisticated, as will be shown later.

The scanning Hall-probe microscope (SHPM) [Boe03] is a passive measurement technique that interacts very little with the sample, because the applied currents and their generated magnetic fields are small. It can be operated in low and high fields of several Tesla. A big advantage of a SHPM is the direct measurement of the spatial distribution of the magnetic field. Other scanning probe techniques, such as magnetic force microscopy, detect this quantity indirectly so that complicate calculations have to be applied to extract the magnetic field. A Hall-probe is able to operate in the temperature range of μK to over 300 K. The active area of Hall-probes can be fabricated to be smaller than $1 \mu\text{m}^2$. In standard systems samples only have to be placed in the set-up once and then various measurement conditions can be applied. During an SHPM measurement the Hall-probe is moved in close proximity to the sample surface and the change of the voltage of the probe, due to the changes of the local field, gives a quantitative two-dimensional map of the magnetic field distribution.

In superconductivity, SHPMs are utilized for recording the magnetic field/flux distribution of different materials and geometries [Hen09]. For coated conductors the SHPM provides information about the uniformity of the pinning and the connectivity of the grains. For this purpose the measured field maps are often used to calculate the local current distribution throughout the sample. Thus, the “good” areas can be distinguished from the “bad” ones. In combination with structural analyzing techniques, including optical and electron microscopy, the field maps help to improve the SC. In contrast to this, the widely used transport current measurements of long samples only allow to draw conclusions about the weakest section of the conductor.

The developed set-up was intended to be applicable for different geometries (e.g. film, tap, or bulk), wherefore certain requirements had to be met. The main idea behind the system was to find interesting spots in a relatively large sample, which can then be scanned in detail by the same instrument. For this large area scans, the set-up must have the ability to measure large areas in an acceptable time span and small areas with a high spatial resolution. An evaluation

where the detection of a large area is necessary is the inversion of the field profile [Hen09], where the measurement area has to be larger than the sample to prevent computational artifacts in the results.

The distance between the sample surface and the active area of the Hall-probe should be as small as possible in order to resolve small structures. Thus, a reliable and precise distance control had to be implemented. The dimensions of the sensor should be as small as possible since the resolution of an SHPM depends on the size of the active area of the Hall-probe. The set-up utilizes Hall-probes with an active area of $400 \times 400 \text{ nm}^2$, which are provided by *MagCAM*.

A considerable problem of Hall-probes with such a small sensor is that the two-dimensional electron gas is very sensitive to magnetic particles that deposit on or near the active area. During some measurements the Hall-constant suddenly increased, because of the loss of electrons. The cause for this problem is unknown, but these jumps were more frequent shortly after cooling the system. Also, low resistive contacts at the voltage and current leads and a clean active area, i. e. when a Hall-probe is mounted the first time, seem to prevent the jumps. Another problem is that the thickness of the active area is only a few nanometer which is why surface irregularities or loose grains may damage or even destroy the Hall-probe, thus the sample has to be polished beforehand.

The calibration of the Hall-probe has to be done before and/or after a measurement to ensure the correctness of the Hall-constant, which is used to recalculate the measured voltage into a magnetic induction. This is done by recording the voltage at various applied fields during a field run. By fitting a line through the resulting data the conversion factor between voltage and field is evaluated.

2.3.1 Set-Up

The cryostat in which the experiment is located is constructed as a system with many cylindrically arranged layers. An outer vacuum chamber separates a liquid nitrogen reservoir from the environment. The liquid nitrogen reservoir encloses another vacuum chamber that separates it from a helium reservoir. The variable temperature insert is located inside this 20 L liquid helium reservoir together with a liquid helium level meter and an 8 T Nb-Ti superconducting magnet which is operated in non-persistent mode. The temperature in the sample chamber can be stabilized between 2.5 and 150 K.

The actual SHPM device, shown in figure 2.6 is attached to the lower end of a sample rod which is put into the variable temperature insert. The measurement chamber incorporates three linear piezo-positioners to enable the mapping of the magnetic induction in all three space dimensions. They form a stack, where the z -positioner is located at the bottom of the sample chamber while the x and y -positioner are fixed to the top so that they hang into the chamber. The holder for the cantilever is attached to the y -positioner (figure 2.6B). The surface of the holder which is not in contact with the y -positioner is slanted by an angle of 3° (visible in the right picture of figure 2.6B). The angle is necessary to ensure a sufficiently small distance between the tip of the Hall probe, i. e. the active area, and the sample surface. Furthermore, it has the purpose to guaranty that the point where the Hall-probe comes in contact with the sample surface is the tip of the Hall-probe. The sample is placed on a plate which in turn is screwed on the z -positioner. The gap between the Hall-probe and the z -positioner can be varied with „spacers“, that allow the measurement of thin and thick samples. After the whole measurement chamber is assembled a temperature sensor is placed as close as possible to the sample, but far enough away to prevent any interference with the movement of the positioners.

The piezo-positioners were purchased from *attocube systems AG*. The working principle is based on the „impact drive mechanism,“ which utilizes static friction and impulsive force to move. The positioner consists of three parts: one part is the piezo-element that is attached to a guiding rod to which a plate is loosely connected. If the piezo expands slowly, the friction between guiding rod and the plate is large enough to translate the plate. For quick expansion the friction

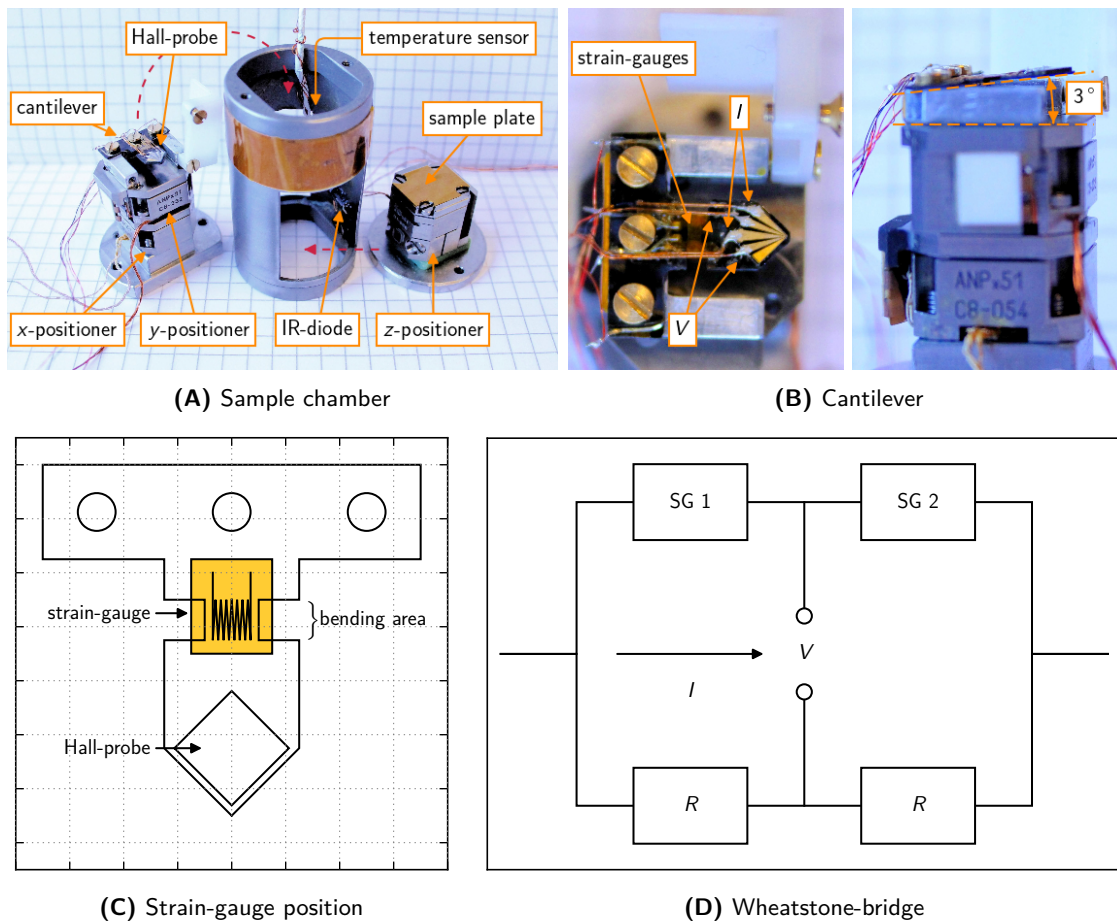


Figure 2.6: Setup of the scanning Hall-probe microscope.

is not sufficient to move the plate, i. e. the guiding rod slips through the holding mechanism of the plate. The lateral movement is achieved by alternately expanding the piezo slowly and then rapidly going back to the initial position. The absolute position of the positioner is read out with a resistive encoder. The scan range of the positioners is approximately 3 mm and the spatial resolution is about 1 μm .

A carbon-fiber plate acts as a cantilever that controls the distance between the active area of the Hall-probe and the sample surface. Figure 2.6C shows the „T-shape“ of the cantilever. The upper part with the three circles is intended for the attachment to the cantilever-holder and the y -positioner. Two strain-gauges are glued on the top and the bottom of the bending area so that they can detect a bent of the carbon-fiber plate. In this area the width of the cantilever is reduced to have a weak spot while the rest of the cantilever is comparatively stiff. When the Hall-probe gets in contact with the sample surface the cantilever is preferably bent at this bending area.

The strain gauges are part of a Wheatstone-bridge as shown in figure 2.6D. A constant current is applied to the bridge and the voltage is detected with a micro-voltmeter. The two resistors in the figure are connect in parallel to the strain-gauges. Their electric resistivity is approximately the same as the resistance of the strain-gauges. With low-noise resistors surface irregularities of about 1 μm can be detected with the cantilever.

The Hall-probe is located at the tip of the carbon plate (figures 2.6B and 2.6C). The current tracks (labeled I) and the voltage tracks (labeled V) are marked in figure 2.6B*. The applied

* The lower track of the Hall-probe in figure 2.6B is connected to a tunneling tip that is not used.

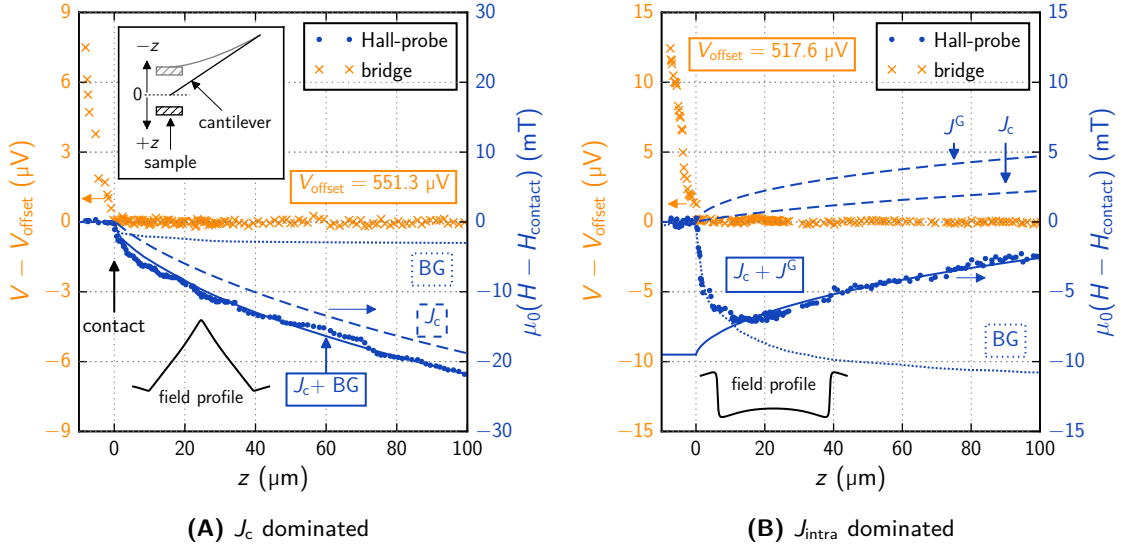


Figure 2.7: Position dependence of the Wheatstone bridge circuit voltage (left axes) and the magnetic field above the center of the medium grained sample (right axes). Inter-grain current density (J_c) is dominant in A, because the measurement was conducted for a saturated field profile on the decreasing field branch at 0.03 T and 5 K. In contrast to this, the measurement in B shows the z -dependence of the field at one point above a saturated field profile on the increasing field branch at 0.17 T, where the contributions of the intra-grain current density (J_{intra}) are dominant.

currents usually lie between 1 to 10 μA , as required by the magnetic signal of the sample. The Hall-probes utilize a two-dimensional electron gas in the active area, which is prone to the spontaneous „loss“ of the carrier electrons. This means that a certain number of electrons can no longer contribute to the current transport and as a consequence the Hall-constant increases. Thus an infrared diode is incorporated in the system to illuminate the Hall-probe in order to „reactivate“ these electrons.

The constructed SHPM combines a large temperature range, a high field resolution due to the use of state-of-the-art Hall-probes with a small active area, and piezo-positioners that allow a high spatial resolution. Furthermore, a wide field range of ± 8 T is accessible. All these points enable the set-up to be utilized in a wide field of experiments.

2.3.2 Distance

The magnetic signal of a sample depends on the distance between the Hall-probe and the sample surface. Thus, the distance should be known as accurately as possible to avoid errors in the evaluation. The SHPM utilizes strain-gauges together with a Wheatstone bridge circuit (cf. section 2.3) to find the z -position where the Hall-probe comes in contact with the sample. The detected voltage from the Wheatstone bridge is approximately constant when the Hall-probe is not in contact, but it changes rapidly when the cantilever is bent, as indicated in figure 2.7. The offset voltage (V_{offset}) is subtracted from the data, because its value changes with H_{ext} . H_{ext} was 30 mT during the measurement shown in figure 2.7A and 170 mT in figure 2.7B. The zero position ($z = 0$) defines the point of the contact. Positive values specify the relative distance between the Hall-probe and the sample. Negative values represent the bending of the cantilever, when the Hall-probe is in contact with the surface (cf. inset in figure 2.7A).

In addition to the voltage of the Wheatstone bridge, the figures display the distance dependence of the local field above the medium grained sample, at 5 K. Figure 2.7A shows the

dependence of the detected field for a saturated field profile on the decreasing field branch, where J_c is dominant (dots). The Hall-probe was positioned at the sample center during the measurements, so that the difference between H_{ext} and the local field is maximal. The field where the Hall-probe is in contact with the surface is $\mu_0 H_{\text{contact}} = 88 \text{ mT}$ ($\mu_0 H_{\text{ext}} = 30 \text{ mT}$).

The dashed curve in figure 2.7A indicates the z -dependence of the inter-grain signal (labeled J_c). This curve is calculated by using the equations in chapter 5 and the J_c obtained from fitting the field profile, which was measured subsequently. It represents the expected decrease of the field at the sample center when the distance between surface and Hall-probe is changed. The comparison to the actual measurement reveals an unexpected increase of the local field before the contact which leads to a constant offset between the expected and the actual field dependence.

Another measurement was conducted at 40 K to record the distance dependence of the Hall-voltage above T_c , which is plotted as a dotted line. This measurement is referred to as background. It changes rapidly when the Hall-probe is less than 20 μm away from the surface, which explains the unexpected increase of the voltage before contact, and is approximately constant at larger distances. The field is $\mu_0 H_{\text{contact}} = 33.4 \text{ mT}$ (40 K) when the Hall-probe is in contact with the surface, which is larger than $\mu_0 H_{\text{ext}} = 30 \text{ mT}$. The superposition of the expected z -dependence of the inter-grain signal and the background (line in figure 2.7A) shows a good agreement with the experimentally observed behavior.

Figure 2.7B shows the z -dependence of the Hall-voltage for a saturated field profile that is dominated by J_{intra} . The expected behavior of the magnetic field is plotted as a dashed line, where J_c and J_{intra} were evaluated from a subsequent measurement of the field profile. The background was measured at 40 K and is shown as a dotted line. The field at which the Hall-probe is in contact with the surface is 156 mT at 5 K and 181 mT at 40 K ($\mu_0 H_{\text{ext}} = 170 \text{ mT}$). The sudden increase of the local field before the contact is again ascribed to the background and the increase of the field at $z > 20 \mu\text{m}$ is in acceptable agreement with the expected behavior.

The increase of the background with H_{ext} is in good agreement with the increase of M with H_{ext} at 40 K (measured in a VSM). This indicates that the background is non-superconducting and that it does not vanish below T_c .

The origin of the background could be the change of the angle of the Hall-probe when it is in contact with the surface. Before the contact, the angle is about 3° , but during contact this angle changes with the z -position and with it the value of the detected field. Assuming that this is the case in the distance measurements shown in figure 2.7, the actual point of the contact is not located at the position where the field becomes constant, but rather sooner (i. e. $z \approx 20 \mu\text{m}$). The bending of the cantilever then reduces the angle between Hall-probe and surface (cf. inset in figure 2.7A). The change of the angle from 3° to 0° would result in a change of the detected field of less than 1%. In case of the measurements the signal increases about 3.4% in figure 2.7A and 6.5% in figure 2.7B, which makes this explanation unlikely.

The most probable reason for the observed background is the granularity of the sample, i. e. the influence of the individual grains and impurities becomes larger when the Hall-probe is near the surface. Additional measurements were carried out, where the z -dependence of the field was recorded at different xy -positions. These measurements exhibit small changes in the distance dependence in close proximity to the surface (i. e. the background), while the dependence at larger distances changes only marginally (i. e. the field profile). This observation and the fact that the background is present below and above T_c support the assumption that non-superconducting impurities cause the background.

2.3.3 Magnetic Impurities

Figure 2.8A shows an area scan of the medium grained K doped sample, where magnetic structures with a spacial extend of about 10 μm can be identified. A priori, this structures could belong to grains or grain clusters with strong pinning centers. Their size is about 10 times larger than the characteristic grain size ($s_0 = 1 \mu\text{m}$).

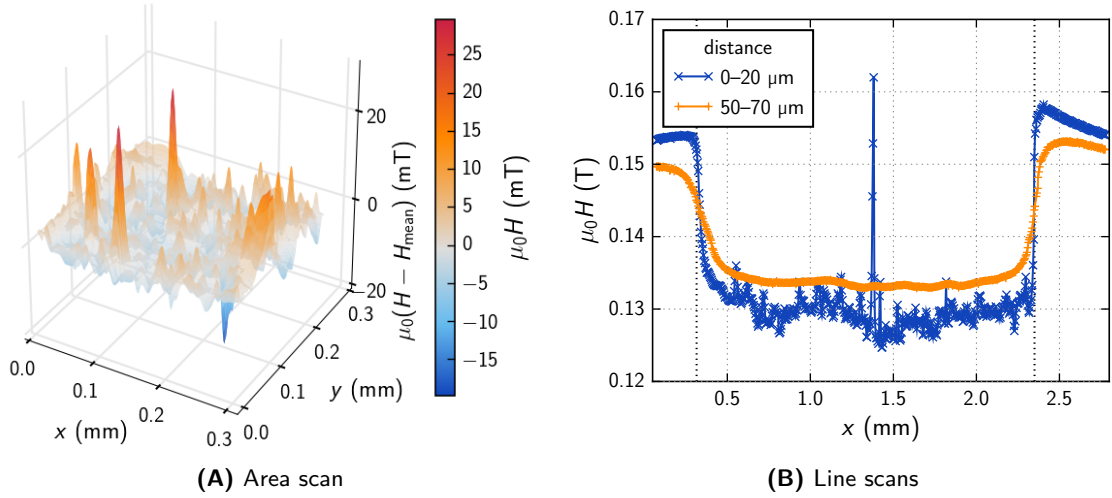


Figure 2.8: Scan of an area in close proximity to the surface near the center of the medium grained sample and a line scans of the same sample with varying distance to the surface. The measurements were carried out at 5 K and the external applied field was ramped from -0.15 to 0.15 T, where the measurements were carried out. H_{mean} in A is the mean value of all data points.

The two line scans in figure 2.8B are recorded under similar conditions. During one scan the distance between the sample surface and the Hall-probe was approximately $20 \mu\text{m}$ at the left sample edge and 0 at the right edge. The distance was increased by $50 \mu\text{m}$ for the second scan. The first line scan shows field-peaks above the sample, where the peak near the sample’s center exhibits a higher value than H_{ext} . This indicates the presence of a secondary phase at that location, which is either ferro- or paramagnetic.

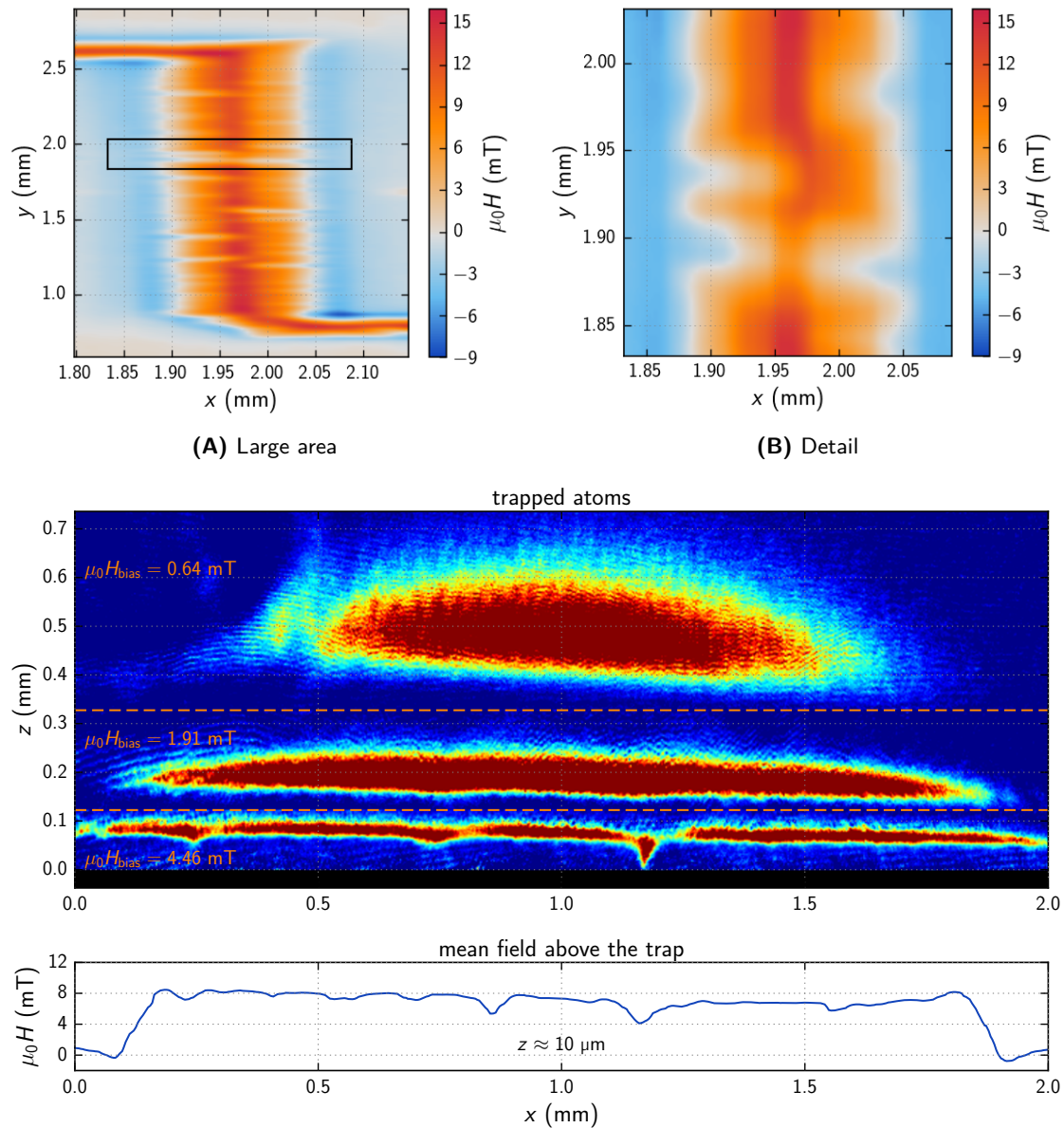
These impurities can be identified in the SHPM scans, because the slope of the field profile of a superconducting grain is preserved as long as H_{ext} is ramped in a certain direction, while the slope of the field profile of an impurity changes from positive to negative (or vice versa) when H_{ext} is ramped through zero. Such secondary phases occurred regularly in the samples, which made the evaluation of J_{intra} from measurements such as figure 2.8A unreliable.

2.3.4 An Exemplary Measurement

Figure 2.9 shows an exemplary measurement of a niobium thin-film superconductor used to trap atoms in a magnetic field [Min14]. A typical SHPM scan procedure is to first measure a large area of the sample (figure 2.9A) with a sufficiently small distance between the individual measurement points, i. e. the step width, to detect interesting structures. In figure 2.9A, the area of interest was near $y = 1.5$ mm, where the trapped field of the Nb-film is comparatively small.

Figure 2.9B displays the detailed scan of this area. The upper image in figure 2.9C shows the trap at a constant current through the chip. Different bias field values (H_{bias}) were used to move the atoms closer to the chip surface, which is located at $z = 0$. The lower image shows the average field above the film, where the value at a certain x -position is calculated from all data points in the interval $y = 1.6$ to 1.8 mm in figure 2.9A. The closer the atoms get to the film the more details of the film inhomogeneities, which are visible in the lower image, are reproduced. Figure 2.9 gives a nice example for the usefulness of the SHPM for other fields in physics.

Thin-films on a smooth substrate fulfill the requirement of a flat sample surface, which is beneficial in many ways. Firstly a smooth surface, that is parallel to the xy -scan plane, reduces the measurement time because the z -positioner does not have to compensate the slope or a surface roughness. Furthermore, an uneven surface is more likely to damage the active area of the Hall-



(C) Comparison between the distribution of the trapped Rubidium atoms and the mean field above the film.

Figure 2.9: scanning Hall-probe microscope measurement of a niobium thin-film used to trap Rubidium atoms. The rectangle in the large area scan indicates the scan area shown in the more detailed scan. The field distribution above the film is compared to the distribution of the trapped atoms in C. (The image titled „trapped atoms“ was provided by F. Diorico and S. Minniberger.)

probe and the measured data is also sensitive to the distance between Hall probe and sample surface. Therefore, polishing samples with rough surfaces is important.

References

- [Bea62] C. P. Bean (1962): „Magnetization of Hard Superconductors“ *Phys. Rev. Lett.* **8**, 250.
- [Boe03] G. Boero, M. Demierre, P.-A. Besse, and R. S. Popovic (2003): „Micro-Hall devices: performance, technologies and applications“ *Sensors and Actuators A: Physical* **106**, 314
[Proceedings of the 4th European Magnetic Sensors and Actuators Conference].
- [Hay14] Y. Hayashi, A. Yamamoto, H. Ogino, J. Shimoyama, and K. Kishio (2014): „Influences of material processing on the microstructure and inter-granular current properties of polycrystalline bulk $\text{Ba}(\text{Fe},\text{Co})_2\text{As}_2$ “ *Physica C* **504**, 28
[Proceedings of the 26th International Symposium on Superconductivity].
- [Hen09] F. Hengstberger, M. Eisterer, M. Zehetmayer, and H. W. Weber (2009): „Assessing the spatial and field dependence of the critical current density in YBCO bulk superconductors by scanning Hall probes“ *Supercond. Sci. Technol.* **22**, 025011.
- [Min14] S. Minniberger, F. Diorico, S. Haslinger, C. Hufnagel, C. Novotny, N. Lippok, J. Majer, C. Koller, S. Schneider, and J. Schmiedmayer (2014): „Magnetic conveyor belt transport of ultracold atoms to a superconducting atomchip“ *Appl. Phys. B* **116**, 1017.
- [Mul94] K.-H. Müller, C. Andrikidis, H. K. Liu, and S. X. Dou (1994): „Intergranular and intragranular critical currents in silver-sheathed Pb-Bi-Sr-Ca-Cu-O tapes“ *Phys. Rev. B* **50**, 10218.
- [Ni11] B. Ni, J. Ge, Y. Tanaka, E. S. Otabe, M. Kiuchi, T. Matsushita, Z. Gao, L. Wang, Y. Qi, X. Zhang, and Y. Ma (2011): „Estimation of Critical Current Densities in Polycrystalline $\text{Sr}_{0.6}\text{K}_{0.4}\text{Fe}_2\text{As}_2$ Superconductors“ *IEEE Trans. Appl. Supercond.* **21**, 2862.
- [Pag10] J. Paglione (2010): „High-temperature superconductivity in iron-based materials“ *Natur Phys.* **6**, 645.
- [Pal07] A. Palau, T. Puig, X. Obradors, and Ch. Jooss (2007): „Simultaneous determination of grain and grain-boundary critical currents in $\text{YBa}_2\text{Cu}_3\text{O}_7$ -coated conductors by magnetic measurements“ *Phys. Rev. B* **75**, 054517.
- [See98] B. Seeber (1998): *Handbook of Applied Superconductivity*. ISBN: 9781420050271.
- [Wei13] J. D. Weiss, J. Jiang, A. A. Polyanskii, and E. E. Hellstrom (2013): „Mechanochemical synthesis of pnictide compounds and superconducting $\text{Ba}_{0.6}\text{K}_{0.4}\text{Fe}_2\text{As}_2$ bulks with high critical current density“ *Supercond. Sci. Technol.* **26**, 074003.
- [Wie92] H. P. Wiesinger, F. M. Sauerzopf, and H. W. Weber (1992): „On the calculation of J_c from magnetization measurements on superconductors“ *Physica C* **203**, 121.
- [Xu90] M. Xu, D. Shi, and R. F. Fox (1990): „Generalized critical-state model for hard superconductors“ *Phys. Rev. B* **42**, 10773.
- [Zeh09] M. Zehetmayer (2009): „Simulation of the current dynamics in superconductors: Application to magnetometry measurements“ *Phys. Rev. B* **80**, 104512.
- [Zeh04] M. Zehetmayer, M. Eisterer, J. Jun, S. M. Kazakov, J. Karpinski, B. Birajdar, O. Eibl, and H. W. Weber (2004): „Fishtail effect in neutron-irradiated superconducting MgB_2 single crystals“ *Phys. Rev. B* **69**, 054510.

Chapter 3

Modeling Intra-Grain Currents

*If I told you I've worked hard to get where I'm at, I'd be lying,
because I have no idea where I am right now.*

— Jarod Kintz, *This Book is Not FOR SALE*

The intra-grain current density (J_{intra}) defines the part of the total current flow of a polycrystalline sample, that flows within the grains, while the inter-grain current density (J_c) flows from one grain to another, thereby passing the grain boundaries (GBs). The grains can be treated as a collection of separated crystals if no J_c flows in the sample. In the presence of J_c the individual grains are still describable with the equations that characterize a crystal, but J_c leads to a field gradient inside the sample that changes the local field at the GBs depending on the grain's location. Therefore the global response of a polycrystalline sample is a sum of the local magnetizations of the grains.

3.1 Crystals

Every superconductor (SC) shares the fundamental property to expel magnetic flux when it is cooled below the superconducting transition temperature (T_c) in a small external applied field (H_{ext}). This flux expulsion is caused by the emergence of a current density that shields the inside of the SC from the field [Lon35], i. e. the shielding current density. It flows in a small region of the width λ near the surface. This length is called the magnetic penetration depth, which is a characteristic parameter of a SC. The shielding effect was discovered by Meißner and Ochsenfeld [Mei33] and will be referred to in this thesis as Meißner state. When H_{ext} is increased, the shielding current density increases as well, but at a critical field H_c the superconducting state breaks down and the material becomes normal conducting. SCs which exhibit this behavior are called type-I SCs. In a type-II SC, flux lines (FLs) can form when H_{ext} is increased above the lower critical field (H_{c1}). Below H_{c1} these kind of SCs are in the Meißner state, where only the shielding currents flow, similar to SCs of type-I. FLs penetrate the SC between H_{c1} and the upper critical field (H_{c2}), and above H_{c2} the SC becomes normal conducting.

To describe the occurrence of type-I and type-II superconductivity as well as the existence of FLs Ginzburg and Landau used an additional, material dependent, characteristic length ξ [Gin04]. This coherence length provides information on the variation of the superconducting order parameter ψ . If the ratio $\kappa = \lambda/\xi$ is smaller than $2^{-1/2}$ the material is a type-I and otherwise a type-II SC, where FLs may be formed. A FL is a cylindrical object which contains one flux quantum $\Phi_0 = 2.07 \cdot 10^{-15}$ Vs. The normal conducting FL cores have a radius of the order of ξ and repel each other because of the circular (shielding) currents that are flowing around the cores. As a result of the repulsion, the FLs form a hexagonal lattice in the SC, the so-called

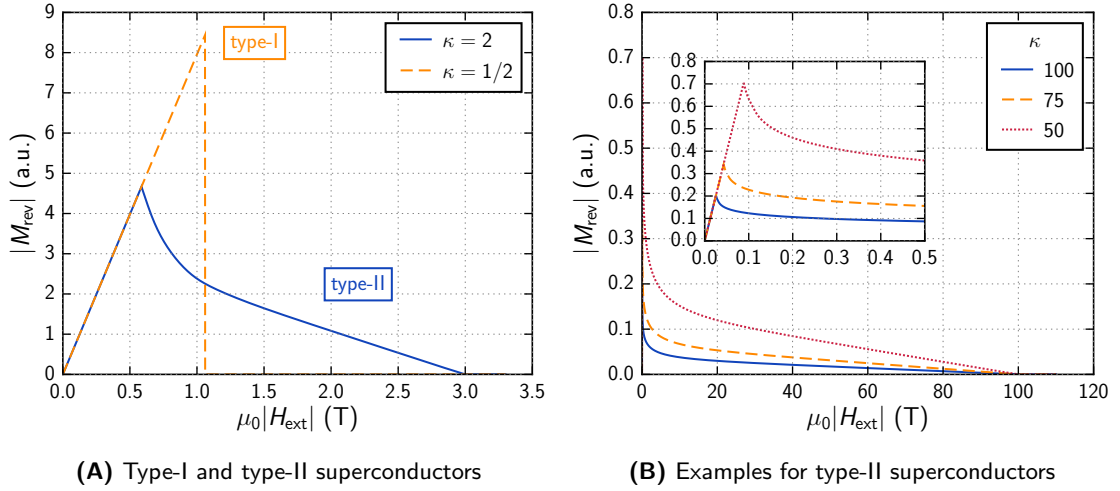


Figure 3.1: Comparison of the reversible magnetization (M_{rev}) of type-I and type-II superconductors and the M_{rev} of type-II materials for different κ .

FL lattice [Abr04]. The magnetic responses plotted in figure 3.1A are exemplary for type-I and type-II SCs. The values of the critical fields depend on λ and ξ and are given by [Bra95]:

$$\mu_0 H_{c1} \approx \frac{\Phi_0}{2\pi\lambda^2} (\ln(\kappa) + 0.5), \quad \mu_0 H_c = \frac{\Phi_0}{\sqrt{8\pi\xi\lambda}}, \quad \text{and} \quad \mu_0 H_{c2} = \frac{\Phi_0}{2\pi\xi^2}. \quad (3.1)$$

High-temperature superconductors (HTSs) exhibit fundamental differences compared to the low-temperature superconductors (LTSs). The former have a crystal structure in which the superconducting layers are located parallel to the crystallographic ab -planes and are separated by a priori non-superconducting layers. This structural anisotropy leads to an anisotropy in the parameters λ and ξ [Dew01]. In isotropic LTS λ and ξ describe the material whereas the anisotropic HTSs have four characteristic lengths [Cle98]. Along the c -axis the values λ_c and ξ_c are used and λ_{ab} and ξ_{ab} in the ab -planes, where $\lambda_c > \lambda_{ab}$ and $\xi_c < \xi_{ab}$. The anisotropy is usually described by the parameter γ or ε , which are defined as [Cle98]:

$$\gamma = \frac{1}{\varepsilon} = \frac{\lambda_c}{\lambda_{ab}} = \frac{\xi_{ab}}{\xi_c}. \quad (3.2)$$

3.1.1 Reversible Properties

The magnetization curves in figure 3.1B represent M_{rev} of a type-II SC, which terms the magnetic signal of a perfectly „clean“, and infinitely large sample. In this context clean denotes a perfect crystal, i.e. a SC without any inhomogeneities in its crystal structure. An illustrative interpretation of M_{rev} is the distribution of the FLs inside the material. When H_{ext} is larger than H_{c1} , FLs form at the sample surface. Because the FLs encounter no crystal defects which may act as pinning centers (cf. to section 3.1.2) they can move freely through the material until they reach an equilibrium position. Every time a new FL penetrates the sample this equilibrium is disturbed and all FLs in the SC have to reposition themselves so that the total energy of the system is minimized and thus the total force acting on the FLs is zero. The resulting FL lattice depends on the geometry of the sample and the number of FLs [Bae02]. In case of a SC with infinite dimensions the FL lattice is hexagonal.

Figure 3.1B displays the reversible magnetization of type-II SCs [Bra03] with different values of κ , where ξ is constant. The magnitude of the magnetization decreases the larger the value of κ

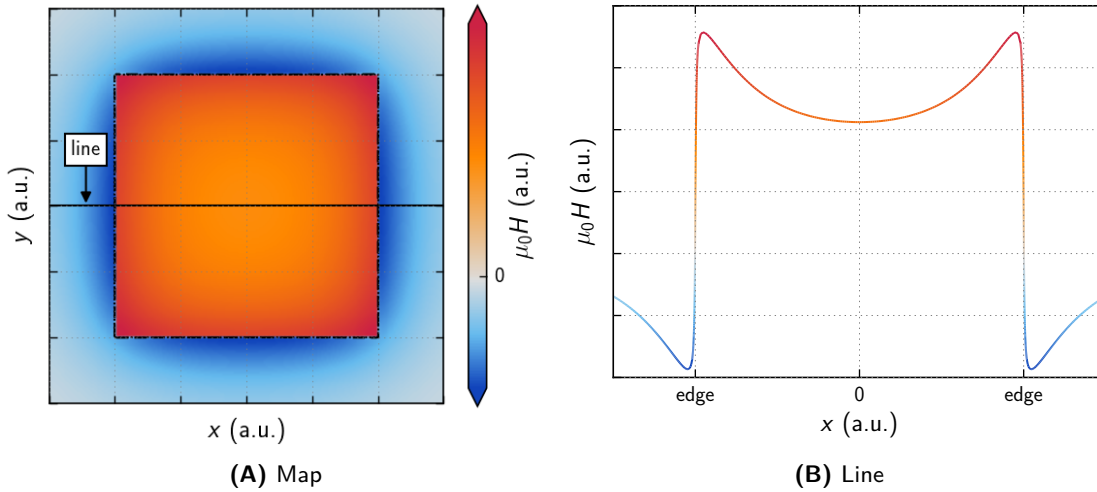


Figure 3.2: Two dimensional and one dimensional field profile above a square crystal, that originates from the reversible magnetization. The dashed line in A represent the position where the magnetic field is zero and the horizontal line indicates the position of the line plotted in B.

becomes. In case of an anisotropic crystal, this means that the value of M_{rev} , and therefore the shielding current, is smaller when the magnetic field is parallel to the ab -planes.

An example for a magnetic field profile is visualized in figure 3.2. At the sample edges the field profile exhibits a step in the field that is caused by the shielding current near the surface.

3.1.2 Irreversible Properties

The reversible magnetization is only observable in very clean SCs. If a current is applied to such a sample the FLs begin to move because of the Lorentz force. This movement of the FL dissipates energy, which corresponds to a finite resistance and the material can no longer be considered a perfect conductor [Car12].

From the viewpoint of applications, the maximum transport current density (i. e. J_c) is the most important quantity of a SC [Dew01]. In order to enable the loss-free transport of current the FL movement has to be detained by so-called pinning centers. These pinning sites are local distortions of the crystal lattice in the material, where the FLs conserve condensation energy. This leads to a force that acts against the FL movement. The maximum possible current which can be carried by a material before the FLs are unpinned is defined by the effectiveness and number of the pinning sites. The maximization of the pinning force is important to achieve a large J_c .

Non-superconducting inhomogeneities that act as pinning centers in the material are: crystallographic lattice dislocations, vacancies, interstitials, GBs, twin planes, precipitates, defects caused by irradiation, planar dislocation networks, or rough surfaces that causes spatial variation of the FL length and energy [Bra95].

A consequence of the FL pinning is that the magnetic response of the SC becomes history dependent, as discussed in the context of the critical state model in section 2.2. In general, an artificially induced increase of J_c leads to the deterioration of other critical values such as T_c . Therefore, a compromise is usually necessary to ensure the applicability of a SC.

The modeling of the irreversible properties of a samples has been discussed in the context of the measurement techniques in section 2.2. The irreversible magnetic moment of a cubic sample is calculated with equations (2.5), (2.7) and (2.9). An exemplary plot of a field profile originating from J_c is shown in figure 3.3. The dependence of this irreversible field profile on the geometry of the sample is more obvious than for the reversible field profile. The square geometry in figure 3.3

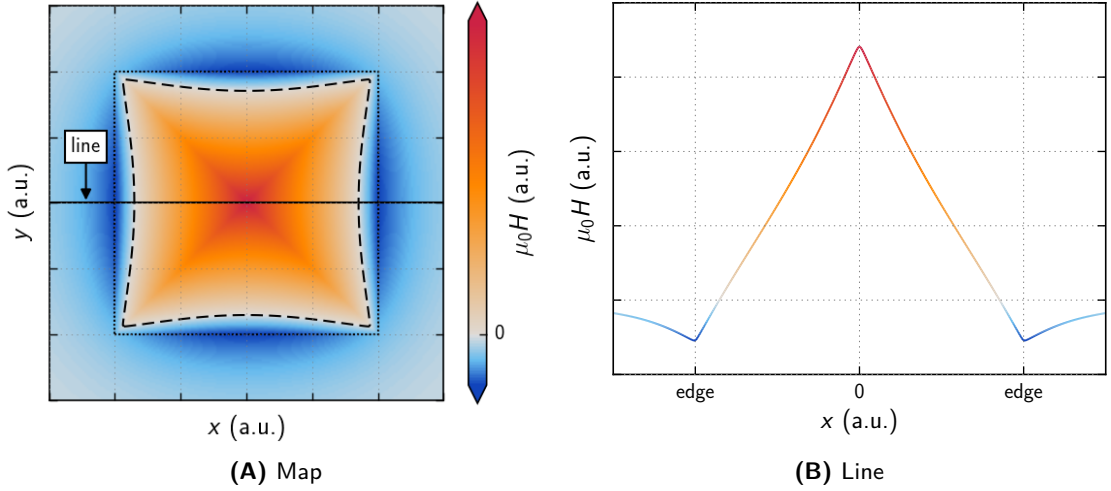


Figure 3.3: Two dimensional and one dimensional field profile corresponding to the irreversible current density of a crystal, similar to figure 3.2.

entails an X-shaped field distribution. In case of a rectangle this field distribution has the shape of a rooftop (cf. figure 3.4), because the magnetic field distribution is determined by the smallest sample dimension orthogonal to H_{ext} .

3.2 Polycrystals

In practical applications the materials of interest are polycrystalline, where GBs together with unwanted defects are unavoidable. Some defects which occur during their fabrication process are cracks or wetting phases which reduce the maximum critical transport current (I_c) in HTS, because of their weak-link behavior (see chapter 4). In LTSs the GBs usually act as effective, two-dimensional, pinning centers. The samples and the modeling introduced in this thesis only treat the weakly linked HTSs.

A consequence of weakly linked grains is the formation of two distinct length scales on which the currents flow in the sample [Gur11]. One is J_c which flows in the whole sample while J_{intra} is confined to the grains. Both current densities can be modeled similar to crystals as discussed above, but in contrast to crystals the development of the field profile is different in polycrystals because of the interaction between the two current densities.

In HTSs the FLs penetrate the sample preferably along the GBs [Pol96] when H_{ext} is increased, which leads to the emergence of a global field gradient inside the sample, similar to the irreversible field profile shown in figure 3.3. This global field profile of a polycrystal is referred to as inter-grain field profile. The grains are penetrated with FLs as soon as the local field around a grain is high enough, and they develop their own field profiles, which influence the further development of the inter-grain field profile, which in return influences the development of the local field profiles of the grains, and so forth.

This section discusses the influence of J_c , i. e. a global field gradient, on the combined magnetic response of the grains, which is denoted by the superscript „G“:

$$m^G = \sum_i m_i. \quad (3.3)$$

Here, m_i denotes the magnetic moment of grain i . The mean magnetization at H_{ext} relates to

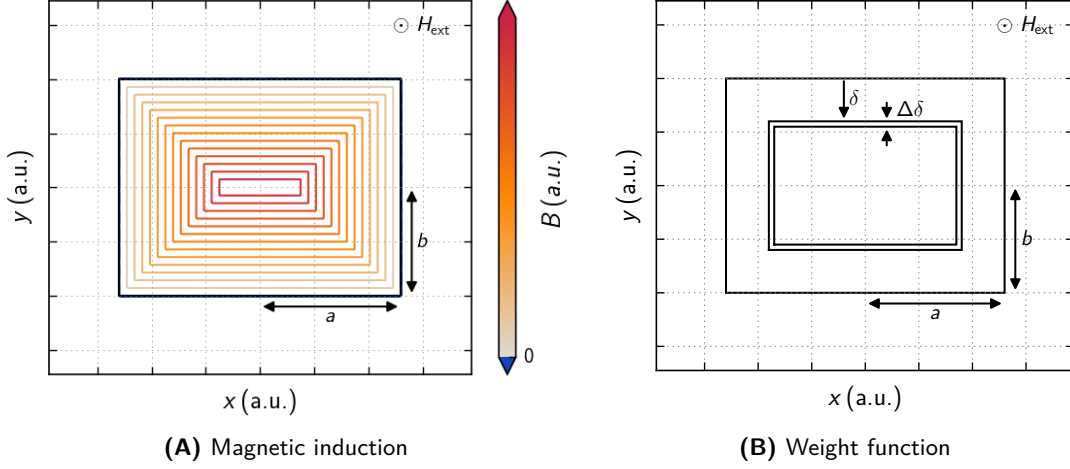


Figure 3.4: Magnetic induction (B) inside the sample and the graphical definition of the weighting function $g(\delta)$.

the magnetic moment via:

$$M^G(H_{\text{ext}}) = \frac{m^G(H_{\text{ext}})}{V}, \quad (3.4)$$

where V is the sample volume.

In the course of the following discussion, a polycrystalline sample is considered, where all grains are cubes with the same edge length. If no global field gradient is present, the value of $M^G(H_{\text{ext}})$ is assumed to coincide with $M(H_{\text{ext}})$ of a single grain, because every grain in the bulk is exposed to the same field (i. e. H_{ext}). With a field gradient, the grains at the sample border feel a different field than the grains closer to the sample center. Furthermore, the number of grains with the same magnetization is larger at the sample edges, because of the dependence of the field profile on the sample geometry. Figure 3.4A shows the contours of the distribution of the magnetic induction (B) inside a cubic sample ($2a \times 2b \times 2c$ with $b \leq a$) with a saturated inter-grain field profile. The rectangular shape of the sample is adopted by the field distribution. The value of B depends on the distance to the closest sample edge (δ). The number of grains which are exposed to the same value of B is proportional to the volume defined in figure 3.4B:

$$\Delta V = 8c[(a - \delta)(b - \delta) - (a - \delta - \Delta\delta)(b - \delta - \Delta\delta)], \quad (3.5)$$

where c is the sample dimension parallel to H_{ext} .

This can be exploited to rewrite equation (2.3) into an integral of the magnetization of a crystal and a weighting function $g(\delta)$:

$$m^G(H_{\text{ext}}) = \int M(H(\delta))g(\delta) d\delta, \quad \text{with} \quad g(\delta) = \lim_{\Delta\delta \rightarrow 0} \frac{\Delta V}{\Delta\delta}, \quad (3.6)$$

where $g(\delta)$ is $8c(a + b - 2\delta)$ in case of a cubic geometry, or $4\pi c(R - \delta)$ for a cylinder with radius R . The equation can be substituted if the local distribution of the magnetic induction, $B = \mu_0 H(\delta)$, is assumed to be described with the extended critical state model: $\delta = |H_{\text{ext}} - H|/J_c(H_{\text{ext}})$, where the function $J_c(H_{\text{ext}})$ describes a spatially invariant critical current density at H_{ext} . Thus δ can be substituted by a magnetic field and equation (3.6) becomes:

$$m^G(H_{\text{ext}}) = \frac{1}{J_c(H_{\text{ext}})} \int_{H_1}^{H_2} M(H)\tilde{g}(|H_{\text{ext}} - H|) dH, \quad (3.7)$$

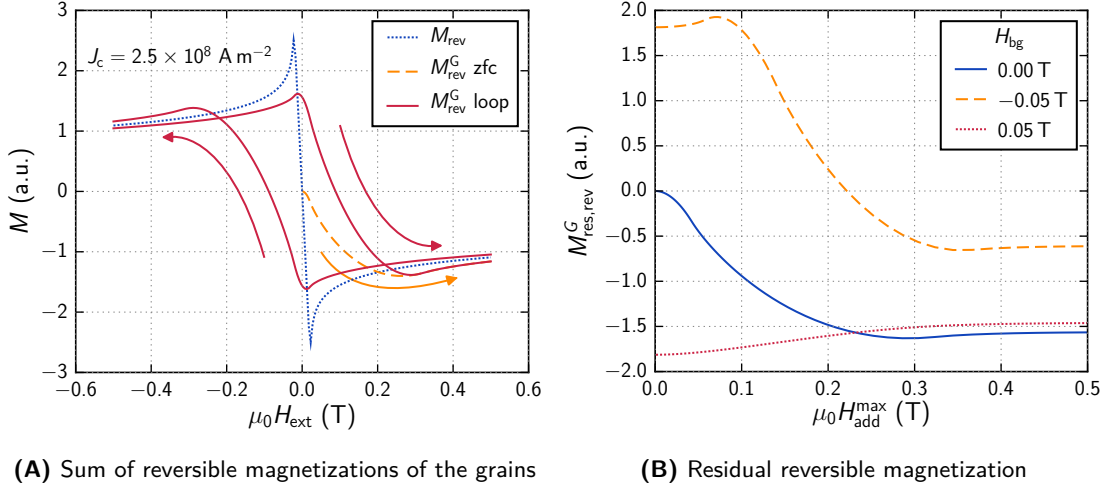


Figure 3.5: Numerically calculated global response of the magnetization originating from the representative reversible intra-grain current density ($M_{\text{rev}}^{\text{G}}$) in a polycrystalline sample with a constant inter-grain current density (J_c) and the change in the residual reversible magnetization of the grains ($M_{\text{res,rev}}^{\text{G}}$) at different background fields (H_{bg}).

where $\tilde{g}(H)$ is $8c(a + b - 2H/J_c(H_{\text{ext}}))$ in case of a cubic geometry, or $4\pi c(R - H/J_c(H_{\text{ext}}))$ for a cylinder with radius R . A dependence of $H(\delta)$ on the z -coordinate, which could be caused by demagnetization effects, is neglected. Equation (3.7) can be used to calculate the mean magnetic moment of the grains, if the field dependent magnetization ($M(H)$) and the dependence of the inter-grain current density on the external applied field ($J_c(H_{\text{ext}})$) is known.

3.2.1 Reversible Properties

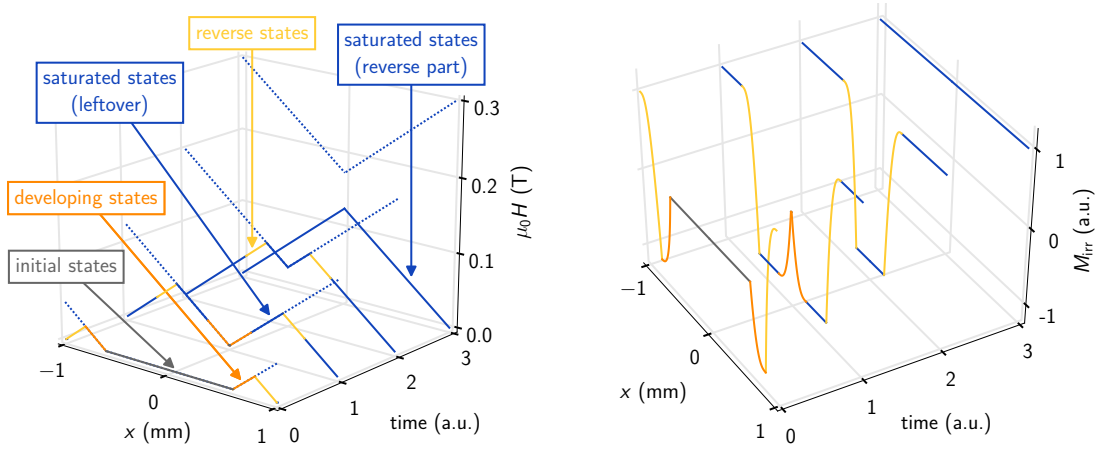
The simplest cases to calculate the reversible contributions to the total magnetization are the developing and saturated field profiles. In figure 3.5A, the magnetization from the developing field profile is labeled „ $M_{\text{rev}}^{\text{G}} \text{ zfc}$ “ and „ $M_{\text{rev}}^{\text{G}} \text{ loop}$ “ indicates the field dependence of the saturated field profile, while M_{rev} is the reversible magnetization determined by Brandt [Bra95]. In both developing and saturated field profiles one boundary field in the integral of equation (3.7) (H_2) coincides with H_{ext} , while the other boundary field is given by the field at the sample center:

$$H_1 = \begin{cases} 0 & \text{developing field profile} \\ H_{\text{ext}} \pm J_c(H_{\text{ext}})b & \text{saturated field profile} \end{cases} \quad (3.8)$$

The sign in the saturated state is positive if H_{ext} is decreasing and negative when H_{ext} is increasing. The impact of J_c on $M_{\text{rev}}^{\text{G}}$ is the emergence of a hysteresis, as shown in figure 3.5A. In other words, the equilibrium magnetization of the grains is no longer reversible.

This fact is also seen in the residual magnetization originating from all reversible contributions of the grains ($M_{\text{res,rev}}^{\text{G}}$) in figure 3.5B, where the development of the magnetic signal at three different H_{bg} is plotted in dependence of an increasing maximum additional applied field ($H_{\text{add}}^{\text{max}}$). The figure shows that the reversible contribution can be an important part of the total residual magnetization (M_{res}) of a polycrystal near zero field.

In this section the value of J_c is spatially invariant, which may not be true in actual measurements of weakly linked polycrystals, wherefore the field dependence of $M_{\text{res,rev}}^{\text{G}}$ can be slightly different from the one plotted in figure 3.5B, but the central statement that the reversible contributions of the grains is history dependent in polycrystalline HTS is still valid.



(A) Formation of the inter-grain field profile, where the states of the intra-grain field profiles are indicated. (B) Corresponding spatial dependence of the irreversible magnetization (M_{irr}) inside the grains.

Figure 3.6: Connection of the formation of the inter- and intra-grain field profiles in a polycrystalline cylinder.

3.2.2 Irreversible Properties

The irreversible contribution of the grains to the magnetic signal of a polycrystal is calculated similar to M_{rev}^G , but instead of inserting M_{rev} , the irreversible magnetization (M_{irr}) is used in equation (3.7), calculated with equation (2.7). Figure 3.6A shows the development of the residual inter-grain field profile for positive H_{add}^{max} . The text boxes in the figure indicate the state of the field profiles inside the grains. The critical state model is employed to model J_c and J_{intra} (J_c is field independent). The time axis in figure 3.6 visualizes the formation of the residual field profile for increasing H_{add}^{max} . These field profiles are split into an initial, developing, reversed, and saturated part according to the states of the field profiles inside the grains. The saturated parts are further divided into one piece that is related to the reversed part of the field profile, while the other is a leftover of the field profile originating from H_{add}^{max} . The corresponding spatial distribution of M_{irr} of the individual grains inside the sample is plotted in figure 3.6B.

Figure 3.7A shows the influence of J_c on $M_{res,irr}^G$ of a polycrystalline sample. The curve labeled single grain is equivalent to the response of a polycrystalline sample where J_c is zero, while the curve denoted as polycrystal is the sum of the individual contributions if J_c is finite. The latter curve is split into the separate contributions of the field profile states outlined in figure 3.6.

At $H_{add}^{max} < H^{*G}$, where H^{*G} is the penetration field of a grain, only the contribution of grains in the developing and reverse state are present in figure 3.7A. The grains with a developing field profile produce a negative signal which becomes stronger until the optimum between the volume fraction of grains (specified by $g(\delta)$) and the magnetization in the developing field profile is reached. The contribution of the developing field profiles vanishes when H_{add}^{max} becomes larger than the sum of the global penetration field (H^*), which is related to J_c . The signal of the reverse part shows a more elaborated behavior, because the local magnetization of the grains changes its sign within the regions indicated with reverse states in figure 3.6. At very small H_{add}^{max} this contribution is approximately zero. The subsequent maximum in the signal is subject to the same argument as in the aforementioned developing states, i.e. the signal increases until the optimum between the volume fraction and the magnetization value of the grains is reached. Compared to the developing states the contribution of the reverse state becomes zero at the additional field where $M_{res,irr}^G$ saturates: $H_{add}^{max} = 2(H^* + H^{*G})$. The leftover of the saturated field profile, that was formed by H_{add}^{max} , gives a negative signal. This signal occurs while $H^{*G} < H_{add}^{max} < 2(H^* + H^{*G})$. Grains with an inverted saturated field profile are found in the

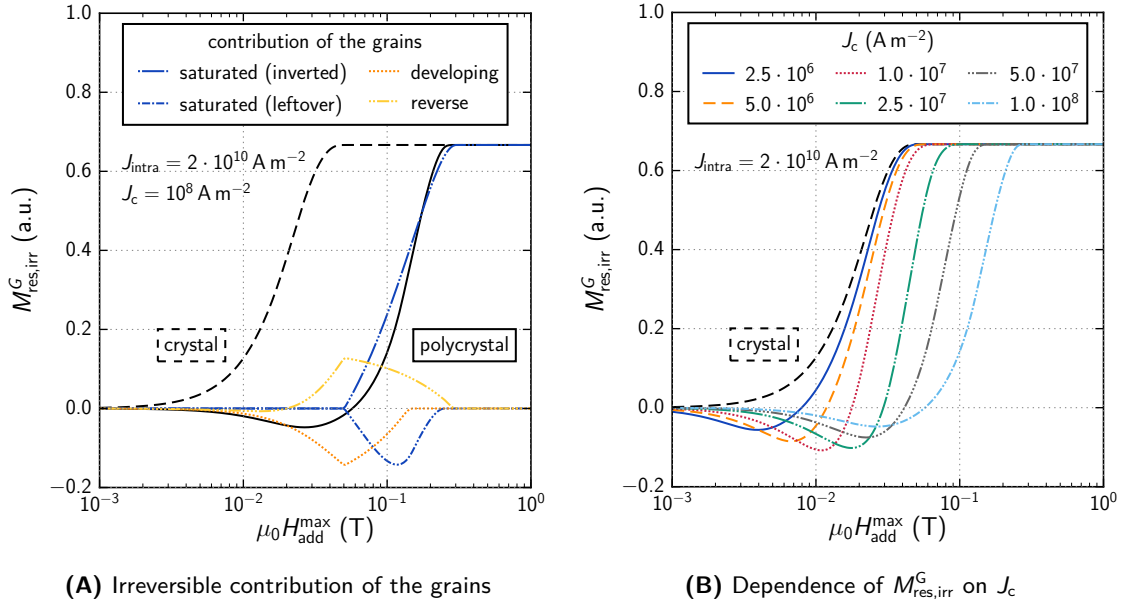


Figure 3.7: Residual magnetic signal of the irreversible contributions of figure 3.6 and a comparison of the global response of the residual magnetization originating from all irreversible contributions of the grains ($M^G_{res,irr}$) in a polycrystalline sample in dependence of inter-grain current density (J_c).

same field range and this contribution is the one that defines the magnitude of the final $M^G_{res,irr}$ ($H_{add}^{max} \geq 2(H^* + H^{*G})$).

The dependence of $M^G_{res,irr}(H_{add}^{max})$ on J_c is illustrated in figure 3.7A (J_{intra} is invariant). In case of a single grain the residual signal is positive, but a minimum occurs in $M^G_{res,irr}$ for finite values of J_c . This minimum is most pronounced at $J_c \approx 10^7 \text{ A m}^{-2}$ for $J_{intra} = 2 \cdot 10^{10} \text{ A m}^{-2}$. If J_{intra} is varied instead of J_c , the field, where the minimum occurs, is shifted to higher H_{add}^{max} the larger J_{intra} becomes, which is a result of the increased value of H^{*G} .

References

- [Abr04] A. A. Abrikosov (2004): „Nobel Lecture: Type-II superconductors and the vortex lattice“ *Rev. Mod. Phys.* **76**, 975.
- [Bae02] B. J. Baelus and F. M. Peeters (2002): „Dependence of the vortex configuration on the geometry of mesoscopic flat samples“ *Phys. Rev. B* **65**, 104515.
- [Bra95] E. H. Brandt (1995): „The flux-line lattice in superconductors“ *Rev. Mod. Phys.* **58**, 1465.
- [Bra03] E. H. Brandt (2003): „Properties of the ideal Ginzburg-Landau vortex lattice“ *Phys. Rev. B* **68**, 054506.
- [Car12] D. A. Cardwell and D. C. Larbalestier (2012): *Handbook of Superconducting Materials, 2nd Edition*. ISBN: 9781439817308.
- [Cle98] J. R. Clem (1998): „Anisotropy and two-dimensional behaviour in the high-temperature superconductors“ *Supercond. Sci. Technol.* **11**, 909.
- [Dew01] D. Dew-Hughes (2001): „The critical current of superconductors: an historical review“ *Low Temp. Phys.* **27**, 713.

- [Gin04] V. L. Ginzburg (2004): „Nobel Lecture: On superconductivity and superfluidity (what I have and have not managed to do) as well as on the ‚physical minimum‘ at the beginning of the XXI century“ *Rev. Mod. Phys.* **76**, 981.
- [Gur11] A. Gurevich (2011): „To use or not to use cool superconductors?“ *Nat. Mater.* **10**, 255.
- [Lon35] F. London and H. London (1935): „The Electromagnetic Equations of the Supraconductor“ *Proc. R. Soc. A* **149**, 71.
- [Mei33] W. Meißner and R. Ochsenfeld (1933): „Ein neuer Effekt bei Eintritt der Supraleitfähigkeit“ *Naturwissenschaften* **21**, 787.
- [Pol96] A. A. Polyanskii, A. Gurevich, A. E. Pashitski, N. F. Heinig, R. D. Redwing, J. E. Nordman, and D. C. Larbalestier (1996): „Magneto-optical study of flux penetration and critical current densities in [001] tilt $\text{YBa}_2\text{Cu}_3\text{O}_{7-\delta}$ thin-film bicrystals“ *Phys. Rev. B* **53**, 8687.

Chapter 4

Modeling Inter-Grain Currents

A student asked, „The questions on this year’s exam are the same as last year’s!“

I responded, „Yes; But this year the answers are different.“

— Albert Einstein, *Anecdote*

In polycrystals the grains form a three dimensional system, where each grain is described by its individual set of parameters, i. e. transition temperature, dimension, orientation, etc. Various effects are known to influence the inter-grain current density (J_c). To model J_c , the dominant mechanism has to be identified.

In iron based superconductors (iron based SCs), as well as other high-temperature superconductors (HTSs), large angle grain boundaries (GBs) were found to be unfavorable for large transport current densities [Kat11]. Since a transport current must pass through many GBs, i. e. weak-links, they pose one of the main problems in the HTS wire development. To advance the superconducting wire fabrication, the optimization of the properties of a GB is crucial. For this purpose the undesirable effects of weak-links on the global current transport have to be addressed.

The model, which will be presented in this section, is based on the superconducting tunneling effect first discussed by Josephson [Jos62]. He considered two superconductors (SCs) which are weakly coupled. The model describes the GBs in HTSs as a weakly coupled network of this so-called Josephson junctions (JJs).

4.1 Josephson Junction

The Josephson effect is a phenomenon which is closely related to the quantum mechanical tunnel effect. This effect enables particles, that can be described with quantum mechanics, to tunnel through a potential barrier. If the particles are treated in the framework of classical mechanics they could not overcome this barrier. In superconductivity, the potential barrier can be discussed as a structure that consists of a pair of SCs that are separated by a non-superconducting layer, which is in general referred to as a JJ, where the tunneling particles are the Cooper pairs.

JJs are employed in superconducting quantum interference device (SQUID) magnetometers. These measurement systems can detect very small magnetic fields, which is associated with the capability to measure magnetic flux quanta (ϕ_0). Various implementations of JJs exist, including point contacts, metal or semiconductor links. Most important for the present work is the fact that the GBs of HTSs become JJs when the misalignment angle between the crystallographic axes of the adjacent grains is large. A sketch of a JJ is shown in figure 4.1.

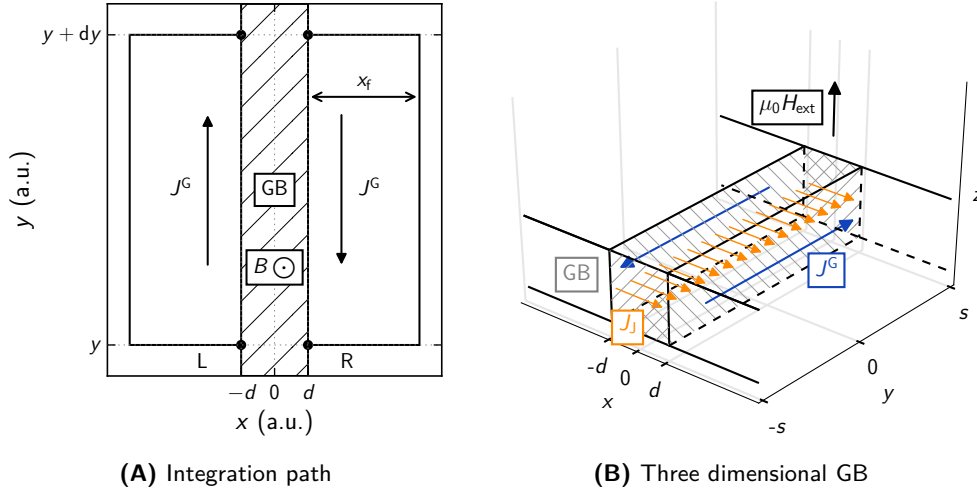


Figure 4.1: Visualization of the coordinate system used to model the Josephson current density across a grain boundary (GB).

4.1.1 Josephson Current Density

The Josephson current density (J_J) denotes the current density across the junction in dependence of the local magnetic induction (B). Figure 4.1A shows two SCs which are located on the left side and the right side of a barrier (i. e. a GB). Their attributes are distinguished by the characters „L“ and „R“. Since the electrons are condensed in their ground state they form Cooper pairs which are described by a quantum mechanical wave function denoted as the superconducting order parameter ψ . The wave function is defined by its expectation value $|\psi|^2$, which represents the Cooper pair density of a SC, and a phase φ :

$$\psi = |\psi|e^{-i\varphi}. \quad (4.1)$$

If the potential barrier between the left and the right SC is small enough, the wave functions overlap sufficiently to enable Cooper pairs to flow from one SC to the other. As a consequence, the phases of the two SCs are no longer independent from each other. Thus, the order parameters of the two SCs build a new, combined wave function: $|\psi\rangle = \psi_L |L\rangle + \psi_R |R\rangle$, where $|L\rangle$ and $|R\rangle$ denote the electron states in the left and right SC. This effect is referred to as weak coupling. [Bar82]

Following Barone and Paternò [Bar82], a quantum mechanical system is described by:

$$i\hbar \frac{\partial |\psi\rangle}{\partial t} = \mathcal{H} |\psi\rangle, \quad (4.2)$$

where the Hamiltonian, \mathcal{H} , is composed of two parts, \mathcal{H}_L and \mathcal{H}_R , which describe the unperturbed electron states of the respective SC, i. e. $\mathcal{H}_X = E_X |X\rangle \langle X|$ (E_X defines the energy of the ground state, and X is a placeholder for L or R). Additionally, the system has an interaction term which characterizes the tunneling between the states from one side of the JJ to the other:

$$\mathcal{H}_T = K (|L\rangle \langle L| + |R\rangle \langle R|). \quad (4.3)$$

The parameter K gives the measure of the interaction between the electron states. By applying

the projections $\langle L|$ and $\langle R|$ the two correlated mathematical expressions:

$$i\hbar \frac{\partial \psi_L}{\partial t} = E_L \psi_L + K \psi_R, \quad (4.4)$$

$$i\hbar \frac{\partial \psi_R}{\partial t} = E_R \psi_R + K \psi_L, \quad (4.5)$$

are obtained. By substituting the order parameters by their respective Cooper pair density and phase, the equations can be separated into an imaginary part, that is not of interest for the model, and a real part:

$$\frac{\partial |\psi_L|}{\partial t} = \frac{2K}{\hbar} \sqrt{|\psi_L| |\psi_R|} \sin(\varphi_L + \varphi_R), \quad (4.6)$$

$$\frac{\partial |\psi_R|}{\partial t} = -\frac{2K}{\hbar} \sqrt{|\psi_L| |\psi_R|} \sin(\varphi_L + \varphi_R). \quad (4.7)$$

The reduction of the Cooper pair density in the left SC leads to a corresponding increase of Cooper pairs in the right SC: $\partial |\psi_L| / \partial t = -\partial |\psi_R| / \partial t$. This time dependent change of $|\psi|$ defines a current density, which is called the Josephson current density:

$$J_J = J_0 \sin(\varphi), \quad (4.8)$$

with $\varphi = \varphi_L + \varphi_R$ and $J_0 = 2K/\hbar \cdot \sqrt{|\psi_L| |\psi_R|}$ the value of the Josephson current density at zero field.

4.1.2 Ginzburg-Landau Phase

In an external applied field (H_{ext}), φ is described by the gauge invariant phase, where the variation of φ at the position \mathbf{r} correlates with the vector potential \mathbf{A} and the current density \mathbf{J} through the equation:

$$\frac{\phi_0}{2\pi} \nabla \varphi = \mu_0 \lambda^2 \mathbf{J} + \mathbf{A}, \quad (4.9)$$

where λ is the magnetic penetration depth. In order to calculate φ the equation is integrated over a closed path parallel to and across the junction (figure 4.1A). Using Stokes' theorem and $\mathbf{B} = \nabla \times \mathbf{A}$ the equation becomes:

$$\varphi - \varphi_0 = \frac{2\pi}{\phi_0} \left(\mu_0 \lambda^2 \oint \mathbf{J} \, d\mathbf{r} + \int \mathbf{B} \, d^2 \mathbf{f} \right), \quad (4.10)$$

where $d^2 \mathbf{f}$ denotes the area enclosed by the path integral. This equation is a general expression for arbitrary \mathbf{J} and \mathbf{B} distributions. The JJ simplifies the equation because \mathbf{J} can be approximated by a current density that flows parallel to the junction, as shown in figure 4.1, and \mathbf{B} is approximately constant in the barrier.

Equation (4.10) would have to be solved for every GB in the sample, where every GB is described by a separate set of parameters. This is circumvented by assuming a representative JJ for the whole sample, i. e. that it describes J_c correctly. Thus, the parameters in the equation become average values that describe the polycrystal best. From now on, the intra-grain current density (J_{intra}) is replaced by a representative intra-grain current density (J^G), where the superscript „G“ is introduced to indicate an average value.

One strategy to calculate the phase in equation (4.10) is to introduce the value x_f , which defines the distance between the edge of the junction and the position where $J^G = 0$ in the SC. If no flux lines (FLs) are present inside the SCs, x_f is often approximated by λ . Bulaevskii et al. [Bul92] showed how a FL distribution can be take into account with x_f .

A second, but equivalent description of the problem, is to set the integration path at the edge of the junction, so that $x_f = 0$. In this case J^G at the junction has to be taken into account.

The variation of the phase difference $d\varphi/dy$ along the junction is now calculated for a JJs, which has the dimensions as defined in figure 4.1B, i. e. $-d \leq x \leq d$, $-s \leq y \leq s$ and $-h \leq z \leq h$ with d , s and h the thickness, the length and the height of the junction divided by 2. The parameters s and h are given by the geometry of the junction, while the value of d is much more difficult to define in HTS. At the same time d is one of the main parameter describing the phase variation. It defines an effective length within which the nonlinear effects are localized [Lik79], i. e. variations in the order parameter that are caused by the GBs. These nonlinear processes depend strongly on the type of the weak-link [Lik79]. When two superconductors are separated by a non-superconducting layer of a certain thickness, d is defined in good approximation by the thickness of the layer. In case of the GBs in HTSs, d describes the region in which the superconducting properties change, e. g. composition variations of the elements and lattice defects. Since these changes are usually continuous a sharp differentiation of a GB region and a SC region is not possible for polycrystals.

The coordinate system in figure 4.1 is defined so that the direction of H_{ext} is parallel to the z -axis, and J^G flows in y -direction parallel to the junction. Another approximation is that B is spatially invariant inside the GBs. With these assumptions the integral becomes:

$$\varphi - \varphi_0 = \frac{2\pi}{\phi_0} \left(\mu_0 \int (\lambda_L^2 J_L - \lambda_R^2 J_R) dy + \int 2Bd dy \right), \quad (4.11)$$

which can be differentiated by y to receive an equation describing the variation of the phase:

$$\frac{d\varphi}{dy} = \frac{2\pi}{\phi_0} (\mu_0 (\lambda_L^2 J_L - \lambda_R^2 J_R) + 2Bd). \quad (4.12)$$

The variables J_L and J_R denote the screening current densities on the left and right side of the junction and λ_L and λ_R allow to treat different magnetic penetration depth of the respective SCs. Since the model only treats one representative JJ for the whole polycrystal the current densities and the penetration depths are equal on both sides ($|J_R| = |J_L| = |J^G|$ and $\lambda_L = \lambda_R$). Therefore, the phase variation along the junction is:

$$\frac{d\varphi}{dy} = \frac{4\pi}{\phi_0} (\mu_0 \lambda^2 J^G + Bd), \quad (4.13)$$

which is defined as: $k \equiv d\varphi/dy$.

Different values of λ may arise due to an anisotropy between the crystallographic c -axis and the ab -planes of ceramic HTSs. Mints and Kogan [Min99] discussed the behavior of a JJ with arbitrary misaligned anisotropic SCs in detail. The λ in equation (4.13) should be interpreted as an average value of the anisotropy of the material:

$$\lambda = (\lambda_{ab}^2 \lambda_c)^{1/3}. \quad (4.14)$$

4.1.3 Model of Svistunov and D'yachenko

Svistunov and D'yachenko [Svi92] proposed that J^G is composed of a representative reversible intra-grain current density (J_{rev}^G), stemming from the reversible magnetization of the grains (M_{rev}^G), and of an representative irreversible intra-grain current density (J_{irr}^G), stemming from the irreversible magnetization of the grains M_{irr}^G :

$$J^G = J_{\text{rev}}^G + J_{\text{irr}}^G. \quad (4.15)$$

If $|B|/\mu_0$ at the GBs is smaller than the lower critical field (H_{c1}) and no FLs are inside the grains ($J_{\text{irr}}^G = 0$), the current density at the GB is a Meißner shielding current density: $J^G = B/(\mu_0 \lambda)$,

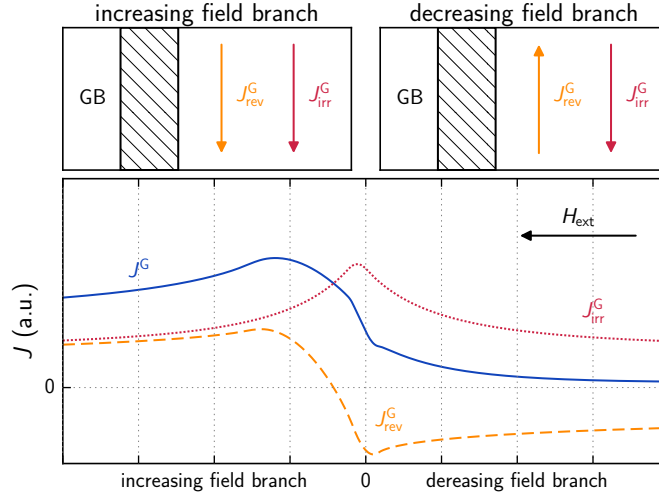


Figure 4.2: Superposition of the reversible ($J_{\text{rev}}^{\text{G}}$) and irreversible contributions ($J_{\text{irr}}^{\text{G}}$) to the intra-grain current density (J^{G}), where $J_{\text{rev}}^{\text{G}}$ was calculated with equation (3.7) and $J_{\text{irr}}^{\text{G}}$ with equation (2.9).

and thus $k \sim (\lambda + d)B$, which is the common representation for k used to discuss JJs [Bar82]. Equation (4.13) allows to extend the results of JJs to the mixed state, where FLs have penetrated the SC. Without pinning, the FLs inside the grain are distributed so that their total energy is minimized. This case defines $J_{\text{rev}}^{\text{G}}$. With pinning, the FL configuration inside the grain is modified compared to the ideal case, i.e. a field gradient develops that is described by $J_{\text{irr}}^{\text{G}}$. In contrast to the positive defined J_{J} (and J_{c}), all currents flowing inside a grain can have positive and negative values.

The idea of the model of Svistunov and D'yachenko is sketched in figure 4.2 based on equation (4.15). It shows the simplified behavior of the current densities inside the grains when H_{ext} is ramped from right to left in the figure. The sign of $J_{\text{irr}}^{\text{G}}$ remains unchanged because the pinning force preserves the field gradient inside the grains, while the sign of $J_{\text{rev}}^{\text{G}}$ is reversed when the field passes zero. The superposition of the two current densities is illustrated by the upper images for the respective field branches. They can be pictured as flowing in opposite directions on the decreasing field branch so that $|J^{\text{G}}|$ is smaller than on the increasing field branch where they flow in the same direction.

4.1.4 Maximum Josephson Current Density

The total current flowing across the junction is calculated by replacing the phase in equation (4.8) with the general solution of equation (4.13) and integrating equation (4.8) over the surface area of the junction [Bar82]:

$$I_{\text{J}} = \int_{-s}^s \int_{-h}^h J_0 \sin(ky + \varphi_0) dy dz, \quad (4.16)$$

where φ_0 is an arbitrary value. The zero field current density can be generalized with a spatial dependent term $J_0 \rightarrow J_0 \mathcal{D}(y, z)$, where $\mathcal{D}(y, z)$ is a two dimensional function. For simplicity this function is set 1, but more complicate current density distributions inside the junction can be calculated (see [Bar82]). For the trivial distribution the Josephson current is:

$$I_{\text{J}} = J_0 2h \int_{-s}^s \sin(ky + \varphi_0) dy = J_0 2h \frac{2}{k} \sin(ks) e^{i\varphi_0}, \quad (4.17)$$

where maximizing the current with respect to φ_0 yields:

$$\frac{I_{J,\max}}{4hs} = J_{J,\max} = J_0 \left| \frac{\sin(ks)}{ks} \right|, \quad (4.18)$$

where $J_{J,\max}$ is the maximum Josephson current density. With the substitution $ks = \pi\phi/\phi_0$ this equation is equivalent to

$$J_{J,\max} = J_0 \left| \frac{\sin(\pi\phi/\phi_0)}{\pi\phi/\phi_0} \right|, \quad (4.19)$$

which is a frequently used expression for the Fraunhofer pattern of JJs in the literature. A representative plot of this function can be found in figure 4.3 together with a graphical interpretation of the equation.

Figures 4.3B to 4.3F trace the behavior of the Fraunhofer pattern shown in figure 4.3A. When no magnetic flux is present the spacial dependent Josephson current density $J_J(y)$ (equation (4.16)) has an infinite sinus period, wherefore J_J is maximal in the whole junction. A finite magnetic field gives rise to a finite period that reduces $J_J(y)$ at certain areas. For instance, if the magnetic field corresponds to a flux $\phi = 0.5\phi_0$, $J_J(y)$ coincides with a half sinus period (figure 4.3C). By increasing the magnetic flux to ϕ_0 (figure 4.3D) $J_J(y)$ describes exactly one period. As a result an equal amount of current flows from one SC to the other so that $J_{J,\max}$ across the junction is zero. The same is true for any other multiple of ϕ_0 (figure 4.3F). A further increase of the magnetic flux entails a continuing development of this oscillating current density pattern. In case of $\phi = 1.5\phi_0$ (figure 4.3E) the current density inside the junction has one period of a sinus, which compensate the current flow for this area. The remaining half period gives the magnitude of the net current through the junction. This is the reason why the maximum Josephson current density is reduced when a magnetic field is applied. The higher the field is the more oscillations emerge of which each period cancels and reduces the net current density across the junction by a certain amount.

4.1.5 Fluctuations in the Josephson Junction

For the calculation of $J_{J,\max}$ the distribution function $\mathcal{D}(y, z)$ is set to unity. To investigate the impact of spatial fluctuations on $J_{J,\max}$ in dependence of H_{ext} , this distribution function has to be modified. Fluctuations can originate from local temperature variation and structural inhomogeneities which are always to some extent present in JJs [Yan70]. In a short JJ with random variations, $J_0(r) = J_0 + \delta J_0(r)$, the $J_{J,\max}$ does not vanish with increasing H_{ext} , but instead reaches a constant value J_{\min} [Vin90]:

$$J_{J,\max} = \sqrt{(J_0^2 - J_{\min}^2) \left(\frac{\sin(ks)}{ks} \right)^2 + J_{\min}^2} \quad (4.20)$$

where $J_{\min}^2 = r_0^2 \langle \delta J_0^2 \rangle / (4hs)$ with r_0 the a typical size of a fluctuation. Fistul' [Fis89] showed that spatial fluctuations in the junction give qualitatively the same results as disorder in the FL lattice near the GB, which can be caused by pinning.

Figure 4.4 shows the saturation of $J_{J,\max}$ at high fields schematically. The zero field current density is still J_0 . This means that the influence of the fluctuations are not very important at small H_{ext} , because the modification of the interference pattern is small in the interval ± 1 in the figure. Furthermore, equation (4.20) assumes that r_0 is much smaller than the size of the junction, i. e. $J_{\min}/J_0 \ll 1$. Assuming a junction with $s = 1 \mu\text{m}$ and $d = 1 \text{nm}$ and $J^G = 0$ the fluctuations will become important for $\mu_0 |H_{\text{ext}}| \gtrsim 1 \text{T}$. For $s = 0.1 \mu\text{m}$ the impact of fluctuations is negligible in the field range $\mu_0 |H_{\text{ext}}| \lesssim 10 \text{T}$.

Bulaevskii et al. [Bul92] treated a two-dimensional junction and found that $J_{J,\max}$ first drops when the field is increased, but then it reaches an approximately constant value at a characteristic

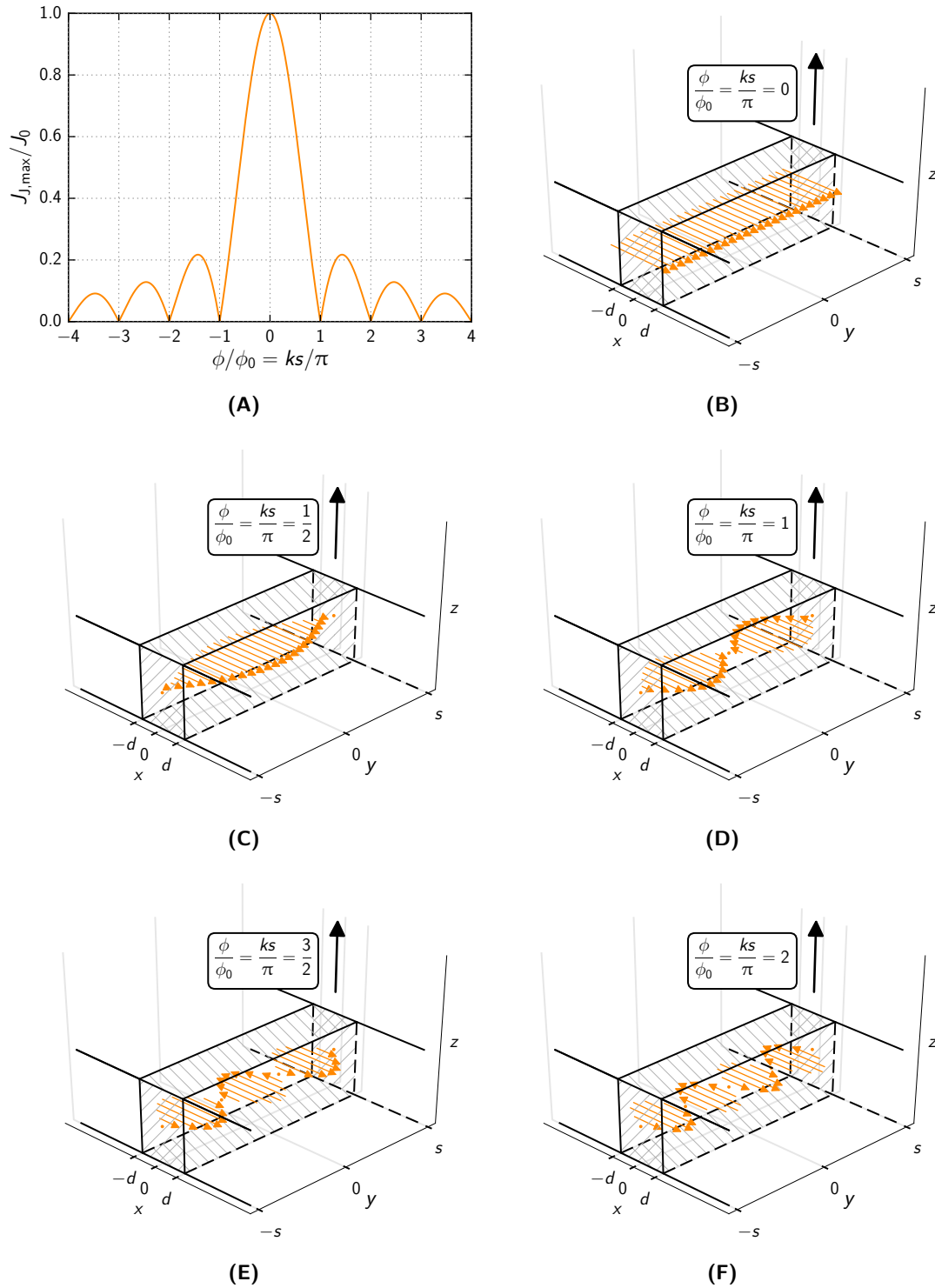


Figure 4.3: The interference pattern of the maximum Josephson current density ($J_{J,\max}$) resulting from a magnetic field. Panel A shows the result of equation (4.19). The other panels visualize the current flow inside the junction, where the text boxes refer to the applied magnetic flux (ϕ) and the arrows inside the junction denote the direction of the current flow as a function of y .

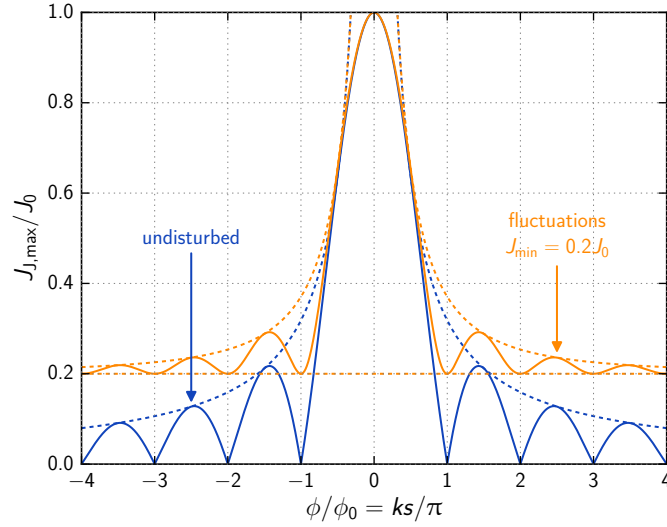


Figure 4.4: Modification of the undisturbed maximum Josephson current density ($J_{J,\max}$) by fluctuations of the properties in the junction.

field. At a second characteristic field, which is larger than the first, $J_{J,\max}$ begins to approach zero again.

As will be shown in chapter 6, the interesting effects occur near zero field. Thus the impact of fluctuations should be small.

4.2 Extension to Polycrystals

The inter-grain current density (J_c) has to cross many GBs when it flows in a macroscopic sample. Every GB in the sample is defined by the parameters in equation (4.12). In equations (4.13) and (4.21) these values are replaced with characteristic (mean) values, that describe the GBs in the polycrystal.

Another value that varies for the individual GBs is the length of a JJ (s). This fact can be accounted for by integrating equation (4.21) over the distribution densities introduced in section 2.1.1. The figures in that section show, how the distribution density of the grain size can be evaluated via images of the polished sample surfaces. Since the orientation of a grain is completely random in a polycrystal, the polishing process slices the grains randomly as indicated in figure 4.5A by the planes. Therefore, the characteristic grain size (s_0) should be interpreted as the mean value of the grain dimensions a , b and c . The grains are approximated by cubes with the edge length $2s_0$.

The statistical distribution of the junction width s , i.e. the grain radius, is visualized in figure 4.5B. The image shows that the value of s is not the same for every GB in a polycrystal. The distribution of s is described by the distribution density function $P(s, s_0, u)$ defined in equation (2.1). A large value of the distribution function parameter (u) implies that the width of the distribution is small, as shown in figure 4.5C. The definition of $P(s, s_0, u)$ is a modified version of a gamma type probability distribution. In contrast to the standard formulation the value of s_0 is independent from u .

The model assumes that equation (4.18) describes the current across every junction, i.e. the inter-grain current density that exits a grain on one side is independent from the value that enters a grain on the other side. Thus the global critical current density can be determined by summing over all junctions the current has to pass. For an infinite number of junctions this sum can be

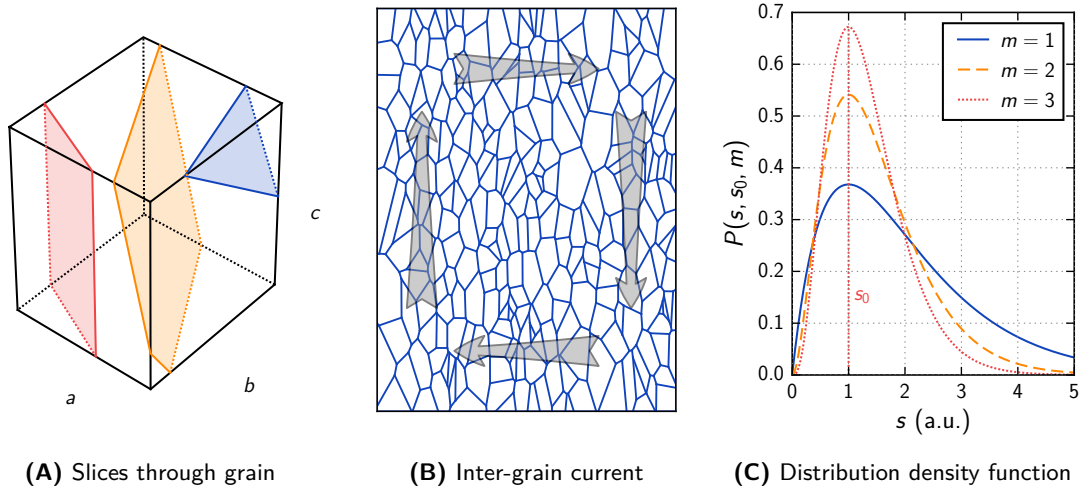


Figure 4.5: Modeling of the grain size distribution. Examples for the slices through a grain that may be detected at the sample surface and a sketch of the inter-grain current flow in a polycrystal. The distribution density function defined by equation (2.1) is used to fit the grain size distribution density.

written as an integral [Gon01]:

$$J_c(\alpha, u) \equiv \int_0^\infty J_{J, \max}(s) P(s, s_0, u) ds = J_{c0} \frac{\alpha_u^{u+1}}{\Gamma(u)} (-1)^{u-1} \frac{\partial^{u-1}}{\partial \alpha_u^{u-1}} \frac{\coth(\alpha_u/2)}{\pi^2 + \alpha_u^2} \quad (4.21)$$

with $\alpha_u = u\pi/|ks_0|$ and $u \in \mathbb{N}^+$. The redefinition of J_0 as J_{c0} is intended to indicate that the maximum Josephson current density is now a global current density. In equation (4.21) the interference pattern from equation (4.19) disappears. It is replaced by a continuous function, which can be applied to quantitatively evaluate the current densities in polycrystalline HTSs.

The angle between the grains defines the weak-link behavior of a junction. If the angle is small ($< 3-8^\circ$ depending on the material), the GB will not act as a weak-link and the two grains can be treated as one. Even more grains can be connected in this way and build a cluster of grains with low angle GBs. Since the J^G can flow unhindered in this cluster of grains, they can be treated as a single grain. This means that the term grain size relates to the size of these grain clusters.

The size of grain clusters may depend on the magnetic field. A large field may split one cluster into two or more parts, which modifies the value of s_0 . Such a variation of s_0 is not treated in this thesis.

4.3 Discussion of the Model

The influence of J^G on J_c is sketched in figure 4.6. It shows the simplified behavior of the current densities inside the grains when H_{ext} is ramped from the positive to the negative field axis (cf. figure 4.2). The presented model predicts, that the hysteresis of J_c is determined by the ratio between J_{rev}^G and J_{irr}^G . Equation (4.21) indicates that maximum inter-grain current density (J_{c0}) is reached when $k = 0$, which is defined by equation (4.13). A finite value of J^G shifts $J_c(\alpha, u)$ so that the peak occurs at the magnetic induction:

$$B_{\text{peak}} = \mu_0 \frac{\lambda^2 J^G}{d} = \mu_0 \frac{\lambda^2 (J_{\text{rev}}^G + J_{\text{irr}}^G)}{d}. \quad (4.22)$$

In figure 4.6, the curve labeled $J^G = 0$ shows the case where $J_{\text{rev}}^G = J_{\text{irr}}^G = 0$, and the peak is located at $B_{\text{peak}} = 0$.

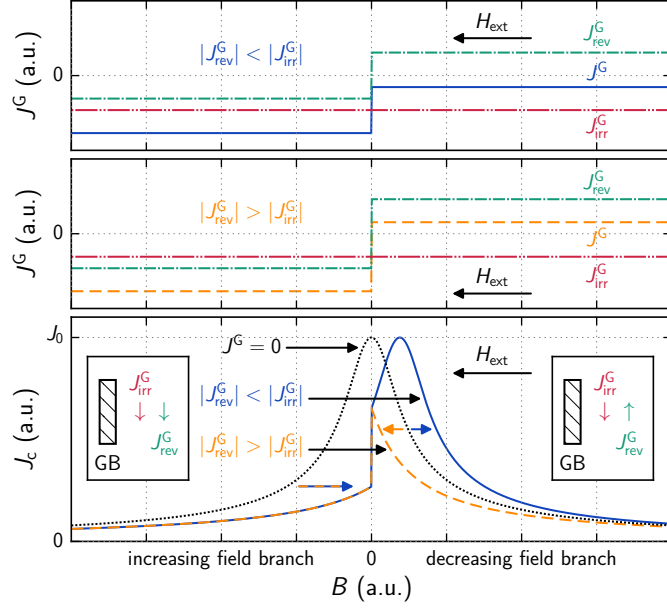


Figure 4.6: Simplified history dependence of the representative intra-grain current density (J^G) according to equation (4.15) for different ratios between the representative reversible intra-grain current density (J_{rev}^G) and the representative irreversible intra-grain current density (J_{irr}^G) ($|J_{\text{rev}}^G| < |J_{\text{irr}}^G|$ top panel and $|J_{\text{rev}}^G| > |J_{\text{irr}}^G|$ middle panel), and the impact on the inter-grain current density (J_c), as defined by equation (4.21) (bottom panel).

If $|J_{\text{rev}}^G| > |J_{\text{irr}}^G|$, $B_{\text{peak}} = 0$ and the maximum J_c is smaller than J_{c0} because $|k| > 0$ applies for both the increasing and decreasing field branch. The values of J_{rev}^G and J_{irr}^G are exchanged for the curve labeled $|J_{\text{rev}}^G| < |J_{\text{irr}}^G|$ in figure 4.6. In this case the maximum of J_c occurs on the decreasing field branch while the behavior on the increasing field branch is unchanged.

The dotted curve in figure 4.6 is shifted to the right on the increasing field branch for finite values of J_{rev}^G and J_{irr}^G . Therefore, J_c is always smaller than the curve labeled $J^G = 0$ on the increasing field branch. This behavior is different on the decreasing field branch, because J_{rev}^G and J_{irr}^G flow in opposite directions. The dotted curve is shifted to the left or to the right depending on whether J_{rev}^G is smaller or larger than J_{irr}^G .

Figure 4.7 is similar to figure 4.6, but J_{rev}^G and J_{irr}^G are varied systematically to illustrate the shift of the J_c curve in dependence of the ratio between J_{rev}^G and J_{irr}^G . The similarity between figures 4.7A and 4.7B is clearly visible. The figures allow to draw conclusions of the influence of the J^G shift in view of applications, where the increasing field branch is of interest because a magnet is always magnetized on the increasing field branch. The best properties on the increasing field branch are achieved when $J^G \rightarrow 0$, so that the shift of the J_c curve is minimal. Usually, the pinning should be as strong as possible and much effort is made to achieve a larger J^G in the grains. The presented model predicts the opposite, i.e. the pinning inside the grains and thus J^G should be as small as possible (but still large enough to support J_c).

Figure 4.8A shows that changes of λ in equation (4.21) do not alter the physics of the model qualitatively and lead to the same influence in the product $\lambda^2 J^G$ in equation (4.13) as those of J^G . On closer consideration, J^G is dependent on λ and the dependence of J_c becomes more sophisticated. For instance, in the Meißner state J^G is proportional to λ^{-1} , which leads to a linear λ dependence in equation (4.13). Figure 4.8A shows that the shift of the central peak results from the variation of λ , if the values of J_{rev}^G and J_{irr}^G are kept constant and λ is varied instead. A smaller λ leads to a larger J_c on the increasing field branch.

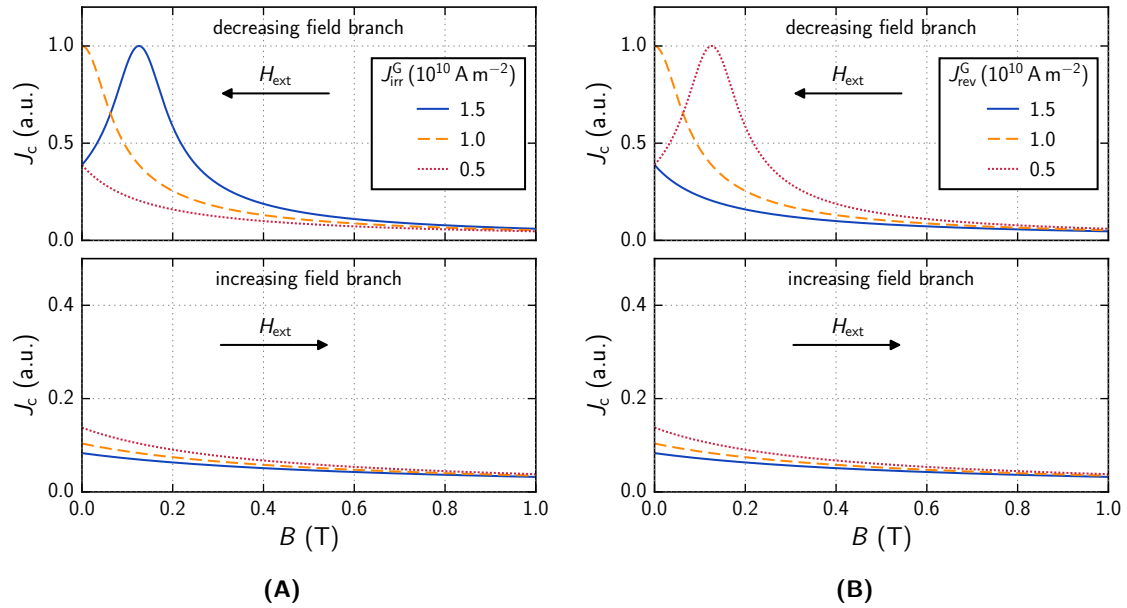


Figure 4.7: Dependence of the inter-grain current density (J_c) on the representative irreversible intra-grain current density (J_{irr}^G) and the representative reversible intra-grain current density (J_{rev}^G), as defined by equation (4.21). In A: $J_{rev}^G = 10^{10} \text{ A m}^{-2}$, and in B: $J_{irr}^G = 10^{10} \text{ A m}^{-2}$. The other parameters were $m = 1$, $d = 2 \text{ nm}$, $\lambda = 200 \text{ nm}$, and $s_0 = 1 \text{ }\mu\text{m}$.

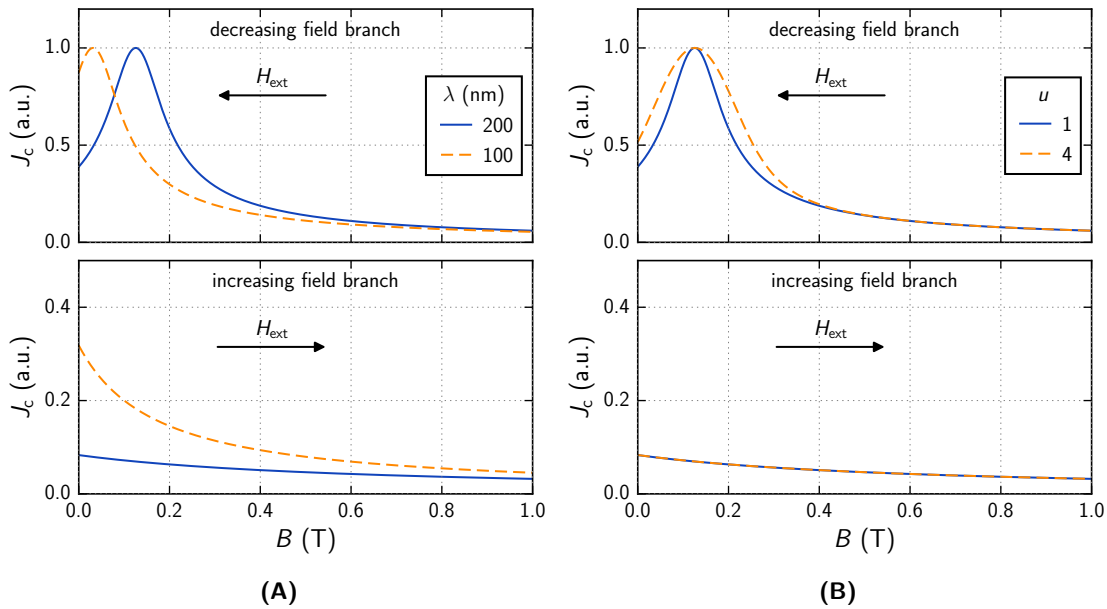


Figure 4.8: Dependence of the inter-grain current density (J_c) on the magnetic penetration depth (λ) and the distribution function parameter (u). If a respective parameter was invariant, it had the value: $m = 1$, $J_{irr}^G = 1.5 \cdot 10^{10} \text{ A m}^{-2}$, $J_{rev}^G = 10^{10} \text{ A m}^{-2}$, $d = 2 \text{ nm}$, $\lambda = 200 \text{ nm}$, and $s_0 = 1 \text{ }\mu\text{m}$.

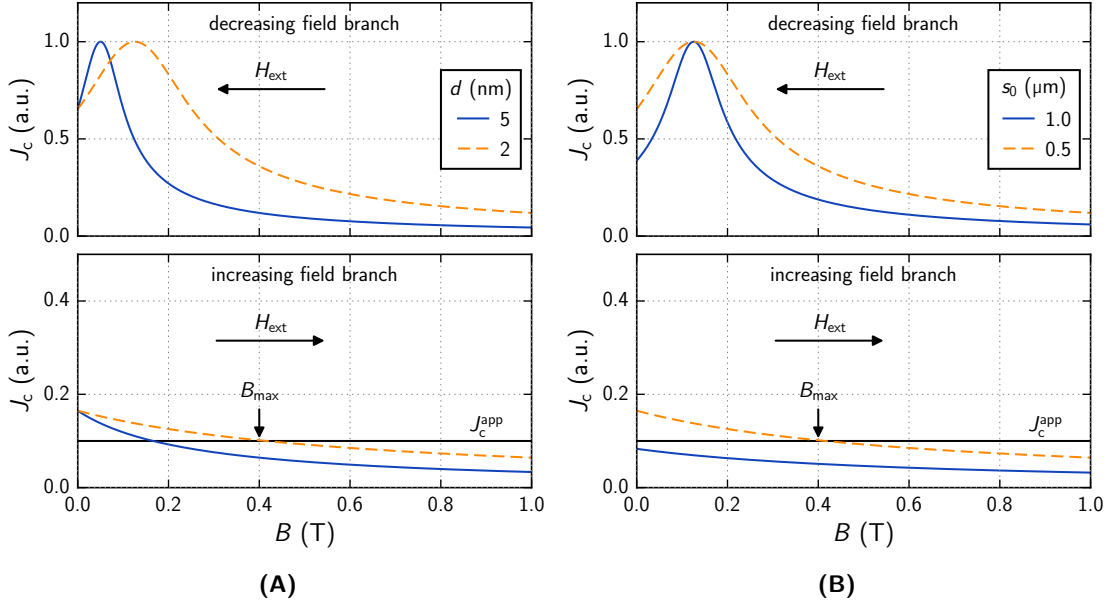


Figure 4.9: Impact of the characteristic thickness of the GBs (d) and the characteristic grain size (s_0) on the inter-grain current density (J_c). If a respective parameter was invariant, it had the value: $m = 1$, $J_{\text{irr}}^{\text{G}} = 1.5 \cdot 10^{10} \text{ A m}^{-2}$, $J_{\text{rev}}^{\text{G}} = 10^{10} \text{ A m}^{-2}$, $d = 2 \text{ nm}$, $\lambda = 200 \text{ nm}$ and $s_0 = 0.5 \mu\text{m}$.

The distribution of the grain size also influences the behavior of J_c . The parameter u is related to the width of the function, where larger values correspond to a sharper peak around s_0 (figure 4.5C). In equation (4.21) a large u entails a larger J_c in the vicinity of the peak (figure 4.8B).

Figures 4.7 and 4.8 show the field range where J_c^{G} , λ and m lead to noticeable changes of J_c , i.e. $|\mu_0 H_{\text{ext}}| \lesssim 1 \text{ T}$ for typical values of the involved parameters. This means that these parameters are less important at higher fields, $|\mu_0 H_{\text{ext}}| > 10 \text{ T}$ in which high field magnets are operated. The parameters J_c^{G} and λ only shift the J_c curve by a certain value because they do not depend on the field (in the presented model).

In contrast to J_c^{G} , λ and u a change in the parameters d and s_0 are independent of the field (within the framework of the model) and affect J_c at all fields. For instance, the smaller d is, the smaller the dependence of J_c on H_{ext} becomes, as visualized in figure 4.9A. This is consistent with the expected behavior of a GB, where a small value of d corresponds to stronger coupling between the grains, which increases J_c .

A change of s_0 has the same impact on J_c as the change of d , which is most interesting in view of the production of technical SCs. The dependence of a GB network with varying s_0 is visualized in figure 4.9B. A small s_0 in equation (4.21) entails a diminished field dependence of J_c . Within the framework of the presented model the most advantageous grain size of a weakly linked polycrystal is as small as possible. The model neglects the influence of the grain size on other superconducting properties, such as the superconducting transition temperature (T_c) or the upper critical field (H_{c2}). In reality the optimal/minimal grain size will be determined by the deterioration of the superconducting properties of the grains.

Neglecting this deterioration, a magnetic induction B_{max} can be extracted from figure 4.9 up to which a wire with a certain grain size can be used in typical applications. The value of B_{max} is defined by the point where J_c drops below a minimum value J_c^{app} , which is determined by the engineering critical current density of a wire and the envisioned application. This point can be approximated with equation (4.21). For typical values of λ ($\approx 200 \text{ nm}$), d ($\approx 2 \text{ nm}$) and J_c^{G} ($\approx 10^{10} \text{ A m}^{-2}$) the field dependence of k is mainly determined by the term $4\pi dB/\phi_0$ for

$B \gg 1$ T, which is true for high field applications. In the limit $\alpha < 1$ (with B sufficiently smaller than H_{c2}) equation (4.21) can be expanded into Taylor series at $\alpha = 0$, yielding the first order approximation:

$$B_{\max} \approx \frac{\phi_0}{2\pi^2} \frac{J_{c0}}{J_c^{\text{app}}} \frac{1}{s_0 d}. \quad (4.23)$$

The value J_c^{app} lies typically in the range 10^8 to 10^9 A m⁻², depending on the filling factor* of the wire and the envisioned application. Equation (4.23) can be used to estimate B_{\max} for the investigated iron based SCs in dependence of s_0 and d . The main message of the model is that the operable field range of an application can be increased by one order of magnitude by reducing the grain size or the GB thickness by one order of magnitude.

Another possibility to extend the operable field range of a device is to increase J_{c0} , which is defined by the properties of the GBs, i. e. the tunneling barrier. The barrier is defined by its „width,“ which is described by parameters such as d , and its „height,“ which is defined by parameters such as the coupling parameter of a JJ. A detailed analysis of the tunneling barrier and its impact on J_{c0} is out of the scope of this thesis.

4.4 Modification of the Critical State

The model of Svistunov and D'yachenko [Svi92] predicts that the intra-granular current flow leads to a hysteresis of J_c , which has consequences for the global field profile of a sample. According to the model, J^G has different values on the increasing and decreasing field branch, which causes a crossover in the inter-grain field profile when H_{ext} is ramped through zero.

For the discussion in this section J_c is split into two values, to emphasize the J_c hysteresis. One describes J_c on the increasing field branch ($J_{c,\text{inc}}$) and the other J_c on the decreasing field branch ($J_{c,\text{dec}}$), with $J_{c,\text{inc}} < J_{c,\text{dec}}$. Furthermore, two fields are defined. The first penetration field (H_1^*) defines the additional applied field (H_{add}) at which the flat field distribution from the initial field profile is entirely replaced by a field gradient for the first time, i. e. the field at which the developing field profile becomes saturated, similar to the penetration field (H^*). The second penetration field (H_2^*) corresponds to the field value at which the residual field profile saturates. The value of these fields changes depending on the background field (H_{bg}).

4.4.1 Field Profile

Together with the changes of H_1^* and H_2^* with H_{bg} , the field profile of the sample change, as shown in figure 4.10. In the figure the values of $J_{c,\text{inc}}$ and $J_{c,\text{dec}}$ are constant, but the conclusions that can be discerned from the figure also hold for field dependent values (in that case H_1^* and H_2^* depend on H_{ext} and H_{bg}). The sample is assumed to be an infinitely long cylinder with radius R in the following discussion, thus the geometry dependent factor n from equation (4.10) is one and is therefore not explicitly written.

The initial state is given by the horizontal line at the field value of H_{bg} in figure 4.10. The field profiles are plotted after applying an additional field H_{add} with a value of H_1^* and H_2^* . For the case that $-R(J_{c,\text{dec}} + J_{c,\text{inc}}) < H_{\text{bg}} < 0$ the field profile of the sample exhibits a distinct change in the slope at $H = 0$ when H_{ext} is ramped through zero (see figure 4.10B), because a part of the field profile is located on the increasing field branch, where J_c is smaller than on the decreasing field branch. H_1^* is smallest for $H_{\text{bg}} \geq 0$ (figure 4.10A) and it increases when H_{bg} becomes negative (figure 4.10B) until it reaches a maximum for $H_{\text{bg}} \leq -RJ_{c,\text{dec}}$ (figure 4.10C). In contrast, H_2^* is maximal if $H_{\text{bg}} \geq 0$ or $H_{\text{bg}} \leq -R(J_{c,\text{dec}} + J_{c,\text{inc}})$ (figures 4.10A and 4.10C). Between these two fields H_2^* is smaller (figure 4.10B), with a minimum at $H_{\text{bg}} = -RJ_{c,\text{inc}}$ which corresponds to the case where the field value at the sample center is zero for both the residual field profile and the field profile at H_2^* .

* The filling factor denotes the relation between superconducting and non-superconducting areas in the wire cross section.

4.4.2 Magnetization and Currents

The field profiles in figure 4.10 illustrate the influence of $J_{c,\text{inc}}$ and $J_{c,\text{dec}}$ on the critical state model. This influence is shown in figure 4.11A for the magnetization originating from J_c (M_{inter}) when H_{ext} is ramped to negative fields after cooling the sample in a certain H_{bg} . The magnetization is calculated for different values of H_{bg} , for the sample geometry with $a = b = 1$ mm and $J_{c,\text{inc}} = 1.5 \cdot 10^8$ while $J_{c,\text{dec}} = 3.5 \cdot 10^8$ A m⁻².

The impact of the two (constant) current densities $J_{c,\text{inc}}$ and $J_{c,\text{dec}}$ is obvious. The case $H_{\text{bg}} \leq 0$ is equivalent to the critical state model discussed in section 2.2 because only $J_{c,\text{inc}}$ defines the field distribution inside the sample. An alternation of the magnetic signal becomes evident when H_{bg} is slightly larger than zero so that $J_{c,\text{dec}}$ also contributes to the magnetic signal in the beginning. This leads to the emergence of a maximum in M_{inter} which increases with larger H_{bg} . At first, this maximum is located on the increasing field branch (e.g. $H_{\text{bg}} = RJ_{c,\text{inc}}/3$) and moves towards zero field for larger H_{bg} until it reaches zero (e.g. $H_{\text{bg}} = RJ_{c,\text{inc}}$). A further increase of H_{bg} leads to the saturation of the field profile on the decreasing field branch, i.e. M_{inter} follows the curve labeled $H_{\text{bg}} = \infty$.

The curve labeled $H_{\text{bg}} = \infty$ describes the dependence of the saturated field profile. Its value is constant on the decreasing field branch but drops rapidly when H_{ext} is ramped through zero. In order to calculate the impact of weakly linked grains more accurately, an iterative method can be utilized. A result of such an iteration is shown in figure 4.11B.

For this iteration, the grains were assumed to be cubic and their irreversible contribution of the grains was defined by the extended critical state model, where J_{intra} is given by equation (2.9) with $J_0 = 2.2 \cdot 10^{10}$ A m⁻², $\mu_0 H_0 = 1.5$ T, and $\beta = 1$. J_c was modeled using equation (4.21), where $J_{c0} = 4.5 \cdot 10^8$ A m⁻², $d = 2$ nm, and $\lambda = 200$ nm.

Without going into details, the iteration procedure is as follows. Before the iteration starts an arbitrary invariant J_c is chosen to describe $J_c(H_{\text{ext}})$. One step of the iteration is then conducted by:

1. calculating $M_{\text{irr}}^{\text{G}}(H_{\text{ext}})$ and $M_{\text{rev}}^{\text{G}}(H_{\text{ext}})$ from the field profile defined by $J_c(H_{\text{ext}})$ (cf. section 3.2), then
2. calculating $J_{\text{irr}}^{\text{G}} = M_{\text{irr}}^{\text{G}}/(s_0/3)$ and $J_{\text{rev}}^{\text{G}} = M_{\text{rev}}^{\text{G}}/\lambda$, and
3. inserting $J^{\text{G}} = J_{\text{irr}}^{\text{G}} + J_{\text{rev}}^{\text{G}}$ in equation (4.21) to calculate a new $J_c(H_{\text{ext}})$.

This iteration is carried out at various points on the field axis. $M_{\text{irr}}^{\text{G}}$ and $M_{\text{rev}}^{\text{G}}$ in each iteration are calculated as described in section 3.2.1. The resulting $J_c(H_{\text{ext}})$ is then used to repeat this procedure several times, until the variation from one iteration to the next becomes sufficiently small (e.g. $< 1\%$).

Figure 4.11 reproduces the characteristic drop of the magnetization at $H_{\text{ext}} = 0$, which is related to the weakly linked behavior of grains in HTSs. The common interpretation of this drop is that J_c is defined by equation (4.19) and therefore depends on the magnetic flux at the GBs. The basic equation to express this dependence in terms of the magnetic field is: $J_c \sim 1/|H|$. In a first approximation H is given by H_{ext} and a characteristic peak is expected in the magnetization that is symmetric about $H_{\text{ext}} = 0$. Therefore, the hysteresis of J_c cannot be explained within this simple picture. To account for the hysteresis the return field (H_{return}) of the grains is added to the equation: $H \rightarrow H_{\text{ext}} + H_{\text{return}}$. As a result, the magnetization and the corresponding J_c curves are shifted to the decreasing field branch. A hysteresis is now present when the values of the increasing and decreasing field branch are compared.

The presented model describes the J_c hysteresis in a different way, as already indicated in section 4.3. Instead of H_{return} , which is generated by J^{G} , J^{G} modifies J_c by shifting the phase of the order parameter. Since the shift due to J^{G} and the shift related to H_{return} occur simultaneously the dominant effect is often difficult to determine (with magnetization and transport current measurements). H_{return} is proportional to the grain size, so that it is more important if the grains

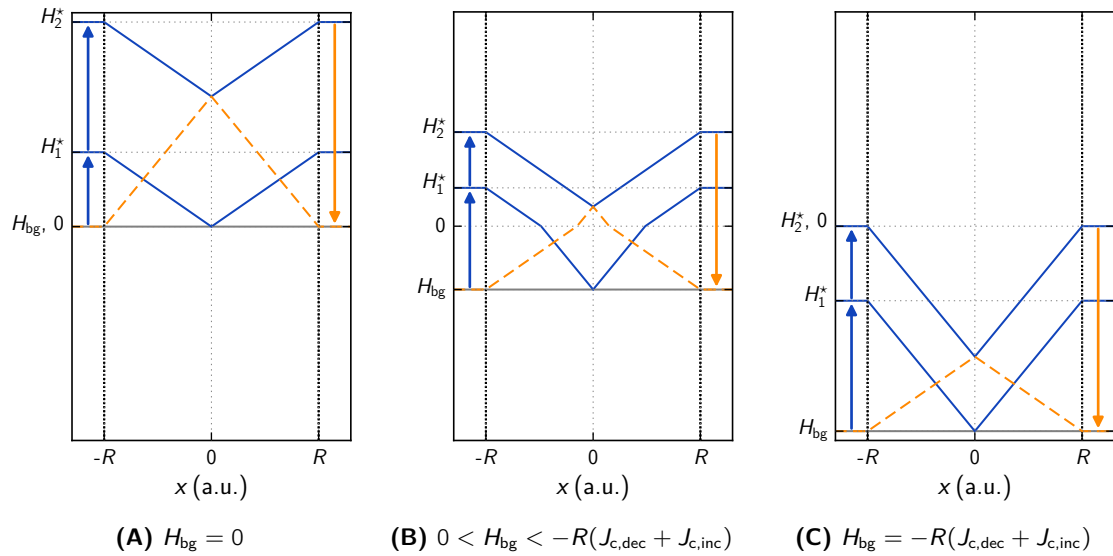


Figure 4.10: Graphical illustration of the modified inter-grain field profiles for constant values of $J_{c,inc}$ and $J_{c,dec}$ with $J_{c,inc} < J_{c,dec}$. The solid lines represent field profiles corresponding to additional applied fields and the dashed lines indicate the residual field profile.

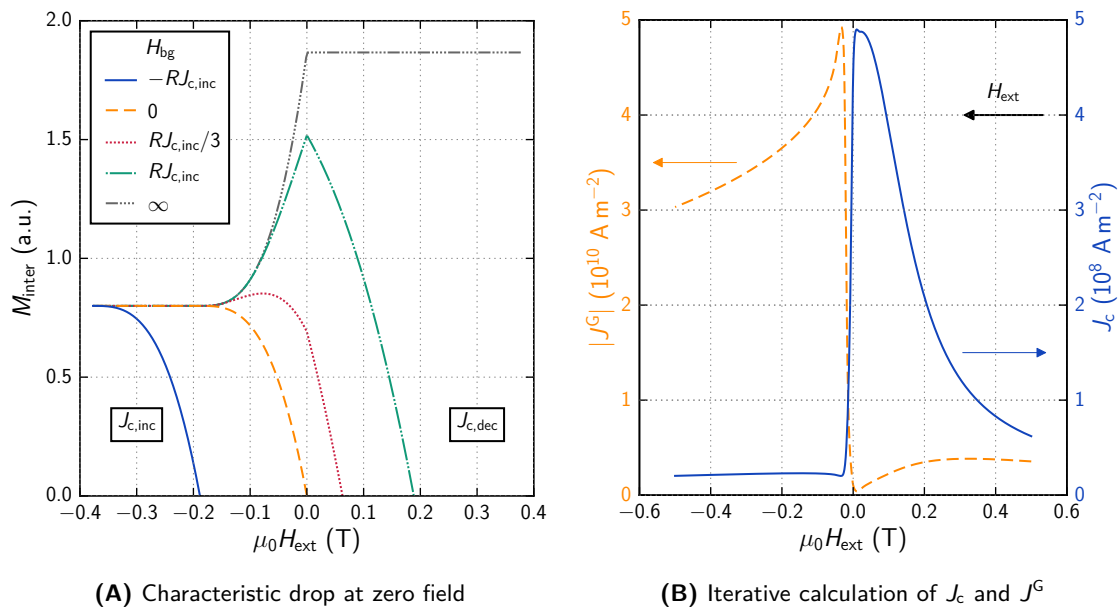


Figure 4.11: Magnetization curves of the inter-grain currents dependent on the background field (H_{bg}) and an iterative calculation of J_c and J^G for a field loop with a saturated field profile.

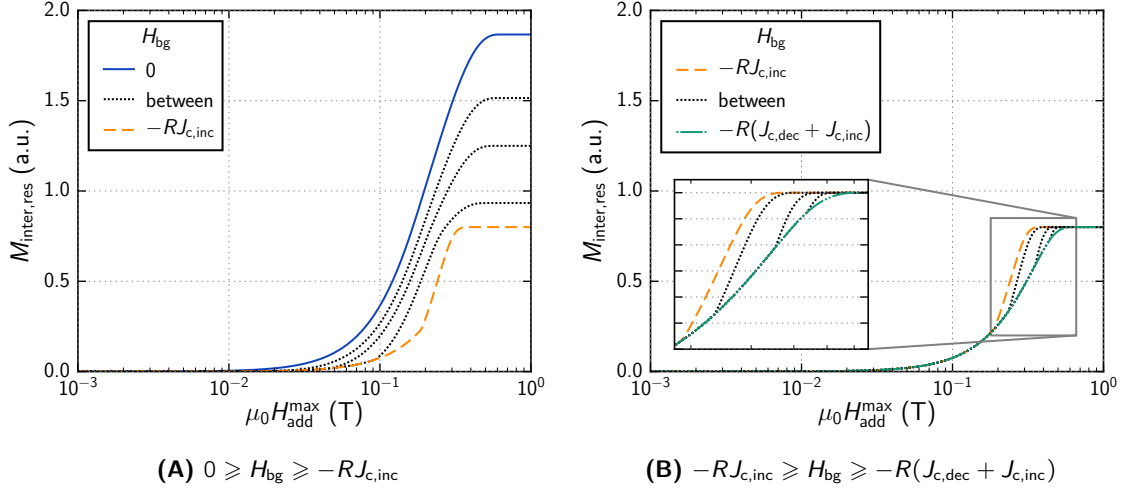


Figure 4.12: Residual magnetization originating from the inter-grain current ($M_{res,inter}$) in dependence of the background field (H_{bg}), where $a = b = 1$ mm with the inter-grain current density on the increasing field branch: $J_{c,inc} = 1.5 \cdot 10^8$, and on the decreasing field branch: $J_{c,dec} = 3.5 \cdot 10^8$ A m⁻².

are large. The investigated samples have comparatively small grains, thus the phase shift due to J^G is more important.

4.4.3 Residual Magnetization

The residual magnetization (M_{res}) is given by the sum of the residual magnetization originating from J_c ($M_{res,inter}$), the residual magnetization originating from all reversible contributions of the grains ($M_{res,rev}^G$) and the residual magnetization originating from all irreversible contributions of the grains ($M_{res,irr}^G$):

$$M_{res} = M_{res,inter} + M_{res,rev}^G + M_{res,irr}^G. \quad (4.24)$$

Figure 4.11 shows the characteristic drop of M_{inter} , that is found in weakly linked polycrystals when H_{ext} is ramped through zero. This drop influences $M_{res,inter}$, due to the different values of the current densities, as shown in figure 4.12, where the maximum additional applied field (H_{add}^{max}) is ramped to positive fields and $J_{c,inc}$ and $J_{c,dec}$ are constant. Two features are noticeable in figure 4.12A, that are directly related to the crossover from the decreasing to the increasing field branch. One is the steady decrease of the maximum $M_{res,inter}$ when H_{bg} becomes smaller until it reaches a minimum value at $H_{bg} = -RJ_{c,inc}$. The second feature is the decrease of H_2^* , which occurs simultaneous to the decrease of the maximum $M_{res,inter}$. H_2^* has a minimum at $H_{bg} = -RJ_{c,inc}$. At this background field the saturated residual field profile and the field profile at $H_{add}^{max} = H_2^*$ are both located on the increasing field branch, wherefore $H_2^* = 2RJ_{c,inc}$. For $H_{bg} < -RJ_{c,inc}$, H_2^* increases again until it reaches the same value as for $H_{bg} > 0$.

Besides the magnitude of $M_{res,inter}$ and H_2^* the curves in figure 4.12 exhibit different slopes depending on H_{bg} . A steeper slope is present when the field profile related to H_{add}^{max} changes from the decreasing into the increasing field branch, where the critical current density is smaller ($J_{c,inc} < J_{c,dec}$). Therefore, the magnetic flux penetrates the sample faster when H_{add}^{max} is on the increasing field branch and $M_{res,inter}$ increases more rapidly from this point on (cf. figures 4.10B and 4.10C).

The use of different values of $J_{c,inc}$ and $J_{c,dec}$ changes the curves in figure 4.12 insofar that the values of the saturated $M_{res,inter}$ and H_2^* are different, but the qualitative behavior is unchanged, i. e. the crossover from the decreasing to the increasing field branch is present.

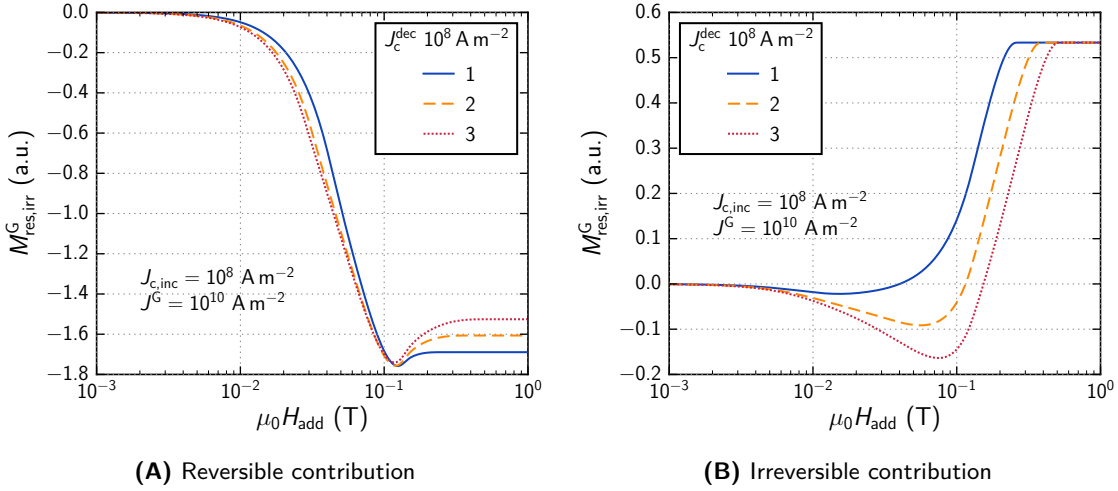


Figure 4.13: Residual magnetization of the reversible ($M_{res,rev}^G$) and irreversible contribution of the grains ($M_{res,irr}^G$) in dependence on the ratio between J_c on the increasing field branch ($J_{c,inc}$) and J_c on the decreasing field branch ($J_{c,dec}$), where the background field (H_{bg}) is zero. The sample dimensions are $a = b = 1$ mm and the dimensions of the grains are $a^G = b^G = 1$ μm .

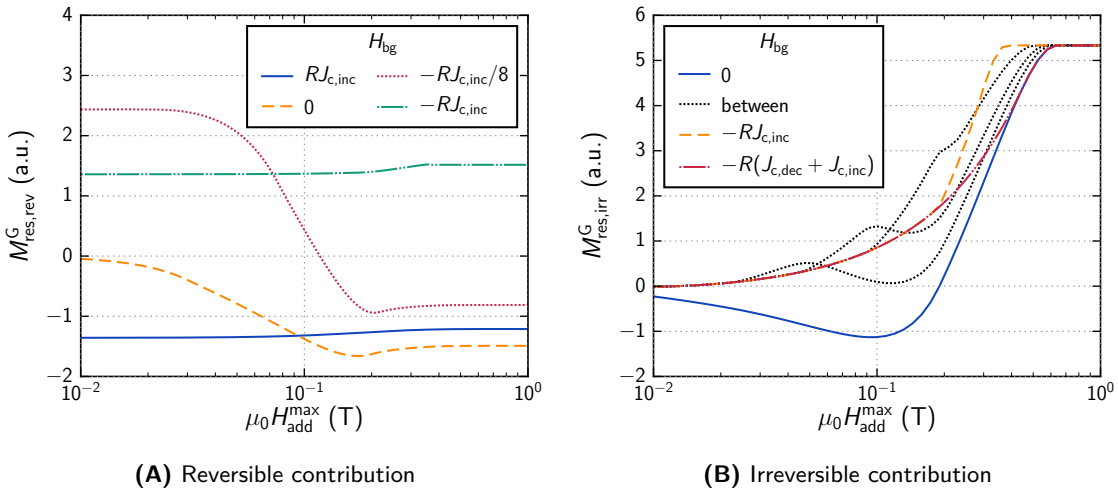


Figure 4.14: Same as figure 4.12, but here the reversible ($M_{res,rev}^G$) and irreversible intra-grain contributions ($M_{res,irr}^G$) are shown for different background field (H_{bg}), where the J_c on the increasing field branch ($J_{c,inc}$) and the J_c on the decreasing field branch ($J_{c,dec}$) as well as the sample and grain dimensions were the same as in figure 4.13.

Figure 4.13 shows the residual magnetization of the grains (M_{res}^G) for various $J_{c,dec}$ and a fixed $J_{c,inc}$, where $H_{bg} = 0$. The reversible ($M_{res,rev}^G$) and irreversible contributions ($M_{res,irr}^G$) of the grains are plotted separately. The reversible contribution is affected at all H_{add} by a variation of $J_{c,dec}$, while the irreversible part reveals a minimum in the magnetization that is more pronounced the larger the ratio $J_{c,dec}/J_{c,inc}$ is. The maximum value where all the grains are in the saturated state is always the same in figure 4.13B, in contrast to $M_{res,rev}^G$, where the saturation value is also affected. The reason for this is that $J_{c,inc}$ and $J_{c,dec}$ define the magnitude of $M_{res,rev}^G$, but in case of $M_{res,irr}^G$, J_{irr}^G is the determining quantity. Since J_{irr}^G is the same for every curve the saturation values are equal.

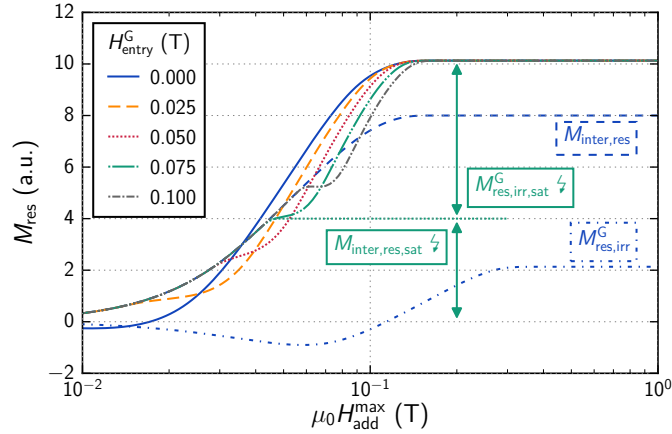


Figure 4.15: Residual magnetization (M_{res}) of the irreversible inter- ($M_{\text{res,inter}}$) and intra-grain contributions ($M_{\text{res,irr}}^G$) for different entry field into the grains (H_{entry}^G). The current densities were $J_{c,\text{inc}} = 10^8$, $J_{c,\text{dec}} = 3 \cdot 10^8$, and $J^G = 2 \cdot 10^{10} \text{ A m}^{-2}$, with the sample geometry: $a = b = 1 \text{ mm}$ and $c = 0.2 \text{ mm}$, and the geometry of the grains: $s_0 = 4 \text{ }\mu\text{m}$.

Only zero field cooling measurements were considered in the previous figures. Figure 4.14 shows the dependence of $M_{\text{res,rev}}^G$ and $M_{\text{res,irr}}^G$ for decreasing H_{bg} . The field dependence of $M_{\text{res,rev}}^G$ is large when a part of the residual inter-grain field profile crosses zero, because the reversible magnetization (M_{rev}) changes rapidly in this field range. This behavior is illustrated in figure 4.14A by the curves labeled $H_{\text{bg}} = 0$ and $-RJ_{c,\text{inc}}/8$. The variation of $M_{\text{res,rev}}^G$ is small for residual field profiles that do not cross zero ($H_{\text{bg}} = \pm RJ_{c,\text{inc}}$). The crossover from decreasing to the increasing field branch influences $M_{\text{res,irr}}^G$ if $-R(J_{c,\text{inc}} + J_{c,\text{dec}}) \leq H_{\text{bg}} \leq 0$ which is shown in figure 4.14B. For $H_{\text{bg}} \geq 0$ $M_{\text{res,irr}}^G$ is negative at first but becomes positive at a certain $H_{\text{add}}^{\text{max}}$ and finally saturates, while it is positive in case of $H_{\text{bg}} \leq -R(J_{c,\text{inc}} + J_{c,\text{dec}})$. The negative signal is a result of the inequality of $J_{c,\text{inc}}$ and $J_{c,\text{dec}}$ (cf. section 3.2.2). At $H_{\text{bg}} = -RJ_{c,\text{inc}}$ the residual field profile of the sample is located completely on the increasing field branch but the field profile at $H_{\text{add}}^{\text{max}}$ crosses the zero field axis before $M_{\text{res,irr}}^G$ saturates. The field at which $M_{\text{res,irr}}^G$ suddenly increases compared to the curve labeled $H_{\text{bg}} = -R(J_{c,\text{inc}} + J_{c,\text{dec}})$ coincides with $H_{\text{add}}^{\text{max}} + H_{\text{bg}} = 0$. The dotted curves in the figure show the behavior of $M_{\text{res,irr}}^G$ for $-RJ_{c,\text{inc}} < H_{\text{bg}} < 0$, where the curves exhibit a combined behavior of the others.

The combined results of figures 4.12 and 4.14B are shown in figure 4.15. An entry field (H_{entry}^G) is introduced, which has the purpose to simulate a delay of the penetration of the FLs into the grains. When the local field at the GBs becomes larger than this value the FLs can enter the grains (similar to H_{c1}). This field shifts M_{res}^G to higher $H_{\text{add}}^{\text{max}}$.

In figure 4.15, the contributions of the J_c and J^G currents cannot be distinguished. The systematic increase of H_{entry}^G leads to the emergence of a double step behavior in M_{res} , where the first increase is related to J_c . The step in M_{res} results from the negative contributions of the grains at small $H_{\text{add}}^{\text{max}}$, while the second slope at high $H_{\text{add}}^{\text{max}}$ is the combined signal of J_c and J^G .

As mentioned in section 2.2, the saturation values of $M_{\text{res,irr}}^G$ and $M_{\text{res,inter}}$ are used to estimate the magnitudes of the J_c and J^G [Eis10; Mul94]. If this „common“ interpretation is applied to the data in figure 4.15 of the $H_{\text{entry}}^G = 0.075 \text{ T}$, the saturation values of $M_{\text{res,irr}}^G$ and $M_{\text{res,inter}}$ ($M_{\text{res,irr,sat}}^G$ and $M_{\text{inter,res,sat}}$) would be erroneous, as indicated in the figure. The common interpretation leads to an underestimation of $M_{\text{inter,res,sat}}$ and the simultaneous overestimation of $M_{\text{res,irr,sat}}^G$, because the supposed first saturation is actually a result of the negative signal from $M_{\text{res,irr}}^G$ and not the saturation of the inter-grain field profile. Figure 4.15 also shows, that the supposed $M_{\text{res,irr,sat}}^G$ and $M_{\text{inter,res,sat}}$ depend on H_{entry}^G .

In this section the simplest case was considered where $J_{c,\text{inc}}$ and $J_{c,\text{dec}}$ are independent of the field and J^G is invariant, but the observations should apply to more realistic scenarios. The curves in figures 4.13A and 4.13B indicate that the signal of the grains modifies M_{res} in a way that has to be accounted for in a quantitative evaluation of M_{res} measurements. The figures point out the problem of the interpretation of the magnetization curves described in section 2.2, i. e. the separability of inter- and intra-grain signals.

References

- [Bar82] A. Barone and G. Paternò (1982): *Physics and applications of the Josephson effect*. ISBN: 9780471014690.
- [Bul92] L. N. Bulaevskii, J. R. Clem, L. I. Glazman, and A. P. Malozemoff (1992): „Model for the low-temperature transport of Bi-based high-temperature superconducting tapes“ *Phys. Rev. B* **45**, 2545.
- [Eis10] M. Eisterer, M. Zehetmayer, H. W. Weber, J. Jiang, J. D. Weiss, A. Yamamoto, E. E. Hellstrom, D. C. Larbalestier, N. D. Zhigadlo, and J. Karpinski (2010): „Disorder effects and current percolation in FeAs-based superconductors“ *Supercond. Sci. Technol.* **23**, 054006.
- [Fis89] M. V. Fistul’ (1989): „Mesoscopic behavior of Josephson junctions with randomly disposed Abrikosov vortices“ *J. Exp. Theor. Phys.* **96**, 209
[*Zh. Eksp. Teor. Fiz.* **96**, 369].
- [Gon01] J. L. Gonzalez, E. V. L. Mello, M. T. D. Orlando, E. S. Yugue, and E. Baggio-Saitovitch (2001): „Transport critical current in granular samples under high magnetic fields“ *Physica C* **364–365**, 347.
- [Jos62] B. D. Josephson (1962): „Possible new effects in superconductive tunnelling“ *Phys. Lett.* **1**, 251.
- [Kat11] T. Katase, Y. Ishimaru, A. Tsukamoto, H. Hiramatsu, T. Kamiya, K. Tanabe, and H. Hosono (2011): „Advantageous grain boundaries in iron pnictide superconductors“ *Nat. Commun.* **2**, 409.
- [Lik79] K. K. Likharev (1979): „Superconducting weak links“ *Rev. Mod. Phys.* **51**, 101.
- [Min99] R. G. Mints and V. G. Kogan (1999): „Josephson junction between anisotropic superconductors“ *Phys. Rev. B* **60**, 1394.
- [Mul94] K.-H. Müller, C. Andrikidis, H. K. Liu, and S. X. Dou (1994): „Intergranular and intragranular critical currents in silver-sheathed Pb-Bi-Sr-Ca-Cu-O tapes“ *Phys. Rev. B* **50**, 10218.
- [Svi92] V. M. Svistunov and A. I. D’yachenko (1992): „A layered structure as a Josephson medium“ *Supercond. Sci. Technol.* **5**, 98.
- [Vin90] V. M. Vinokur and A. E. Koshelev (1990): „Collective pinning of soliton lattice in Josephson junctions“ *J. Exp. Theor. Phys.* **70**, 547
[*Zh. Eksp. Teor. Fiz.* **97**, 976].
- [Yan70] I. K. Yanson (1970): „Effect of Fluctuations on the Dependence of the Josephson Current on the Magnetic Field“ *J. Exp. Theor. Phys.* **31**, 800
[*Zh. Eksp. Teor. Fiz.* **58**, 1497].

Chapter 5

Modeling Field Profiles

Apud me omnia fiunt Mathematicè in Natura.

Translation: *In my opinion, all things in nature occur mathematically.*

— René Descartes, *Correspondence with Mersenne*

In a bulk all existing current densities, i. e. inter-grain current density (J_c) and representative intra-grain current density (J^G), in the sample volume (V') contribute to the local magnetic field at a certain point. A Hall-probe measures the value of this magnetic field, where the magnitude of the contribution depends on the distance between the current loop and the active area of the Hall-probe. The magnetic field at a certain position (\mathbf{r}) is calculated with the Biot-Savart law:

$$\mathbf{H}(\mathbf{r}) = \frac{1}{4\pi} \int \frac{\mathbf{J}(\mathbf{r}') \times (\mathbf{r} - \mathbf{r}')}{|\mathbf{r} - \mathbf{r}'|^3} dV', \quad (5.1)$$

where $\mathbf{r}' = (x', y', z')$ defines a point in the sample at which the local current density $\mathbf{J}(\mathbf{r}')$ flows.

Some simplifications are necessary to derive an analytical function which can describe the current flow in a polycrystalline samples. The irreversible properties of J_c and J^G are approximated by the extended critical state model introduced in chapter 3.

5.1 Discretization

Since a superconducting sample may have a complicated geometry the volume is divided into sub-elements where the magnetic flux distribution $H(r)$ can be described by an analytical equation. One sub-element is defined by a trapezoid which is defined by 2×4 Cartesian (x, y, z) -coordinate points (see figure 5.1A). Four points define the trapezoid in the $z = 0$ plane while the other four define the trapezoid at the floor. These points are redefined as a set of variables $x_i, \{k_j, d_j\}, z_k$, where the indexes identify the integration boundaries in equation (5.1), i. e. the lower boundary has the index 1 and the upper boundary the index 2. The values of k_j and d_j define lines (l_j), which set the integration boundaries for y' at a certain value of x' , as shown in figure 5.1A.

In this trapezoid the current density is spatially invariant and flows along the positive x -axis: $\mathbf{J}(\mathbf{r}) = (J_c, 0, 0)$. By substituting $\hat{x} = x - x'$, $\hat{y} = y - y'$ and $\hat{z} = z - z'$ the Biot-Savart law becomes:

$$H_z = \frac{J_c}{4\pi} \int \frac{-\hat{y}}{(\hat{x}^2 + \hat{y}^2 + \hat{z}^2)^{3/2}} d\hat{x}d\hat{y}d\hat{z}, \quad (5.2)$$

where H_z is the vector component in z -direction. First, the integration of $d\hat{y}$ is carried out to arrive at:

$$H_z = \frac{J_c}{4\pi} \int \frac{1}{(\hat{x}^2 + \hat{y}^2 + \hat{z}^2)^{1/2}} \Big|_{\hat{y}=y-k_1x'-d_1}^{y-k_2x'-d_2} d\hat{x}d\hat{z}. \quad (5.3)$$

After inserting the boundaries the equation can be rewritten to resemble the initial equation by substituting:

$$\chi_j = (c_j - x') \quad \text{where} \quad c_j = (x + k_j(y - d_j))/(1 + k_j^2) \quad \text{and} \quad dx' = -d\chi, \quad (5.4)$$

$$v_j = (k_j x - (y - d_j))/(1 + k_j^2), \quad (5.5)$$

$$\zeta_j = (z - z')/(1 + k_j^2)^{1/2} \quad \text{and} \quad dz' = -d\zeta(1 + k_j^2)^{1/2}, \quad (5.6)$$

where $j = 1, 2$ identifies the lines. The integration is build up of the function K_z which is given by:

$$K_z(\chi_j, v_j, \zeta_j) = \frac{J_c}{4\pi} \int \frac{1}{(\chi_j^2 + v_j^2 + \zeta_j^2)^{1/2}} d\chi_j d\zeta_j \quad (5.7)$$

where the definite integral is replaced with an indefinite integral. The integration of $d\chi_j$ results in:

$$K_z(\chi_{i,j}, v_j, \zeta_j) = \frac{J_c}{4\pi} \int \sinh^{-1} \sqrt{\frac{\chi_{i,j}}{v_j^2 + \zeta_j^2}} d\zeta_j. \quad (5.8)$$

The index i identifies the respective boundary for $\chi_{i,j}$. After the final integration the Biot-Savart law for a trapezoidal sample volume with a constant current density yields the expression:

$$K_z(\chi_{i,j}, v_j, \zeta_{j,k}) = \frac{J_c}{4\pi} \left[\chi_{i,j} \sinh^{-1} \sqrt{\frac{\zeta_{j,k}^2}{\chi_{i,j}^2 + v_j^2}} - v_j \tan^{-1} \left(\frac{\chi_{i,j} \zeta_{i,k}}{v_j \rho_{i,j,k}} \right) + \zeta_{j,k} \sinh^{-1} \sqrt{\frac{\chi_{i,j}^2}{v_j^2 + \zeta_{j,k}^2}} \right], \quad (5.9)$$

where the index k in $\zeta_{i,k}$ has the same purpose as i and j , and $\rho = \sqrt{\chi^2 + v^2 + \zeta^2}$ is a newly introduced parameter (indexes not written). The \sinh^{-1} is the inverse hyperbolic sine and \tan^{-1} is the inverse tangent. With K_z the magnetic field distribution of a trapezoid can be calculated by inserting the correct boundary values:

$$\begin{aligned} H_z(\mathbf{r}) = & K_z(\chi_{2,2}, v_2, \zeta_{2,2}) - K_z(\chi_{2,2}, v_2, \zeta_{2,1}) \\ & - K_z(\chi_{2,1}, v_1, \zeta_{1,2}) + K_z(\chi_{2,1}, v_1, \zeta_{1,1}) \\ & - K_z(\chi_{1,2}, v_2, \zeta_{2,2}) + K_z(\chi_{1,2}, v_2, \zeta_{2,1}) \\ & + K_z(\chi_{1,1}, v_1, \zeta_{1,2}) - K_z(\chi_{1,1}, v_1, \zeta_{1,1}). \end{aligned} \quad (5.10)$$

A calculated field distribution of one trapezoid/sub-element is shown in figure 5.1B. The solid lines represent the edges of the trapezoid and the dash-dotted line indicates where the field is zero. The color bar to the right of the image indicates the positive and the negative field values. In transport current measurements the field profile is similar to the one shown in figure 5.1B, because the current is flowing in one direction (although the lines in the figure should be parallel to the x -axis, for tapes usually have a rectangular cross section).

In contrast to critical current measurements, the current circulates in the sample in scanning Hall-probe microscope (SHPM) measurements, because the current path has to be closed. This leads to field profiles that have a rooftop-shape (cf. section 2.2). To construct such a field profile four trapezoids are translated and rotated by utilizing elemental matrix transformations. An example for a matrix translation is shown in figure 5.1C, where the dotted shape indicates the initial position of the trapezoid. After the translation the trapezoid is rotated in figure 5.1D about the z -axis.

By positioning the sub-elements correctly, the field profile of a rectangular sample can be constructed, which in turn can be rotated or translated via matrix operations (figure 5.1E and 5.1F). If the sample is not a rectangle or square the trapezoids may have more complicated shapes, or more than one sample may be measured at once (figure 5.1G). Equation (5.10) can be used to build and calculate various shapes such as in figure 5.1H.

The developing field profiles are calculated by following the same argumentation as for the calculation of the magnetic moment in section 2.2 with equations (2.6) and (2.7).

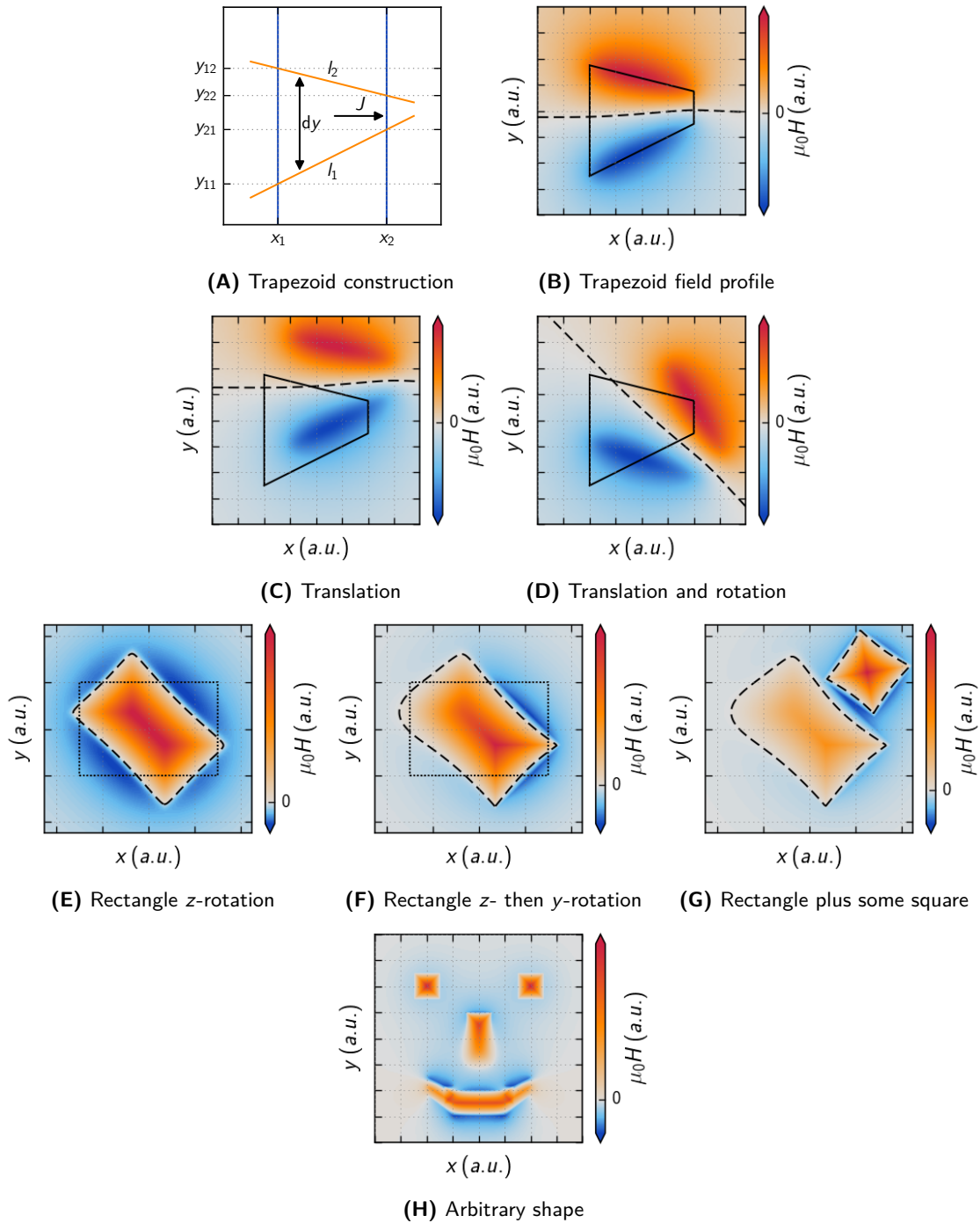


Figure 5.1: Sketch of the construction of a trapezoid and the corresponding field profile for a current flowing in positive x -direction, where the dashed-dotted lines indicates zero field. The figures C and D show how basic matrix operations can be applied to orientate the trapezoid. The other figures show examples of how the correct configuration of trapezoids can be used to calculate the field profile of more complex samples.

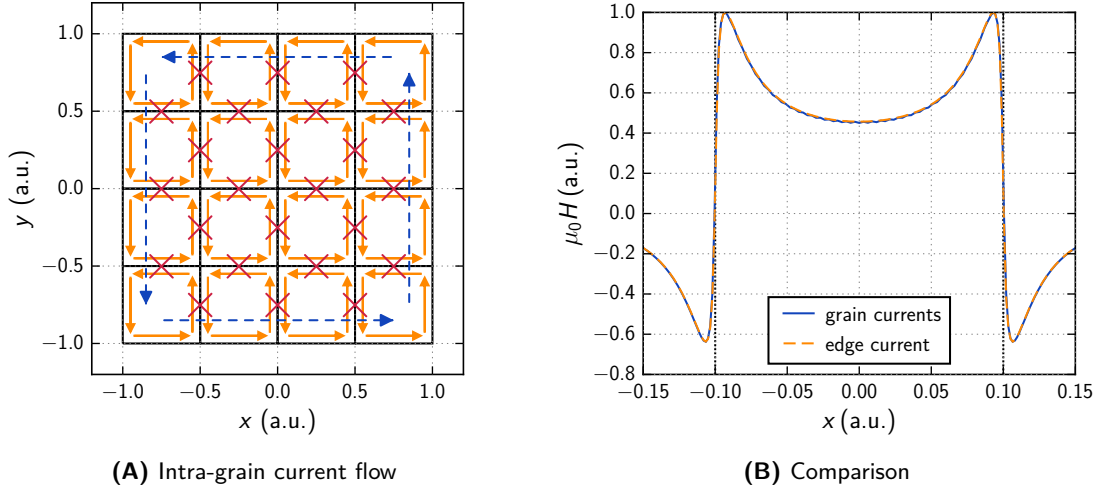


Figure 5.2: Model of the intra-grain current flow in a polycrystal and the comparison between the field profile originating from a current flowing only at the sample edges and the field profile corresponding to a polycrystal with 10^5 grains. The distance to the sample surface is equal to the edge length of the grains: $2s_0$.

5.2 Polycrystals

J_c and J^G are extracted from SHPM data, i. e. the field profiles above the samples. J_c is extracted by fitting the analytical function derived in the previous section to the global field profile, where the spatially constant current density J_c is the only free parameter.

The grains of the polycrystal are described with the same equation, but the calculation of the intra-grain field profile resulting from the individual grains is time consuming, because of the large number of grains. Therefore, a more efficient model is needed.

J^G is confined to the individual grains, which is illustrated in figure 5.2A. The squares in the figure represent the grains and J^G is indicated by the small, solid arrows. These currents generate a field which can be detected with a Hall-probe. If the distance between the Hall-probe and the sample surface is larger than the dimensions of the grains, the contribution of J^G of neighboring grains, cancel each other in a first order approximation (characterized by the crossed out arrows), except for a narrow region at the sample edges.

The thickness of the surface layer, in which the net current flows that describes the field profile of all grains most accurately, is determined using geometrical considerations. The grains can be split into four isosceles triangle in which the current flows in one direction. Utilizing the arguments from above, three parts are negated by the neighboring grains and can be neglected in the modeling (two parts can be neglected if the grain is located at a corner). The only part left is the one at the sample edge. The thickness of the surface layer can be approximated with $s_0/3$ (empirically determined), which corresponds to the distance between the geometric center of the isosceles triangle and the surface.

Thus, the intra-grain field profile can be defined by a field profile resulting from a current density, J^G , flowing in a thin surface layer of thickness $s_0/3$ (indicated by large dashed arrows in figure 5.2A). The resulting field profile from this edge current density is plotted in figure 5.2B together with the field profile calculated for a total number of 10^5 cubic grains. Thereby, the current density inside the grains is equal to the „surface current density“, i. e. J^G . The error between the curves is about 0.03% if the distance between surface and Hall-sensor is $2s_0$. This error increases significantly for distances smaller than the grain size. The number of grains in the sample does not affect the error as strong as the distance. For instance, for a total number of 100

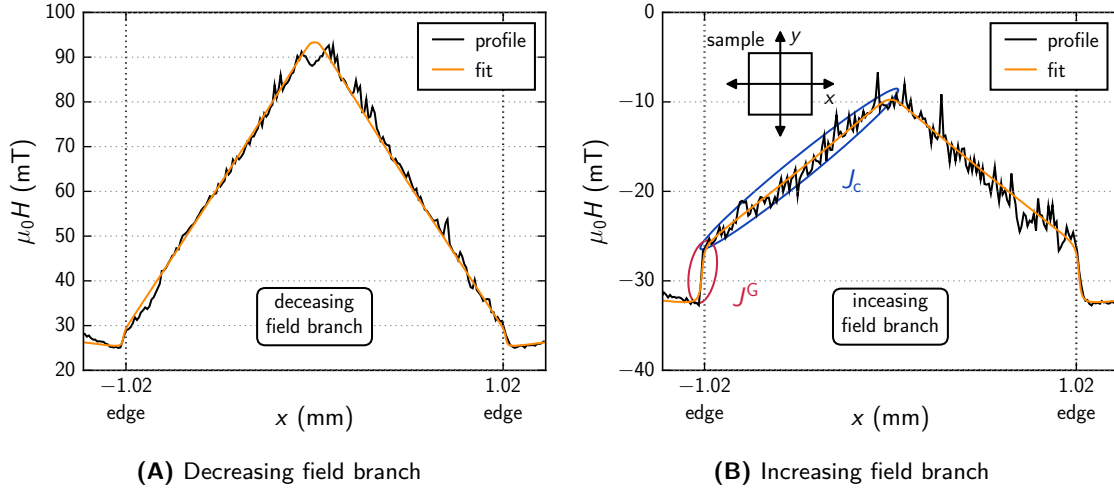


Figure 5.3: Examples of fits to the field profiles of the medium grained K doped sample on the decreasing (A) and the increasing field branch (B). The dotted vertical lines indicate the sample edges. The scans were performed across the sample center.

grains (i. e. s_0 is larger than in the calculation with 10^5 grains) the error is still below 5 % at a distance of $2s_0$.

Figure 5.3 shows examples of field profiles obtained from the medium grained K doped sample and fits utilizing the approach described above. The field profiles were recorded along a field run, where the external applied field (H_{ext}) was ramped from 3 to -3 T. First the field profile was measured on the decreasing field branch at $\mu_0 H_{\text{ext}} = 0.03$ T and then on the increasing field branch at -0.03 T. J^G can be identified as the slopes at the sample edges, while J_c is proportional to the slope in the remaining sample space, as indicated in figure 5.3B.

The SHPM measurements have the advantage that J^G is measured directly, therefore the separation into representative reversible intra-grain current density (J_{rev}^G) and representative irreversible intra-grain current density (J_{irr}^G) as proposed by Svistunov and D'yachenko [Svi92] is not necessary. Another advantage of the direct measurement of J^G is that the determining pinning mechanisms inside the grains do not have to be known (e. g. surface or bulk pinning).

In order to make the SHPM results comparable to the magnetometry data, the obtained values for J_c and J^G can be converted into a magnetization value by using the formulas for cubic samples introduced in section 2.2.

Chapter 6

Experimental Results and Discussion

Aus Steinen, die dir in den Weg gelegt werden, kannst du etwas Schönes bauen.

Translation: *You can build something beautiful with the stones placed in your path.*

— Johann Wolfgang von Goethe

Two current densities can be distinguished in weakly linked polycrystalline superconductors (SCs), the inter-grain current density (J_c) and the intra-grain current density (J_{intra}). J_c describes the global current flow, while J_{intra} is a local current density flowing inside the grains.

The current densities cannot be treated separately in weakly linked SCs, because one influences the other. The field dependences of J_c and J_{intra} are determined by many parameters, for instance the characteristic grain size (s_0) or superconducting parameters such as the magnetic penetration depth (λ). All these values are assumed to be independent of the external applied field (H_{ext}) in the field range that is experimentally accessible by the utilized measurement devices. Therefore, the equations derived in chapters 3 and 4 can be used to evaluate the measurements without further assumptions and the only quantities that influence J_c and J_{intra} are H_{ext} and its history, as well as the current densities themselves.

A finite value of J_c corresponds to a field gradient inside the sample, so that grains closer to the edges feel a different field than those closer to the center. The value of J_{intra} is determined by this local field and each grain would have to be modeled separately, which is difficult and time consuming. Therefore, J_{intra} is replaced by a representative intra-grain current density (J^G), which describes an average over all grains.

J^G originates from two mechanisms. One is the representative reversible intra-grain current density (J_{rev}^G), which stems from the reversible properties of the grains, and the other is the representative irreversible intra-grain current density (J_{irr}^G), which results from pinning. The sign of J_{irr}^G is preserved while H_{ext} is ramped in a certain direction, i.e. the sign is defined by the sign of dH_{ext}/dt , where t is the time, while the sign of J_{rev}^G is determined by the sign of H_{ext} . The value of J^G is larger when $|H_{\text{ext}}|$ is increased (increasing field branch), because J_{rev}^G and J_{irr}^G have the same orientation. The current densities have opposing signs when $|H_{\text{ext}}|$ is decreased (decreasing field branch), therefore J^G is smaller.

J_c and J^G are visible in scanning Hall-probe microscope (SHPM) measurements, where the global field gradient, that originates from J_c , is referred to as inter-grain field profile. The field profile, which is generated by J^G , exhibits a large field gradient at the sample edges while the field distribution above the center is rather flat. Such a field profile is referred to as an intra-grain field profile.

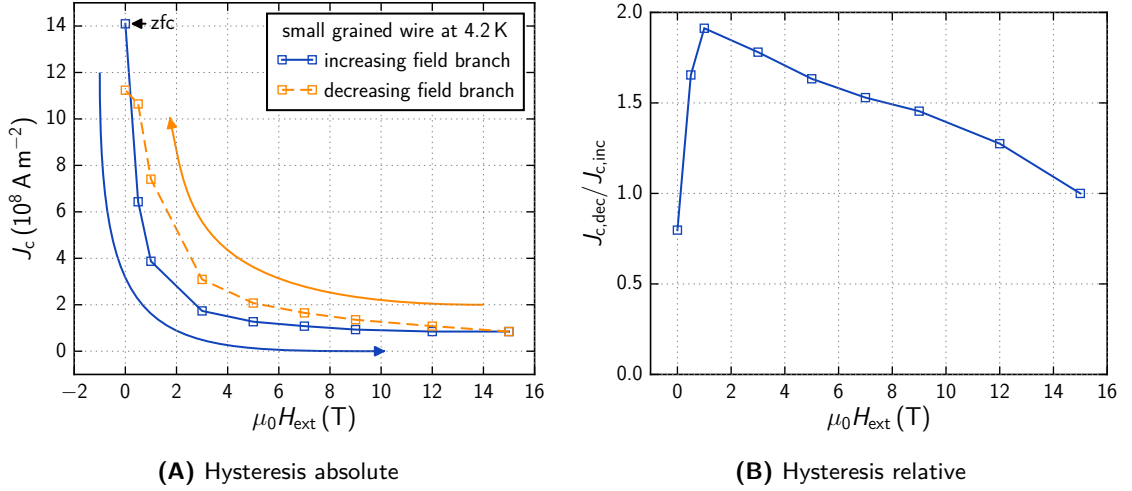


Figure 6.1: Hysteresis of the inter-grain current density (J_c) and the ratio between the increasing ($J_{c,inc}$) and decreasing field branch ($J_{c,dec}$). (Data provided by J. D. Weiss.)

6.1 Saturated Field Profile

The saturated field profile denotes the case where the inter- and intra-grain field profiles of a sample are independent from the magnetic history, i.e. the background field (H_{bg}) and the maximum applied field (H^{max}) do not affect the magnetic signal.*

6.1.1 Hysteresis of the Inter-Grain Current Density

A consequence of the weak-link character of the grain boundaries (GBs) in high-temperature superconductors (HTSs) is a hysteresis of J_c [Dau92; Eve88; Kun98; Lis97; McH89], where the values are smaller on the increasing field branch compared to the decreasing field branch. A related effect is the shift of the maximum value in a magnetization curve. The maximum occurs on the increasing field branch in a crystal, because of the self-field generated by the trapped magnetic flux. In polycrystalline HTSs, the maximum of the inter-grain contributions is expected to occur at zero if the contribution of the grains to the signal is negligible [Sha99]. This peak is shifted to the decreasing field branch when the contributions of the grains become important.

Figure 6.1A shows a transport current measurement of a K doped Ba-122 wire, where $s_0 \approx 0.1 \mu\text{m}$. The hysteresis can be very pronounced as indicated in figure 6.1B where the ratio between J_c on the different branches is approximately 2 at 1 T. Weiss et al. [Wei12] investigated equally synthesized samples as the ones discussed in this chapter and found that J_c obtained from transport current measurements and magnetization loops are in good agreement with each other. Thus, transport and magnetization measurements should both show signs of the J_c hysteresis. In a magnetization loop, the J_c hysteresis manifests as an asymmetry between the increasing and decreasing field branch, which is visible in figure 6.2 for the K and Co doped samples. The increasing field branch of the small grained K doped sample is mirrored about the x -axis and the difference between the field branches is highlighted by the shaded areas.

The measurements on the K doped samples are displayed in figure 6.2A. On the increasing field branch, the magnetization curves of the samples with different grain sizes exhibit very similar characteristics for $\mu_0 |H_{ext}| > 0.5 \text{ T}$, while they have different features on the decreasing field branch. The data obtained from the large grained sample (dotted line) corresponds to the magnetization curve of crystals with the maximum in the magnetization curve on the increasing

* If the magnetic signals depends on H_{bg} , the corresponding field profile is referred to as developing, while the case where it depends on H^{max} is called the reverse field profile.

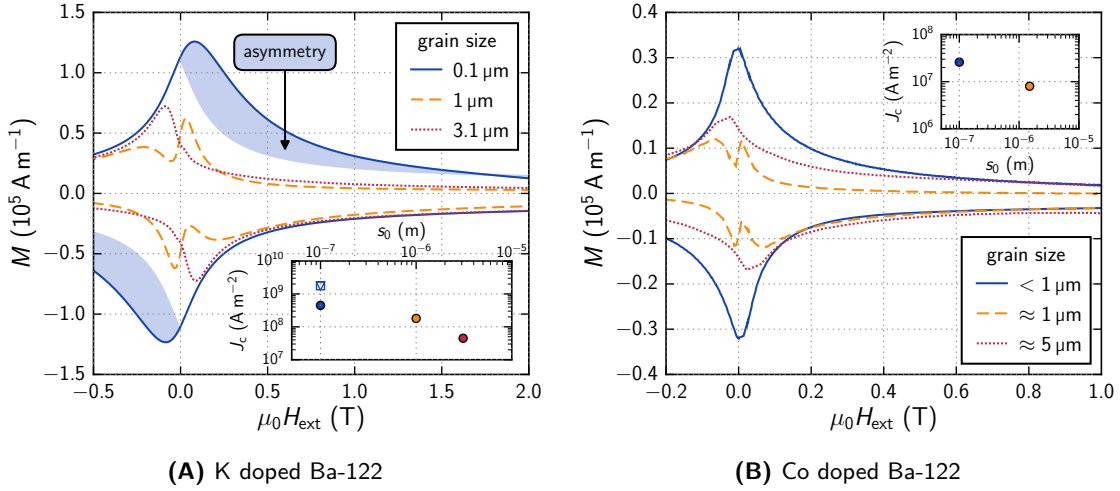


Figure 6.2: Magnetization (M) of K and Co doped Ba-122 polycrystals with different grain sizes as a function of external applied field (H_{ext}). The background signal, measured 5 K above the superconducting transition temperature of the respective samples, was subtracted from the measurements. The insets show the dependence of the maximum inter-grain current density (J_c) on the characteristic grain size (s_0). The measurements were carried out at 5 K in a vibrating sample magnetometer.

field branch and a small asymmetry. The asymmetry increases with decreasing s_0 and another peak near $H_{\text{ext}} = 0$ emerges for $s_0 = 1 \mu\text{m}$ (dashed line). This peak is located on the decreasing field branch and becomes larger and wider for $s_0 = 0.1 \mu\text{m}$ (solid line), while the peak located on the increasing field branch disappears. The small grained samples have the largest M on the decreasing field branch.

The Co doped samples exhibit similar properties. The largest asymmetry and M are observed in the sample with the smallest grain size, two peaks occur in the magnetization curve of the medium grained sample, and only one peak is present in the large grained sample, which is located on the increasing field branch. This indicates that the asymmetry effects are governed by the grain size and not by the dopant. Thus, the focus in this thesis is upon the results obtained from the K doped samples, because the field range, in which the interesting effects occur, is larger than in the Co doped samples (note the differences between the field axes in figures 6.2A and 6.2B).

In order to describe the asymmetry in magnetization measurements, Palau et al. [Pal07] calculated the return field (H_{return}) for cylinders with a saturated field profile, which are described by the critical state model. These cylinders represent grains. The authors consider two isolated adjacent grains with zero separation that contribute to H_{return} at the GB to allow a quantitative evaluation of J^G with the equation:

$$J^G = \frac{H_{\text{return}}}{x^G L}, \quad (6.1)$$

where L represents the length of a cylinder. The dimensionless factor x^G is calculated numerically and depends on the aspect ratio of the grain dimensions. J^G can be estimated with equation (6.1) if H_{return} and L are known. The factor x^G is smaller than 0.5 for a moderate aspect ratio between dimensions orthogonal ($2s_0$) and parallel (L) to H_{ext} : $2s_0/L < 4$ [Par04]. The grains are approximated by cubes in this thesis, therefore $s_0 = L/2$ and $x^G \approx 0.15$ [Par04].

Since s_0 is known, J^G can be estimated by equation (6.1) if H_{return} can be determined. Evetts and Glowacki [Eve88] ascribed the shift of the magnetization peak from the increasing to the decreasing field branch to H_{return} . The maximum magnetization value is expected when the local field at the GB is zero, i. e. $H_{\text{ext}} + H_{\text{return}} = 0$ [Pal04; Sha99], so that H_{return} (at the peak)

should coincide with the field at which the maximum magnetization occurs. Thus, $\mu_0 H_{\text{return}}$ would be approximately 0.1 T in the small grained sample and $J^G > |H_{\text{return}}|/s_0 \approx 10^{12} \text{ A m}^{-2}$. A comparison between this value and the maximum current density found in K doped Ba-122 crystals: $5 \cdot 10^{10} \text{ A m}^{-2}$ [Kih13], indicates that H_{return} on its own is a questionable explanation for the observed behavior, although such large J^G cannot be excluded at this point.

The model, presented in chapter 4, can account for this shift by utilizing much smaller values of J^G . The position of the maximum J_c is determined by phase shift at the GB due to J^G (cf. section 4.3), so that a value of approximately $3 \cdot 10^9 \text{ A m}^{-2}$ on the decreasing field branch is sufficient to account for the experimental data.

Another intriguing observation is that the maximum J_c increases when the grain size becomes smaller. The insets in figure 6.2 display the dependence of the maximum J_c on s_0 . The triangle and the square in the inset of figure 6.2A are evaluations from other small grained samples whose magnetization curves are not shown in figure 6.2A. The maximum J_c exhibits an inverse dependence on s_0 in the investigated samples. A similar behavior was found in other HTS bulks [Kuw89] and tapes [Sol07]. The exact measurement conditions applied by Kuwabara and Shimooka [Kuw89] are not specified in the publication, while Solovyov, Wiesmann, and Suenaga [Sol07] conducted the measurements in self-field. The interpretation based on self-field measurements is problematic because many effects contribute to the limitation of J_c near zero field. In particular, the presented model predicts that the position of the maximum J_c on a magnetization curve depends on J^G . Thus, the increase of J_c found by Solovyov, Wiesmann, and Suenaga [Sol07] could originate from different positions of the J_c peak in the respective samples, although the quantitative increase of J_c corresponds to the behavior observed in the investigated Ba-122 samples.

Solovyov, Wiesmann, and Suenaga [Sol07] attributed the increase of J_c to an improvement in the crystallographic order of the grains due to the reduction of the grain size, while Kuwabara and Shimooka [Kuw89] proposed that their observation originates from the weak-link behavior of the GBs. Only two iron based compounds with three different grain sizes are investigated in this thesis, therefore the significance of the dependence of the maximum J_c on s_0 is difficult to judge. Nonetheless, the results suggest that the maximum J_c can be increased by reducing the grain size of polycrystalline Ba-122 wires.

6.1.2 Temperature Dependence

Figure 6.3 shows the temperature dependence of M of the K doped Ba-122 bulks at 5, 10, and 20 K. On the increasing field branch, the magnetization curve of the large grained sample (figure 6.3A) does not change when the temperature is increased, except for the expected decrease of the magnetic signal. This is different on the decreasing field branch, where M becomes constant at 20 K while it increases with decreasing fields at lower temperatures. This indicates that a small contribution of J_c is present in the large grained sample at low temperatures, that vanishes within the experimental resolution at 20 K. A detailed examination of the magnetization curve supports this assumption, because a small „elevation,“ i. e. a J_c peak, is observable on the decreasing field branch at 5 and 10 K but not at 20 K. In contrast to the large grained sample, J_c does not vanish at 20 K in the other samples, i. e. the magnetization curves are similar at all temperatures.

The magnetization curves of the medium grained sample shown in figure 6.3B exhibit two peaks at all temperatures. The ratio of M between the two peak positions is more or less independent of the temperature, i. e. the peak on the decreasing field branch (J_c) is always approximately 1.5 times larger than the one on the increasing field branch (J^G). An increase of the temperature causes the peaks to occur closer to zero field, which is expected because the current densities are smaller. The behavior of the small grained sample (figure 6.3C) is comparable to medium grained sample. In this thesis, the temperature dependence of the parameters in equation (4.21) is explicitly considered. However, the magnetization curves in figure 6.3 exhibit the expected behavior, if typical temperature dependence are assumed.

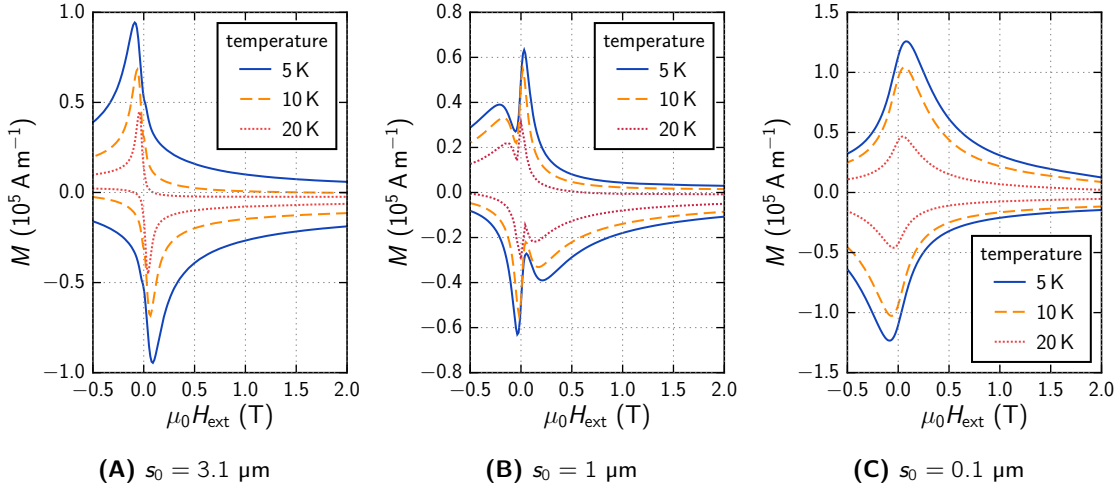


Figure 6.3: Temperature dependence of the magnetization (M) of the K doped Ba-122 polycrystals with different characteristic grain size (s_0), from similar measurements as in figure 6.2.

A detailed investigation of the temperature dependence was done, to analyze in which temperature range the presented model works. Since the J_c hysteresis is indicative for the presented model, these measurements were carried out on the small grained sample, where these effects are largest. The magnetization curves showed, that the hysteresis persist up to 34 K ($T_c = 35.7$ K), which suggests that the model is applicable in the whole superconducting temperature range. The following discussion will focus on the measurements at 5 K, where the signals are strongest.

6.1.3 Scanning Hall-Probe Microscopy

Magnetization measurements are a fast, non-destructive, and straightforward techniques that provide general information on a sample, but an accurate determination of J_c and J^G is very difficult in polycrystalline samples. The SHPM is a tool to detect and evaluate J_c and J^G .

Figure 6.4A displays the field profiles of the small grained K doped sample at various fields along a run from 3 to -3 T. The field profiles are shaped (roughly) in accordance with the extended critical state model, i.e. a constant slope that corresponds to an invariant J_c . The maximum in the magnetization curve (0.1 T) coincides with the field profile with the steepest slope in the SHPM scans. A contribution of J^G is not observable, which illustrates that the peak in the magnetization curve of the small grained sample originates from J_c . Thus, the peak on the decreasing field branch is refer to as the inter-peak.

After the determination of J_c by fitting the field profiles with the procedure described in chapter 5, the values can be recalculated into a magnetization ($M_{\text{inter}}^{\text{SHPM}}$), which is compared to the magnetization measured by a SQUID magnetometer (M^{SQUID}) in figure 6.4B. $M_{\text{inter}}^{\text{SHPM}}$ clearly follows the magnetization loop. The slope of the field profile at 0.1 T coincides with a J_c of approximately $4 \cdot 10^8 \text{ A m}^{-2}$ (10 K). On the increasing field branch, the field profile starts to „collapse“ from the sample edges towards the center, leaving a significantly reduced slope ($J_c \approx 10^8 \text{ A m}^{-2}$ at -0.5 T). The difference in the magnitude of the slope at comparable positive and negative fields in figure 6.4A is striking. For instance, the slope at 0.5 T is approximately 2.5 times larger than at -0.5 T.

Further evidence, that H_{return} alone cannot be responsible for the J_c hysteresis, is visible in figure 6.4A. Simply put, H_{return} has to be of the order of the trapped field inside the grains which corresponds to the height of the field step at the sample edges. This argument includes scenarios where the magnetic grain size differs from s_0 , i.e. the formation of grain clusters, which

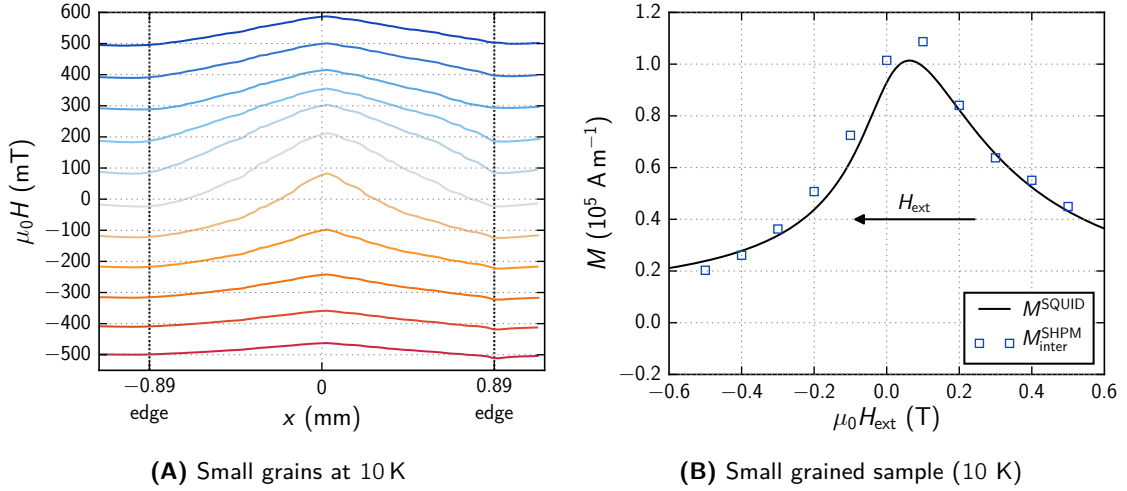


Figure 6.4: Scanning Hall-probe microscope (SHPM) measurements of the small grained K doped sample and the corresponding magnetization (M) at 10 K, where the contribution of the inter-grain current density ($M_{\text{inter}}^{\text{SHPM}}$) is shown. The magnetization obtained from Hall-scans is compared to the magnetization measured by a SQUID magnetometer (M^{SQUID}). The sample was cooled in zero field, then the field was ramped to 3 T. During the subsequent run to -3 T the field profile of the sample was measured at certain external applied field (H_{ext}), which are indicated by the labels in A. The spatial extent of the samples is given by the vertical dotted lines. The Hall-probe was at a constant z -position, and the distance to the sample surface was approximately $20 \mu\text{m}$ during the scans.

are characterized by a number of connected grains with small angle GBs that do not hinder the current transport within the cluster and therefore behave like a single grain. However, a field step of the order of 0.1 T is not present in the SHPM measurements in figure 6.4A.

The field profiles of the large grained sample, displayed in figure 6.5, exhibit a rather flat field distribution except for a large field gradient at the sample edges, which is characteristic for field profiles dominated by the contribution of the individual grains. A global slope between the sample edge and the center, which indicates the presence of J_c , is hard to discern. The inter-grain contribution can be seen in the left half of the sample in the 50, 25, and 0 mT measurements in figure 6.5A. The distance between the Hall-probe and the sample surface was small in the right half of the sample, so that the signals of J^G dominate.

The contributions of J_c and J^G to the magnetic signal of the large grained sample are plotted in figure 6.5B. Again, the field profiles are fitted and the corresponding J_c and J^G are recalculated into a magnetization ($M_{\text{inter}}^{\text{SHPM}}$ and $M_{\text{intra}}^{\text{SHPM}}$), which is compared to the SQUID measurement. The maximum J^G , measured at -0.07 T, is about $2.2 \cdot 10^{10} \text{ A m}^{-2}$. A very small contribution of J_c is visible on the decreasing field branch on the left side of the sample. The largest J_c is observed at 25 mT and is about $4.5 \cdot 10^7 \text{ A m}^{-2}$. The measurements show that the peak in the magnetization of the large grained sample is caused by J^G .

The data points in figure 6.5B are acquired by fitting the left half of the sample in figure 6.5A (negative x -axis). The results of the evaluation are less accurate if the right side is used, where the Hall-probe was in close proximity to the sample surface, although the measurement obtained from the SQUID magnetometer is still clearly reproduced. This discrepancy between left and right sample edge is caused by the insufficient distance between the Hall-probe and sample surface on the right side. J^G is a representative value in the evaluation of the field profiles, which neglects the fact that the field profile is actually composed of the contributions of the individual grains. Their field profiles are visible on the right side of the measurement because the Hall-probe does not detect the average M of many grains but rather the signal of single grains.

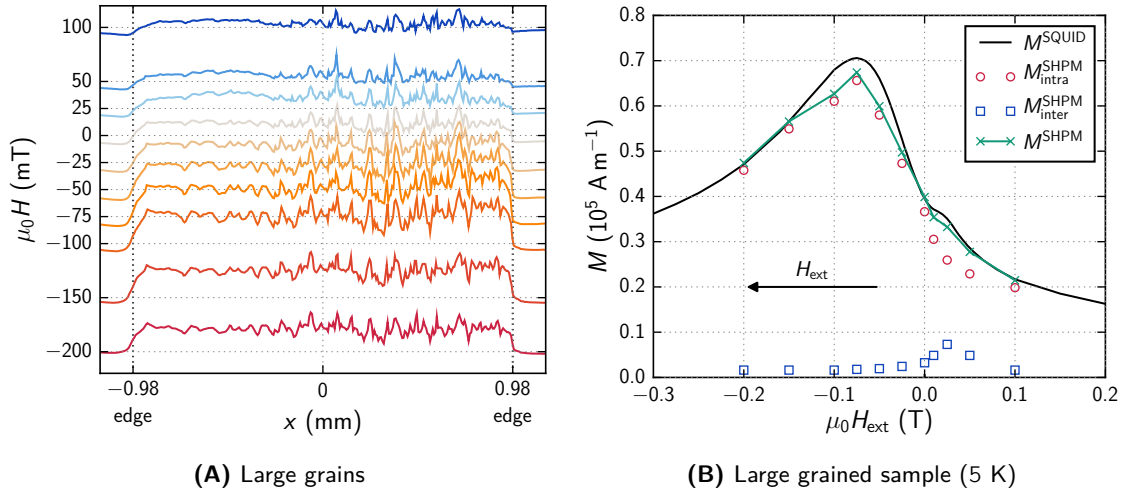


Figure 6.5: Scanning Hall-probe microscope (SHPM) measurements of the large grained K doped sample and the corresponding magnetization values (M) at 5 K, where the contribution of the inter-grain current density ($M_{\text{inter}}^{\text{SHPM}}$) and the contribution of the intra-grain current density ($M_{\text{intra}}^{\text{SHPM}}$) are shown together with their combined value (M^{SHPM}). The magnetization obtained from Hall-scans are compared to the magnetization measured by a SQUID magnetometer (M^{SQUID}). The sample was cooled in zero field, then the field was ramped to 3 T. During the subsequent run to -3 T the field profile of the sample was measured at certain external fields, which are indicated by the labels in A. The spatial extent of the samples is given by the vertical dotted lines. The Hall-probe was at a constant z -position, and the distance to the sample surface was approximately $20 \mu\text{m}$ at the left edge and $3 \mu\text{m}$ at the right edge because of a tilted sample surface.

The measured field profiles of the sample with the medium sized grains show the combined behavior of the large and small grained sample (figure 6.6A). When the field is ramped from H^{max} to zero, the inter-grain field profile builds up, while hardly any contribution of J^{G} is observed. The maximum slope in the inter-grain field profile (i. e. J_c) corresponds to the peak of M on the decreasing field branch. After the peak, J_c becomes smaller and the slope at the sample edges (J^{G}) increases until the field profiles resemble those of the large grained sample.

The resolution of the Hall-probe is not sufficient to detect any intra-granular field profiles in the small grained sample (grain size smaller than the dimensions of the active area of the Hall-probe). J_c is resolvable in the large grained sample, but the magnitude is small. Furthermore, the field interval in which both current densities can be evaluated is rather small in the large grained sample (between ± 0.1 T). Therefore, the small and large grained sample are not ideal for quantitative evaluations. The focus of the following discussions is placed on the medium grained sample, because it allows the simultaneous detection of J_c and J^{G} .

Figure 6.6A shows some fits to the field profiles of the medium grained-sample utilizing the procedure described in chapter 5, where the dashed lines represent the fits. The field profiles exhibit a distinct kink when H_{ext} is ramped through zero. This behavior results from the strong field dependence of J_c near zero field. Thus, two values of J_c and J^{G} would have to be fitted to the field profiles, i. e. one for the part that is located on the increasing field branch and one for the part located on the decreasing field branch.* Only the region between the sample edge and the kink was fitted in figure 6.6A (if a kink is present in a field profile). That is why $M_{\text{inter}}^{\text{SHPM}}$ is underestimated near $H_{\text{ext}} = 0$.

* On closer consideration the values of J_c and J^{G} change continuously with the local field inside the sample, but around zero the field dependence of J_c is very strong (cf. figure 4.11B), therefore the region in which the slope changes is comparatively small and thus the inter-grain field profiles near zero seem to have only two distinct slopes; one at the sample edge and one near the center.

The evaluated $M_{\text{inter}}^{\text{SHPM}}$ and $M_{\text{intra}}^{\text{SHPM}}$ from figure 6.6A are shown in figure 6.6B. At $\mu_0 H_{\text{ext}} = 0.03$ T, where the maximum M is observed, the slope of the inter-grain field profile corresponds to a J_c of approximately $1.8 \cdot 10^8$ A m⁻². The evaluated J^G at the intra-grain peak position (-0.17 T) is approximately $3.7 \cdot 10^{10}$ A m⁻².

The J^G values from the SHPM data in figure 6.7, together with equation (4.21) are used to calculate the expected J_c according to the presented model. This J_c is then recalculated to a magnetization ($M_{\text{inter}}^{\text{model}}$). The grain size distribution parameters $u = 3$ and $s_0 = 1$ μm were evaluated from images of the sample surface (cf. figure 2.1). The self-field of the sample is taken into account by substituting $B = \mu_0 H_{\text{ext}} + \Delta B_{\text{profile}}^{\text{SHPM}}/2$ in equation (4.13), where $\Delta B_{\text{profile}}^{\text{SHPM}}$ is the difference between the maximum and minimum field value of the (measured) field profile. The characteristic thickness of the GBs (d), λ , and the maximum inter-grain current density (J_{c0}), are the fitted parameters. The obtained $M_{\text{inter}}^{\text{model}}$ values are plotted in figure 6.7 for comparison with $M_{\text{inter}}^{\text{SHPM}}$.

Figure 6.7 shows the advantage of combining a large area and high resolution SHPM. The sum of $M_{\text{inter}}^{\text{SHPM}}$ and $M_{\text{intra}}^{\text{SHPM}}$ clearly reproduced the unconventional double peak in M^{SQUID} and $M_{\text{inter}}^{\text{model}}$ closely follows $M_{\text{inter}}^{\text{SHPM}}$. The fit value of $J_{c0} = (1.8 \pm 0.4) \cdot 10^8$ A m⁻² corresponds to the maximum J_c extracted from the field profiles in figure 6.6A ($J_c = 1.8 \cdot 10^8$ A m⁻²). The penetration depth ($\lambda = 190 \pm 20$ nm) is comparable to the results obtained by Li et al. [Li08], where the authors found a value of 200 nm at 10 K. Kim et al. [Kim14] investigated identically synthesized samples as those in this thesis by atom-probe tomography. Their data show that the length scale of the composition variation of Ba, K, Fe, As and O across the GBs is about 5 to 15 nm. This length is comparable to the fitted total thickness of the GBs: $2d = 5.4 \pm 1.5$ nm.

6.2 Developing and Reverse Field Profiles

The developing field profile refers to the advance of a field gradient towards the sample center when H_{ext} is changed after cooling the SC below T_c at a certain H_{bg} (cf. figure 2.3). The field profile saturates when the field gradient reaches the sample center. The field difference between this point an H_{bg} is termed the first penetration field (H_1^*).

In this thesis, a reverse field profile denotes the inversion of a field profile after the reversal of the field ramp at certain field, H^{max} . This leads to the formation of „two slopes,“ where one is the leftover of the field profile originating from H^{max} , while the second is the reversed slope, which advances towards the sample center and replaces the leftover field profile. The reverse field profile changes into a saturated field profile when the reversed field gradient has replaced the leftover from H^{max} completely. The field difference between H^{max} and this point is denoted the second penetration field (H_2^*).

6.2.1 Characteristic Fields

The two current densities that are present in polycrystals with weakly linked GBs (J_c and J^G) can be described by two sets of characteristic fields. One set is H_1^* and H_2^* , while the second consists of the first (H_1^G) and the second representative penetration field of the grains (H_2^G). The first set describes the inter-grain field profile and the second set the intra-grain field profile. J_c and J^G can be estimated from these fields by equations (2.11) and (2.12), if the size of the sample and the grains is known and the current densities are describable by the extended critical state model. However, this equations are only partly applicable for polycrystals with weakly linked GBs, as will be shown below.

Figure 6.8 shows magnetization measurements on the medium grained sample. The measurements labeled „developing“ illustrate the behavior after cooling the sample below T_c at different H_{bg} . Thus, the field profiles start to develop when H_{ext} is ramped to higher or smaller values. The „reverse“ measurements recorded the reversal of a saturated field profile, so that the first point in a measurement lies on the saturated magnetization curve (M_{sat}). The starting fields were

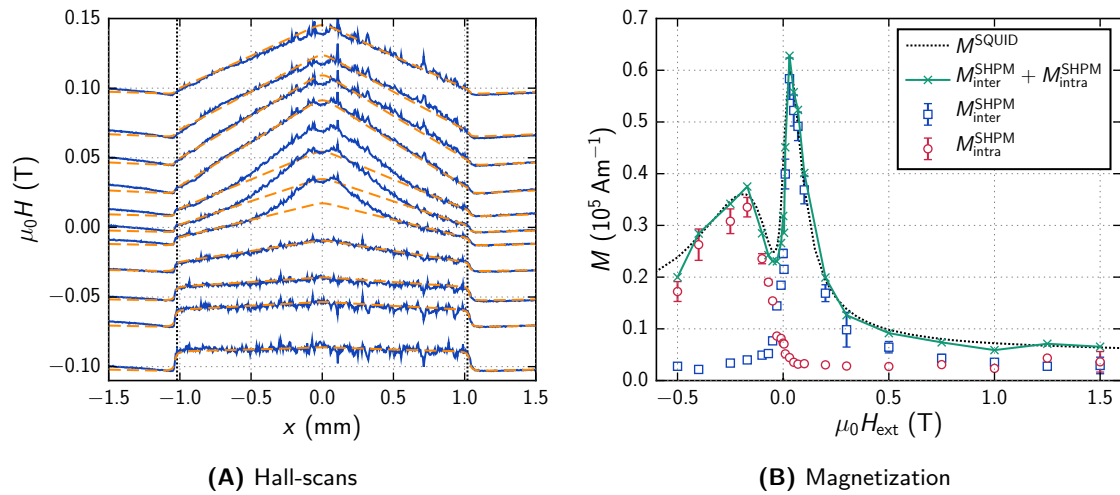


Figure 6.6: Scanning Hall-probe microscope (SHPM) measurements of the medium grained sample, at 5 K, where the dashed curves are the fits to the data near the sample edge. The evaluated magnetization of the contribution of the inter-grain current density (J_c) to the magnetization, which was evaluated from SHPM measurements ($M^{\text{SHPM}}_{\text{inter}}$) and the contribution of the representative intra-grain current density (J^G) to the magnetization, which was evaluated from SHPM measurements ($M^{\text{SHPM}}_{\text{intra}}$) are plotted together with their combined value (M^{SHPM}). The dotted line is the magnetization measured by a SQUID magnetometer (M^{SQUID}). The errors correspond to one standard deviation of the fits.

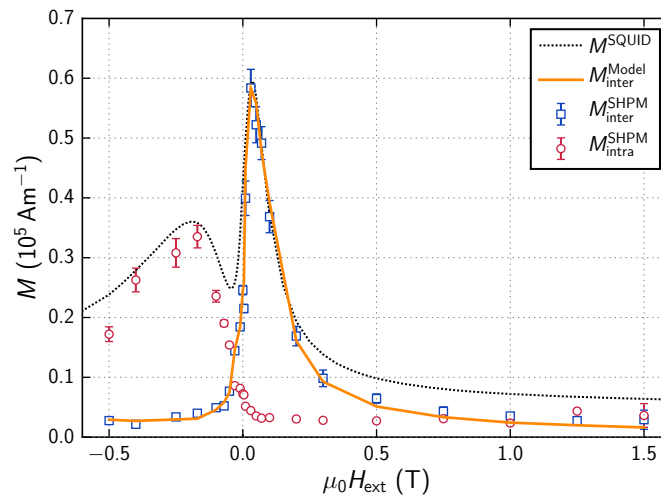


Figure 6.7: Same data as in figure 6.6. The curve labeled $M^{\text{Model}}_{\text{inter}}$ denotes the fit with equation (4.21) to the values evaluated from scanning Hall-probe microscope (SHPM) measurements ($M^{\text{SHPM}}_{\text{inter}}$), where the evaluated representative intra-grain current density (J^G) from the SHPM measurements was used in equation (4.21).

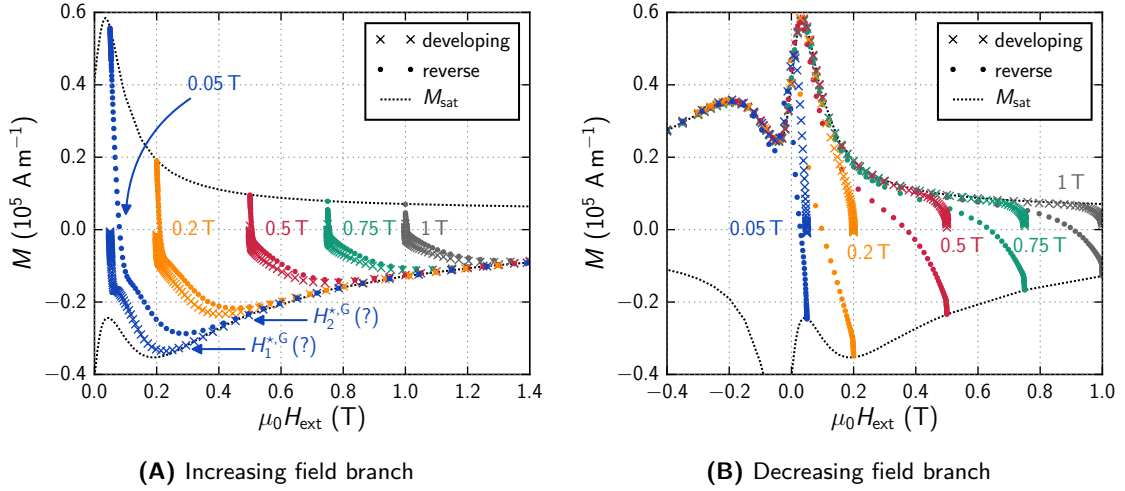


Figure 6.8: Comparison between the developing and reverse field profile in magnetization (M) measurements on the medium grained sample. The dotted line represents the saturated magnetization (M_{sat}). The field values in the plots correspond to the external applied fields (H_{ext}) at which the measurements started.

the same as H_{bg} in the developing measurements. The behavior of the developing and the reverse curves in figure 6.8 is notable because the additional applied field (H_{add}) that has to be set to achieve an overlap with M_{sat} is larger than expected.

The 0.05 T measurement in figure 6.8A is the only one in which the point of the overlap between the developing curve and M_{sat} is distinctly smaller than the overlap of the reverse curve, i. e. approximately 0.3 T and 0.5 T (indicated by H_1^{*G} and H_2^{*G}). In the other measurements, the overlap of the developing and reverse curves with M_{sat} occurs after applying an H_{add} of about 0.4 to 0.5 T. Thus, H_1^{*G} would be approximately equal to H_2^{*G} instead of the expected relation: $H_2^{*G} \approx 2H_1^{*G}$.^{*} The behavior of the developing curves on the decreasing field branch (figure 6.8B) is comparable to those on the increasing field branch, i. e. the curves overlap with M_{sat} after reducing H_{ext} by approximately 0.5 T, except the 0.05 and 0.2 T measurements which overlap shortly after the zero crossing.

The evaluated SHPM scans in figure 6.6 revealed that the contribution of J_c is small on the increasing field branch, thus the measurements in figure 6.8A show mainly the dependence of J^G . Accordingly, the merging points in this figure should define H_1^{*G} and H_2^{*G} , but the calculated J^G from those fields are very large (approximately 10^{12} A m⁻²). Such large values are not observed in the SHPM measurements in figure 6.6.

Figure 6.8 shows that the development and reversal of M is not explainable by the extended critical state model, i. e. the field difference between the first measurement at H_{bg} and the merging with M_{sat} is too large. Another mechanism has to be responsible for this effect.

6.2.2 Scanning Hall-Probe Microscopy

The SHPM scans in figure 6.9 correspond to the 0.2 T measurements in figure 6.8. The solid lines represent the developing and the dashed lines the reverse measurement. H_{ext} was ramped to 5 T and subsequently to 0.2 T before the first measurement of the reverse measurements was conducted in figure 6.9A. The figure shows measurements from 0.2 to 0.3 T, where H_{ext} was increased by 0.01 T between the scans. Further scans were conducted up to 1.2 T. Figure 6.10

^{*} The field steps in the measurement of M_{sat} are 0.05 T at $|\mu_0 H_{\text{ext}}| > 0.2$ T. Therefore, the values of H_1^{*G} and H_2^{*G} are rough estimations.

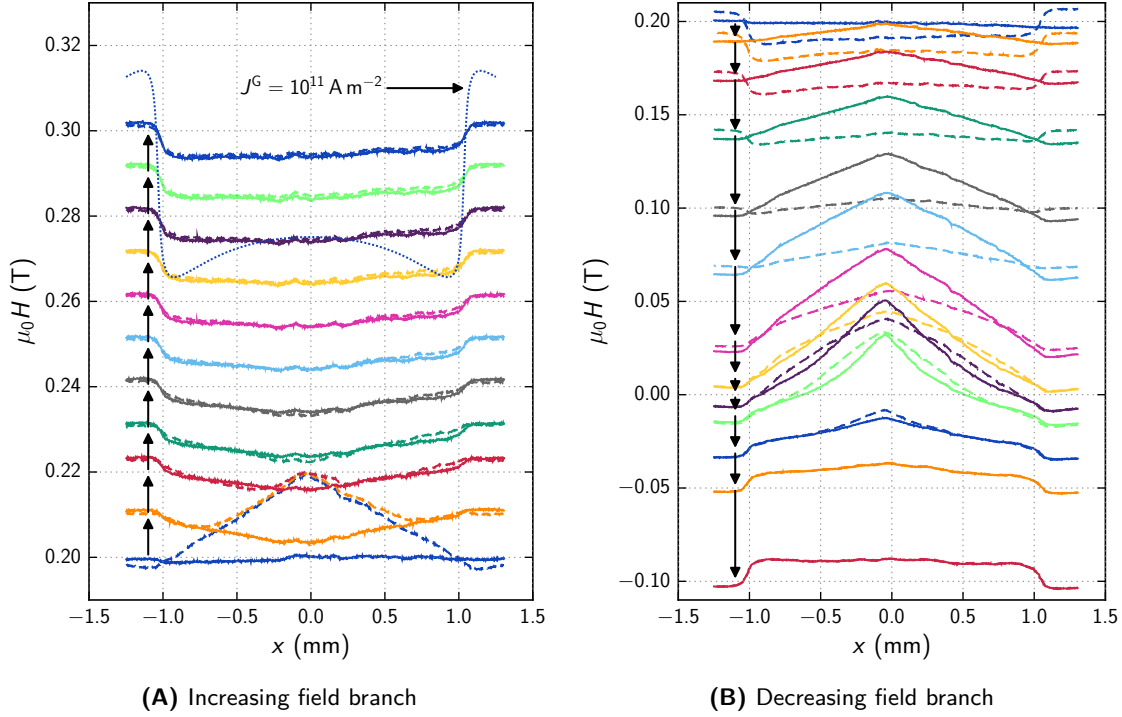


Figure 6.9: Scanning Hall-probe microscope measurements from the medium grained sample at 5 K on the increasing and decreasing field branch, where the solid lines show the developing and the dashed lines the reverse field profiles. All measurement series start at 0.2 T.

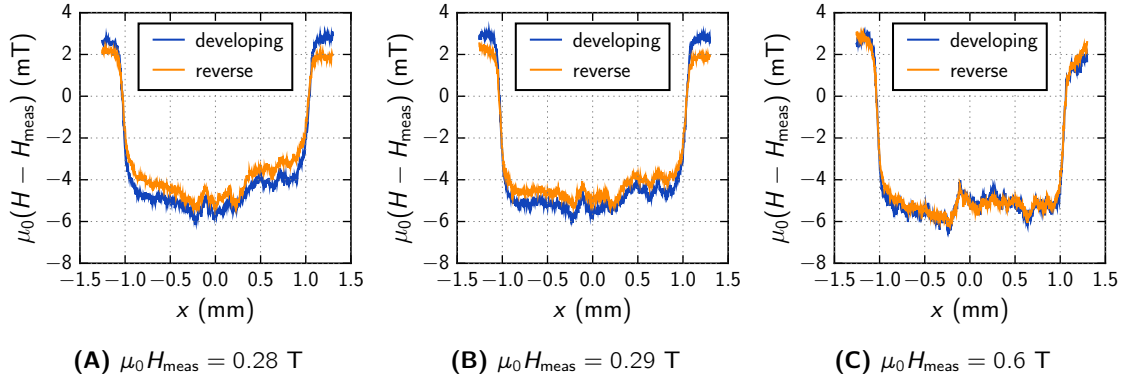


Figure 6.10: Selected field profiles from figure 6.9A, where H_{meas} defines the external applied field in which the measurements were conducted.

displays selected scans, which show that the difference between the field profiles becomes small at $\mu_0 H_{\text{ext}} \gtrsim 0.3 \text{ T}$.

The initial field profile in figure 6.9A (solid line at 0.2 T) is flat after cooling the sample below T_c . The increase of H_{ext} to 0.21 T leads to the formation of a global field gradient, i. e. J_c , which is already saturated at this field and $\mu_0 H_1^*$ can be estimated with 8 mT. A further increase of H_{ext} entails a decrease of the slope of the inter-grain field profile.

The dashed lines in figure 6.9A illustrate the behavior of the field profile in the reverse measurement. A global field gradient is present in the first scan, which is inverted in the subsequent

measurements. The inter-grain field profile is saturated at $\mu_0 H_{\text{ext}} = 0.23$ T, and thus $\mu_0 H_2^*$ can be approximated with 0.025 T. A comparison with the developing measurement shows that the global field gradient is larger in the reverse measurements, but the slope becomes small at $\mu_0 H_{\text{ext}} > 0.28$ T in both measurements. The intra-grain field profiles still have different magnitudes at these fields (cf. figures 6.10A and 6.10B), where the signal from the grains is larger in the developing measurement up to about 0.6 T, where the field profiles finally overlap (figure 6.10C).

The differences between the developing and reverse measurements are more obvious in figure 6.9B, where the field profiles at $H_{\text{ext}} > 0$ are located on the decreasing field branch, while the ones at negative fields are on the increasing field branch. The inter-grain field profile saturates at $\mu_0 H_{\text{ext}} \approx 0.19$ T in the developing measurements. The slope of the inter-grain field profile increases with decreasing field and collapses when the field profile passes zero, while the signal of the grains starts to increase.

H_{ext} was ramped to -5 T before the first scan of the reverse measurement was carried out at 0.2 T (dashed line), so that a saturated intra-grain field profile is present in figure 6.9B. The reduction of H_{ext} leads to the development of a comparatively small slope in the inter-grain field profile, which begins to increase at $\mu_0 H_{\text{ext}} \lesssim 0.07$ T. The overlap of the field profiles of the reverse and the developing measurements occurs on the increasing field branch.

To explain the late overlap in figure 6.8 in context of the critical state model, J^G should be (significantly) larger than 10^{11} A m $^{-2}$. A field profile with $J^G = 10^{11}$ A m $^{-2}$ is plotted in figure 6.9A for comparison at 0.3 T, which makes the inconsistency apparent.

The quantitative evaluations from the field profiles in figure 6.9 are displayed in figures 6.11A and 6.11B, where the corresponding contribution of J_c ($M_{\text{inter}}^{\text{SHPM}}$) and J^G ($M_{\text{intra}}^{\text{SHPM}}$) to the magnetization are plotted together with their combined value (lines), which reproduce the magnetization measured by a SQUID magnetometer (M^{SQUID}) very accurately. In figures 6.11C and 6.11D the evaluated values from the SHPM scans are used together with equation (4.21) to calculate J_c according to the presented model. The parameters in equation (4.21) are adopted from the fit to the data in figure 6.7 ($u = 3$, $s_0 = 1$ μm , $d = 2.7$ nm, $\lambda = 180$ nm, and $J_0 = 1.8$ A m $^{-2}$).

The behavior of $M_{\text{inter}}^{\text{SHPM}}$ and $M_{\text{intra}}^{\text{SHPM}}$ in the developing and reverse measurements is qualitatively the same on the increasing field branch (figure 6.11A). $M_{\text{inter}}^{\text{SHPM}}$ changes rapidly within the first 10 and 20 mT of the respective measurements. $M_{\text{intra}}^{\text{SHPM}}$ exhibits a similar behavior when H_{ext} increases, but the rate at which $M_{\text{intra}}^{\text{SHPM}}$ decreases is much slower. After their respective minimums, $M_{\text{inter}}^{\text{SHPM}}$ and $M_{\text{intra}}^{\text{SHPM}}$ increase slowly. Figure 6.11C shows, that the presented model describes data correctly at $\mu_0 H_{\text{ext}} \gtrsim 0.35$ T. At smaller H_{ext} , the model overestimates J_c by a factor 1.2.

The field dependence of $M_{\text{inter}}^{\text{SHPM}}$ and $M_{\text{intra}}^{\text{SHPM}}$ in the developing and reverse measurements on the decreasing field branch are slightly different compared to the increasing field branch, as shown in figures 6.11B and 6.12A. The rapid change of $M_{\text{inter}}^{\text{SHPM}}$, which is observed in the beginning of each measurement, occurs within 1 mT, which is indicated in figure 6.12A as region „1.“ This change is in agreement with the predictions of critical state model.

Besides this first increase the developing and reverse measurements behave differently. In the developing measurements, $M_{\text{inter}}^{\text{SHPM}}$ increases steadily while $M_{\text{intra}}^{\text{SHPM}}$ stays small and varies only slightly. This region is indicated in figure 6.12A by „3.“ The role of $M_{\text{inter}}^{\text{SHPM}}$ and $M_{\text{intra}}^{\text{SHPM}}$ is exchanged in the reverse measurements, i. e. $M_{\text{intra}}^{\text{SHPM}}$ increases slowly when H_{ext} is reduced while $M_{\text{inter}}^{\text{SHPM}}$ does not change (region „2“ in figure 6.12A). When $M_{\text{intra}}^{\text{SHPM}}$ approaches zero, $M_{\text{inter}}^{\text{SHPM}}$ and $M_{\text{intra}}^{\text{SHPM}}$ behave similar to the developing measurements, i. e. region 3: $M_{\text{inter}}^{\text{SHPM}}$ increases steadily while $M_{\text{intra}}^{\text{SHPM}}$ stays small.

In figure 6.11D, $M_{\text{inter}}^{\text{SHPM}}$ of the reverse measurement is not in agreement with the presented model, while it increases in accordance with the model in figure 6.12. The inconsistency between the model and the data in figure 6.11D is most likely a consequence of the large J_c near zero, so that the inter-grain field profile cannot develop fast enough. This is visible in figure 6.11B, where the slope of $M_{\text{inter}}^{\text{SHPM}}$ in the developing and reverse measurement is approximately the same in the range: $0.03 \leq \mu_0 H_{\text{ext}} < 0.1$ T. Thus, $M_{\text{inter}}^{\text{SHPM}}$ is only able to catch up with $M_{\text{inter}}^{\text{SHPM}}$

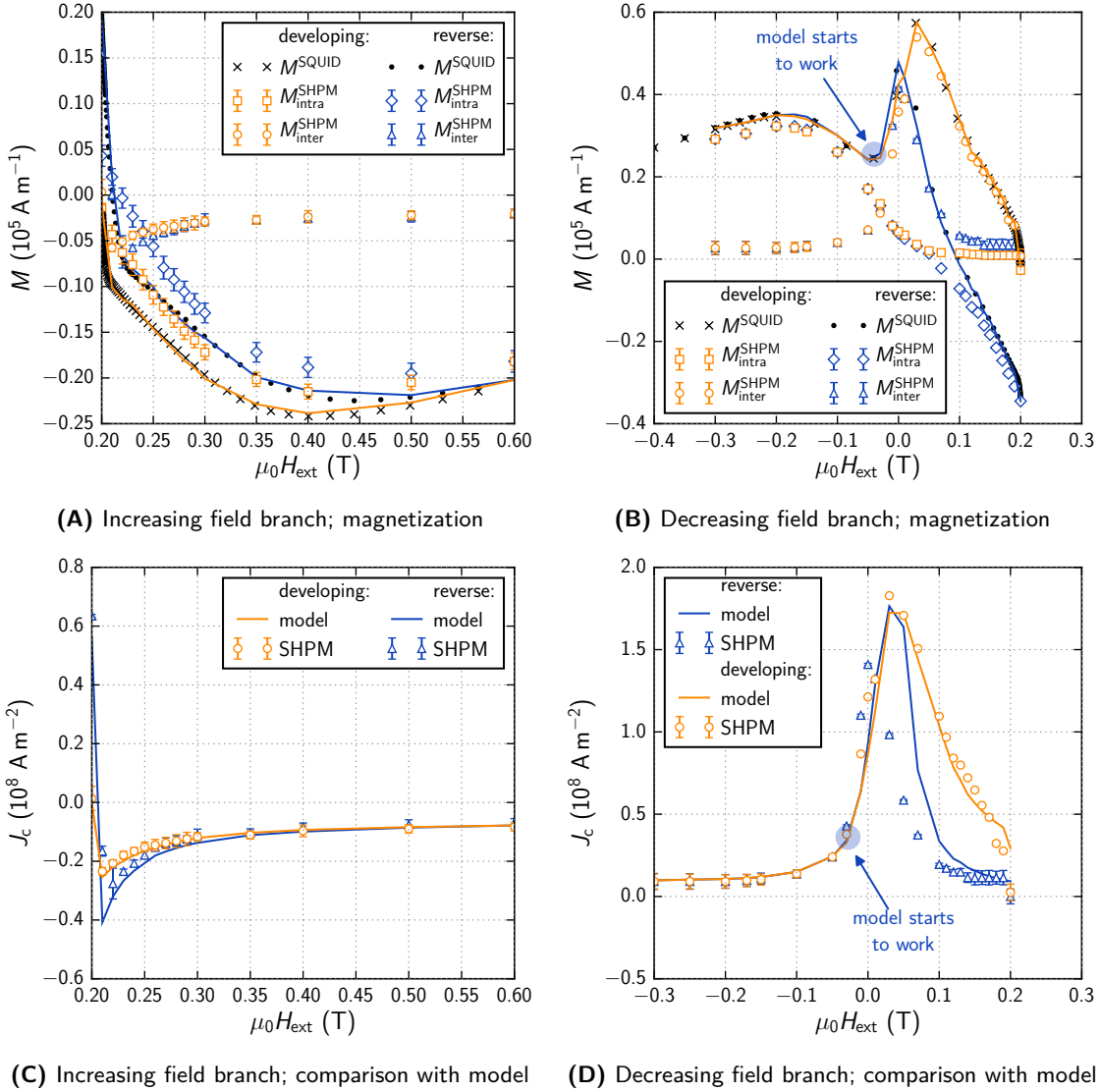


Figure 6.11: Magnetization corresponding to the inter- ($M_{\text{inter}}^{\text{SHPM}}$) and intra-grain currents ($M_{\text{intra}}^{\text{SHPM}}$) calculated from the fits to the field profiles measured by the scanning Hall-probe microscope (SHPM) in figure 6.9, and the results for inter-grain current density (J_c) according to equation (4.21), where the evaluated intra-grain current density from the SHPM measurements and the parameters from the fit in figure 6.7 (here, J_c has a sign to allow a comparison with the data from the SHPM). The lines in A and B represent $M_{\text{inter}}^{\text{SHPM}} + M_{\text{intra}}^{\text{SHPM}}$. The errors correspond to one standard deviation of the fits.

in the developing measurement on the increasing field branch, where J_c decreases. In contrast to figure 6.11D, the developing and the reverse measurement are in good agreement with the predictions of presented model in figure 6.12B. J_c is much smaller at larger fields ($\mu_0 H_{\text{ext}} > 0.2 \text{ T}$), so that the inter-grain field profile can adopt the aspired slope quickly.

Figures 6.9 to 6.12 show that H_1^* (and H_2^*) can be estimated from SHPM measurements of the field profile. In figure 6.13, these estimations are compared to the developing measurements presented in figure 6.8A. The vertical dotted lines indicate the fields at which the respective inter-grain field profiles of the various measurements saturate (H_1^*). The saturation occurs at

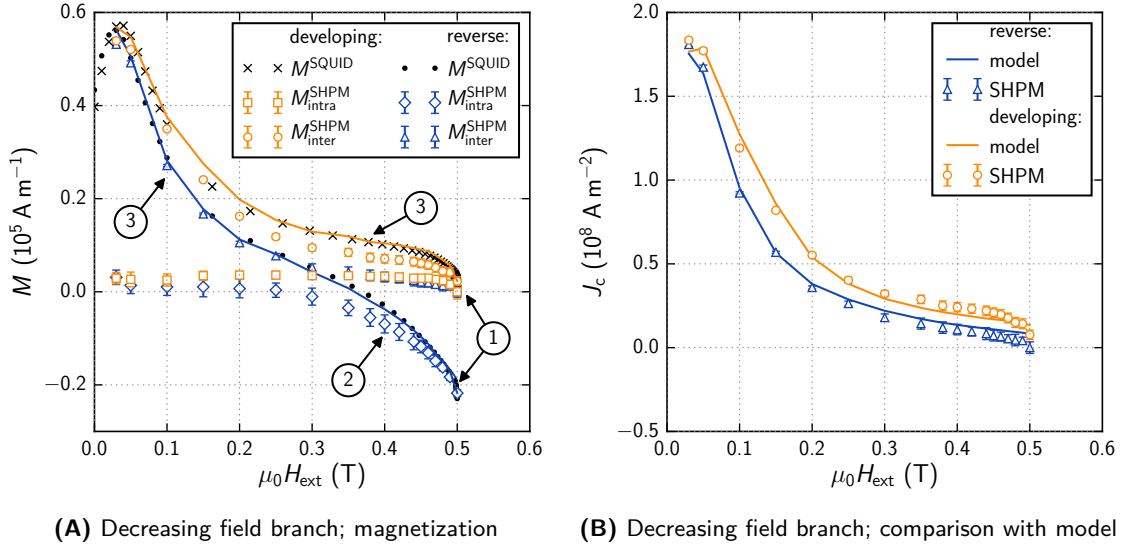


Figure 6.12: Similar to figures 6.11B and 6.11D. The measurements started at 0.5 T.

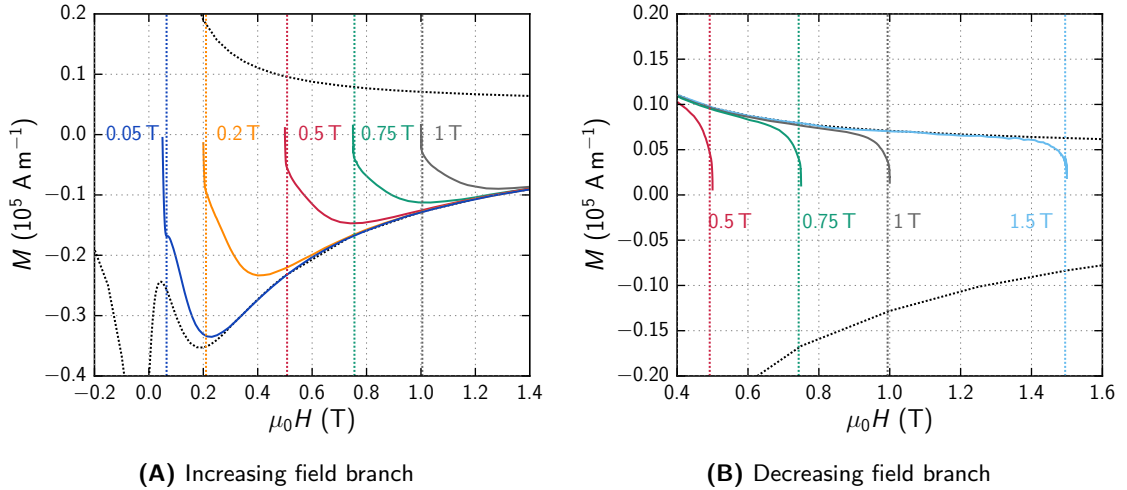


Figure 6.13: Same measurements as in figure 6.8, where the vertical dotted lines indicate the first penetration field (H_1^*) of the inter-grain field profile. H_1^* in the individual measurements were estimated from scanning Hall-probe microscope measurements.

the change in the slope of the magnetization curve on the increasing and decreasing field branch. The figure shows that J_c can be estimated from the developing magnetization curves in case of the medium grained sample and thus $J_c(H_{\text{ext}})$ can be determined by this way. This evaluated J_c as a function of H_{ext} can be used to simulate the behavior of the of the medium grained sample according to the critical state model, which can then be compared to the measured data.

The figures also show, that the determination of J^G from magnetization measurements, as discussed in section 2.2, is not possible, due to some unknown mechanism. Still, the presented model describes J_c very accurately despite the „strange“ behavior of J^G .

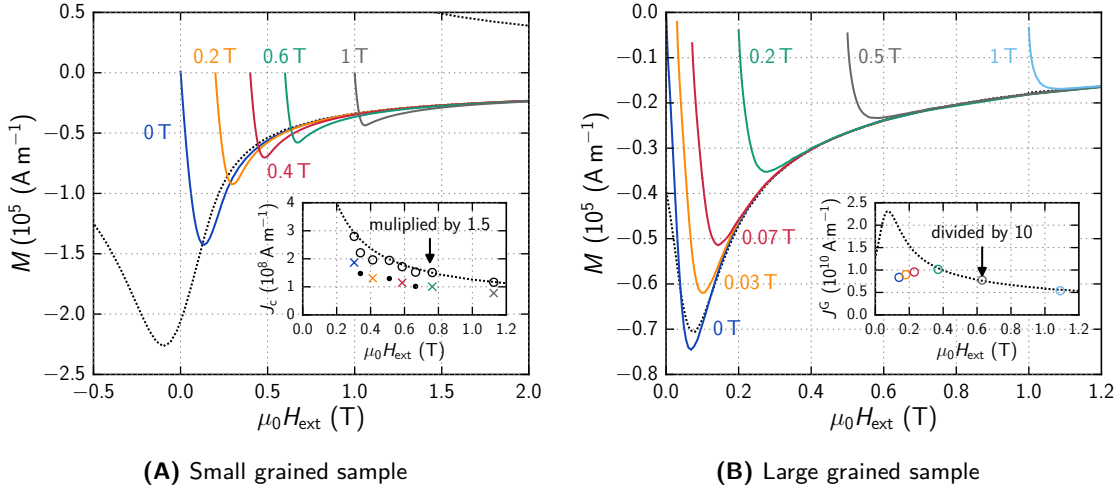


Figure 6.14: Magnetization measurements of a small ($3.47 \times 0.98 \times 0.50 \text{ m}^3$) and the large grained sample. The dotted line in the insets represent the J_c in A and representative intra-grain current density (J^G) in B. The „x“ in A are evaluations from the measurements in the main plot while the dots (\bullet) are evaluations from measurements that are not shown in the main plot. The circles (\circ) correspond to the same data multiplied by a certain factor.

6.2.3 Small and Large Grained Samples

In the small grained sample, M is mainly determined by the contributions of J_c , while J^G is dominant in the large grained sample. An attempt to estimate J_c from magnetization measurements is shown in figure 6.14A. The overlap between the various measurement with M_{sat} (dotted line) occurs at too large H_{add} , which would result in unreasonably large J_c , similar to the discussion of the medium grained sample. The magnetization curves after zero field cooling exceed M_{sat} , so that the peaks in M are clearly visible in the measurements. Thus, the field difference between H_{bg} and the peak position is used to estimate J_c with equation (2.11). The results are shown in the inset of figure 6.14A, where the dotted curve represents the evaluated J_c from M_{sat} (equation (2.5)). The inset shows that the peak position reflects J_c , therefore these measurements can be used to estimate J_c in the small grained sample. J_c was multiplied with the (arbitrary) factor 1.5 to emphasize the agreement of the peak position of M and J_c (circles in the inset).

The large grained sample also exhibits peaks in the measurements (figure 6.14B), but only the $H_{\text{bg}} = 0$ measurement has a peak that exceeds M_{sat} . The reason for this is most likely a noticeable contribution from J_c to the signal near zero field (cf. figure 6.5B). This contribution breaks down when the flux lines (FLs) penetrate the grains. Instead of the peak, the merging point with the magnetization loop of the saturated field profile is used to estimate J^G , where the influence of J_c is assumed to be negligible. Thus, the merging point should define the saturation of the intra-grain field profile, i. e. H_1^{*G} , with which J^G can be estimated by:

$$J^G \approx \frac{H_1^{*G}}{n^G s_0}, \quad (6.2)$$

where $n^G \approx 0.43$. The results are shown in the inset of figure 6.14B.

The calculated values of J^G are about a factor 10 larger than expected when the merging point of the magnetization measurements is used. A similar factor is found for J_c in the small grained sample if the merging point is utilized instead of the peaks. The measurements on the medium grained sample showed, that this behavior is rooted in the intra-grain field profile, which changes very slowly. Therefore, the late overlap of the magnetization measurements and M_{sat} in figure 6.14 is most likely a result of the same mechanism.

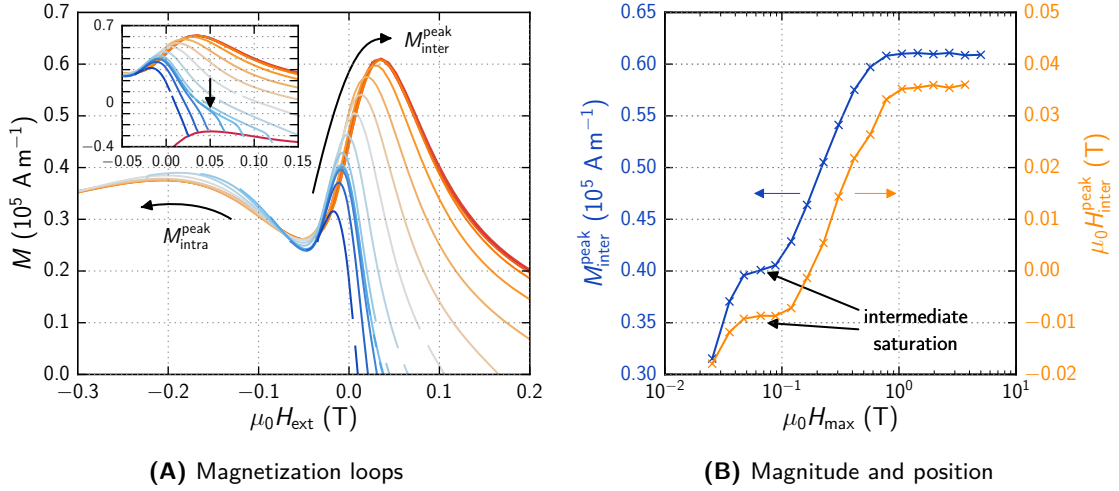


Figure 6.15: Dependence of the inter- ($M_{\text{inter}}^{\text{peak}}$) and intra-grain magnetization peak ($M_{\text{intra}}^{\text{peak}}$) on the maximum applied field (H^{max}). The development of $M_{\text{inter}}^{\text{peak}}$ and the shift from the increasing to the decreasing field branch ($H_{\text{inter}}^{\text{peak}}$) with increasing H^{max} are displayed in B.

6.3 Residual Field Profile

The motivation for the use of the residual field profile to separate J_c and J^G is the assumption that the inter-grain field profile saturates before the intra-grain field profile in weakly linked HTSs, because $J_c < J^G$. The residual field profile refers to the magnetic response of a sample at a certain field as a function of H^{max} , i. e. the sample is cooled below T_c at H_{bg} , then the field is ramped to H^{max} and back to H_{bg} . Such field cycles are repeated several times, where H^{max} is increased for consecutive measurements. In order to saturate the residual inter-grain field profile, the maximum additional applied field ($H_{\text{add}}^{\text{max}} = H^{\text{max}} - H_{\text{bg}}$) has to be equal to H_2^* or larger. The saturation process of the intra-grain field profile is more sophisticated (cf. section 3.2).

This section will show that the standard interpretation of residual magnetization (M_{res}) measurements, i. e. the separability of the inter- and intra-grain signals [Mul94; Eis10], is not possible in the case of the investigated samples. Instead, the measurement of the residual field profile is used to visualize a transition from the physics of the extended critical state model to a mechanism governed by coupled Josephson junctions (JJs) as discussed in chapter 4.

6.3.1 Magnetization Loops

Figure 6.15 displays the dependence of M of the medium grained sample on H^{max} . H_{ext} was ramped from positive to negative fields, where the value of H^{max} was increased for consecutive measurements. The measurements trace the evolution of the magnetization curves and of the two peaks that are present in this sample. The peak related to J_c ($M_{\text{inter}}^{\text{peak}}$) is referred to as the inter-peak. The other peak, which is referred to as the intra-peak, originates from J^G ($M_{\text{intra}}^{\text{peak}}$).

$M_{\text{intra}}^{\text{peak}}$ is shifted to negative fields, while $M_{\text{inter}}^{\text{peak}}$ moves from the increasing to the decreasing field branch, as indicated by the arrows in figure 6.15A. The evolution of $M_{\text{inter}}^{\text{peak}}$ and the simultaneous shift on the field axis ($H_{\text{inter}}^{\text{peak}}$) are plotted in figure 6.15B. $M_{\text{inter}}^{\text{peak}}$ increases with H^{max} and saturates at $\mu_0 H^{\text{max}} \approx 0.05$ T. This first saturation is referred to as intermediate saturation.

The three magnetization loops, that correlate with the intermediate saturation are indicated by the arrow in the inset of figure 6.15A. The field dependence of M changes significantly in these measurements. Only one slope (i. e. dM/dH) can be observed in the curves before the intermediate saturation, whereas three slopes can be distinguished in the measurements where

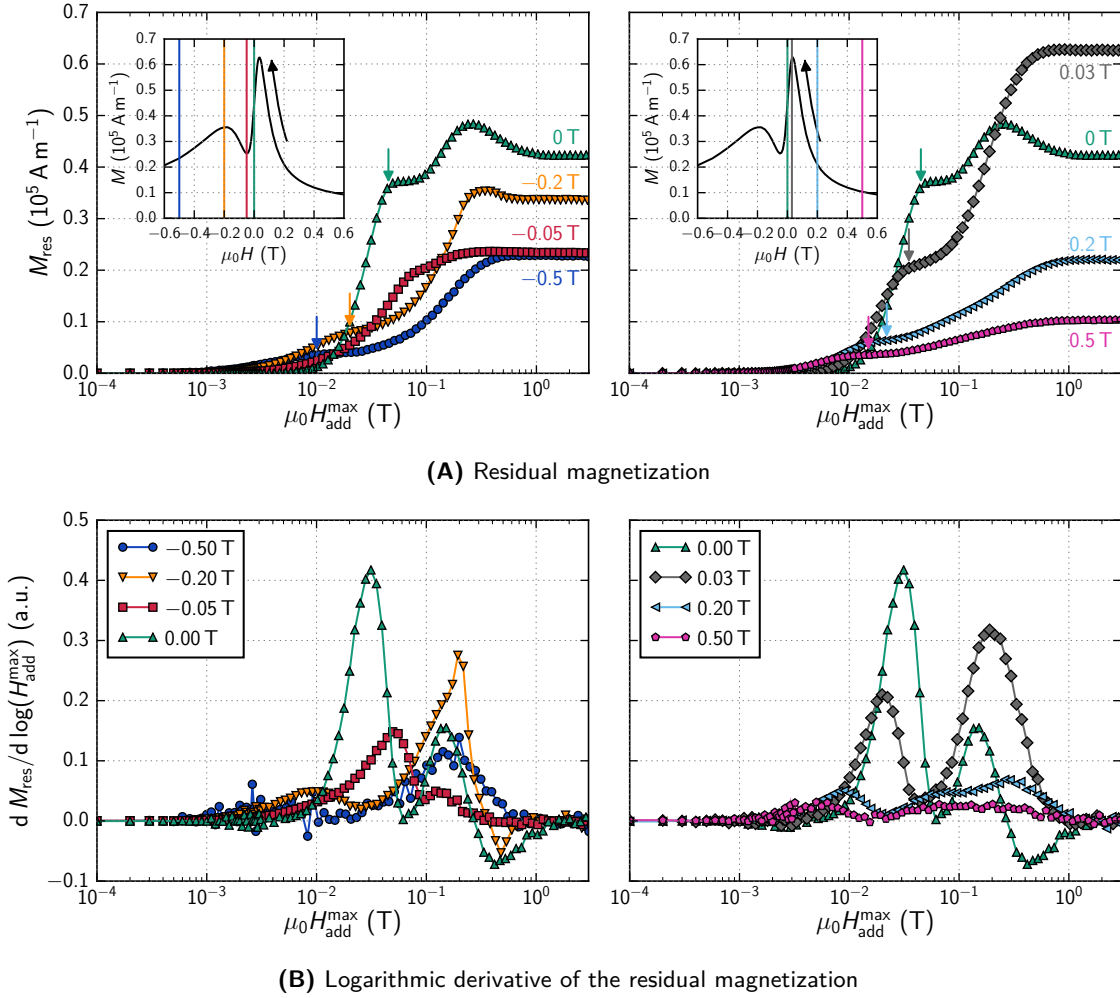


Figure 6.16: Residual magnetization (M_{res}) at various background fields (H_{bg}) as a function of the maximum additional applied field ($H_{\text{add}}^{\text{max}}$), as well as the logarithmic derivative of M_{res} , measured at 5 K. The respective H_{bg} of a measurement is given by the labels, the legends and the insets in A.

$M_{\text{inter}}^{\text{peak}}$ saturates for the first time. These regions have been discussed in context of figure 6.12. The curves at smaller H^{max} are described by the critical state model (cf. figure 2.5). Thus, the intermediate saturation is a result of the transition from the behavior according to the critical state model to the presented model. At $\mu_0 H^{\text{max}} > 0.1$ T, $M_{\text{inter}}^{\text{peak}}$ increases further and saturates at $\mu_0 H^{\text{max}} \approx 1$ T, which is referred to as final saturation. A similar dependence on H^{max} is found for $H_{\text{inter}}^{\text{peak}}$, which is plotted as a second axis in figure 6.15B. The intermediate and the final saturation of both curves occur at the same H^{max} .

6.3.2 Residual Magnetization

Figure 6.16 shows measurements of M_{res} obtained from the medium grained sample at different H_{bg} . In figure 6.16A, M_{res} is displayed as a function of $H_{\text{add}}^{\text{max}}$, where the insets indicate the different H_{bg} on a magnetization loop and figure 6.16B shows the logarithmic derivative of M_{res} . The corresponding SHPM scans for $\mu_0 H_{\text{bg}} = 0.03, 0,$ and -0.2 T are plotted in figure 6.17 (-0.17 T correlates with -0.2 T).

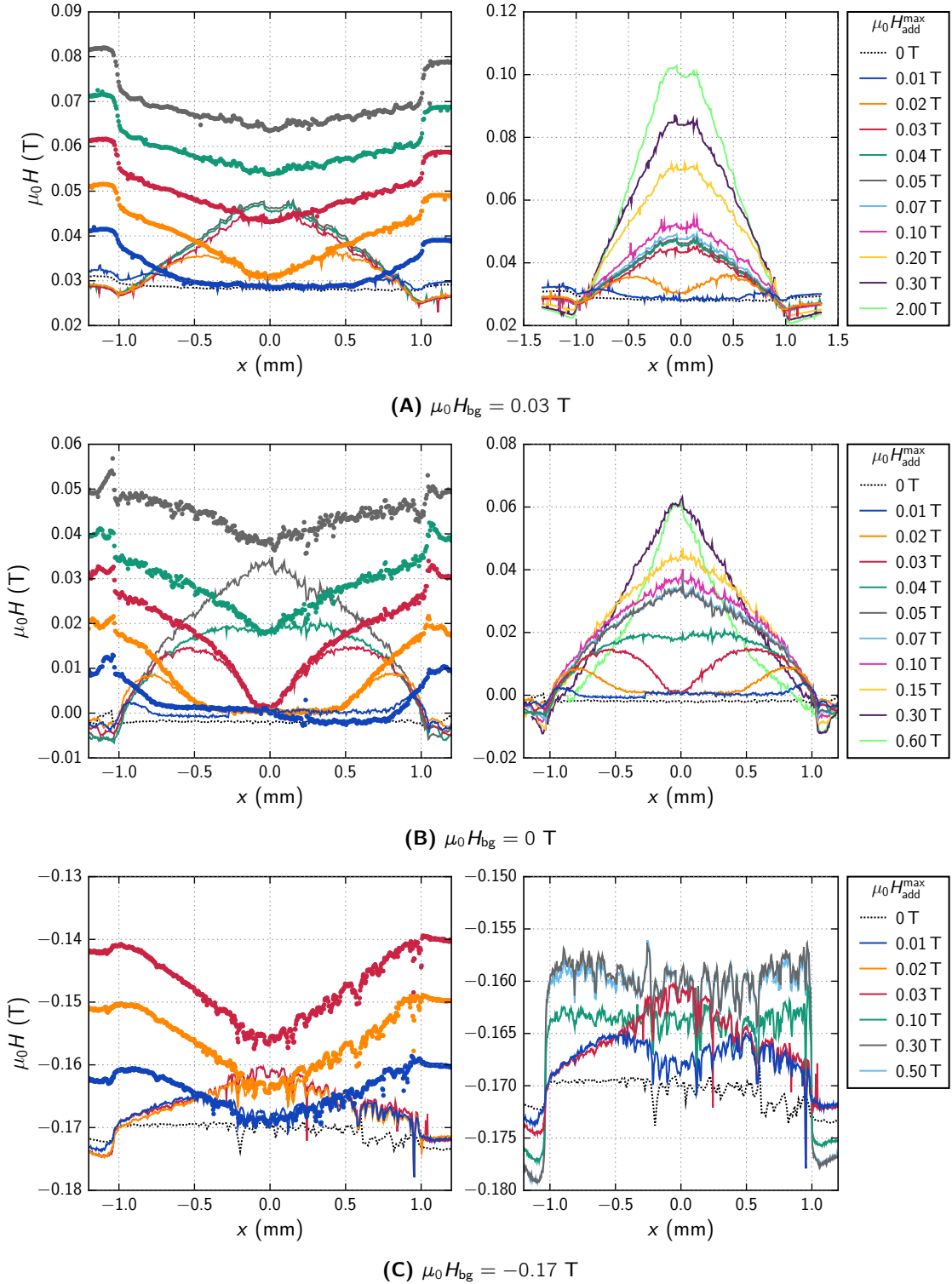


Figure 6.17: Evolution of the residual field profile of the medium grained sample at three different background fields (H_{bg}). The temperature was 5 K and the distance between the Hall-probe and the surface was 1 to 5 μm . The left figures show the field profiles at the maximum additional applied field (H_{add}^{max}) and the corresponding residual state (represented by dots and lines of the same color). In the right figures only the residual field profiles are plotted.

The residual field profile at 0.03 T is displayed in figure 6.17A, which is the field where the maximum J_c is located on a magnetization loop from 7 to -7 T. The scans were slightly off-center in y -direction, so that the field profiles exhibit a plateau region near the middle of the line scans. All measurements, that were carried out at $H_{\text{add}}^{\text{max}}$, are located on the increasing field branch, while the residual field profiles are on the decreasing field branch. The intermediate saturation of the residual inter-grain field profile is observed for $\mu_0 H_{\text{add}}^{\text{max}} \approx 0.04$ T, which correlates to the scans where the field profile at $H_{\text{add}}^{\text{max}}$ has no overlap with the subsequent scan at H_{bg} for the first time in figure 6.17A. The correlation between the intermediate saturation of M_{res} and the first separation of the field profiles at $H_{\text{add}}^{\text{max}}$ and H_{bg} is visualized in figure 6.16A as well. The arrows in the figure indicate the $H_{\text{add}}^{\text{max}}$ where the field profiles separate,* which is the definition of H_2^* in the extended critical state model. These values correspond to the onset of the intermediate saturation. The residual field profile does not change significantly in the interval: $0.04 \lesssim \mu_0 H_{\text{add}}^{\text{max}} < 0.1$ T, but the global slope increases again and finally saturates at $\mu_0 H_{\text{add}}^{\text{max}} \approx 1$ T. The field profiles in figure 6.17A have a more or less constant field gradient, which is not expected because J_c should vary considerably near the peak.

A more complex behavior of the inter-grain field profile is observed in figure 6.17B, where the slope changes from a concave to a convex shape with increasing $H_{\text{add}}^{\text{max}}$. The maximum M_{res} in figure 6.16A coincides with the residual field profile in figure 6.17B, where the global slope is approximately linear ($\mu_0 H_{\text{add}}^{\text{max}} = 0.3$ T). The transition from a concave to a convex inter-grain field profile can be qualitatively explained by the field dependence of J_c . The concave shape results from the rapid decrease of J_c with increasing field when the field profile is located on the right side of the inter-peak. Therefore, J_c is large at the sample edges and small at the center. With increasing $H_{\text{add}}^{\text{max}}$, the inter-peak is shifted to higher fields (cf. figure 6.15). Now the measurements are located on the other side of the peak, i. e. J_c is small at the sample edges and large at the center, which results in the convex shape. With this transition the inter-grain contribution to M_{res} decreases while the intra-grain contribution increases.

The measurements in figure 6.17C ($\mu_0 H_{\text{bg}} = -0.17$ T) show the emergence of an inter-grain field profile up to $\mu_0 H_{\text{add}}^{\text{max}} \approx 0.03$ T. After this field the slope of the inter-grain field profile decreases gradually and becomes flat in the $\mu_0 H_{\text{add}}^{\text{max}} = 0.1$ T measurement.

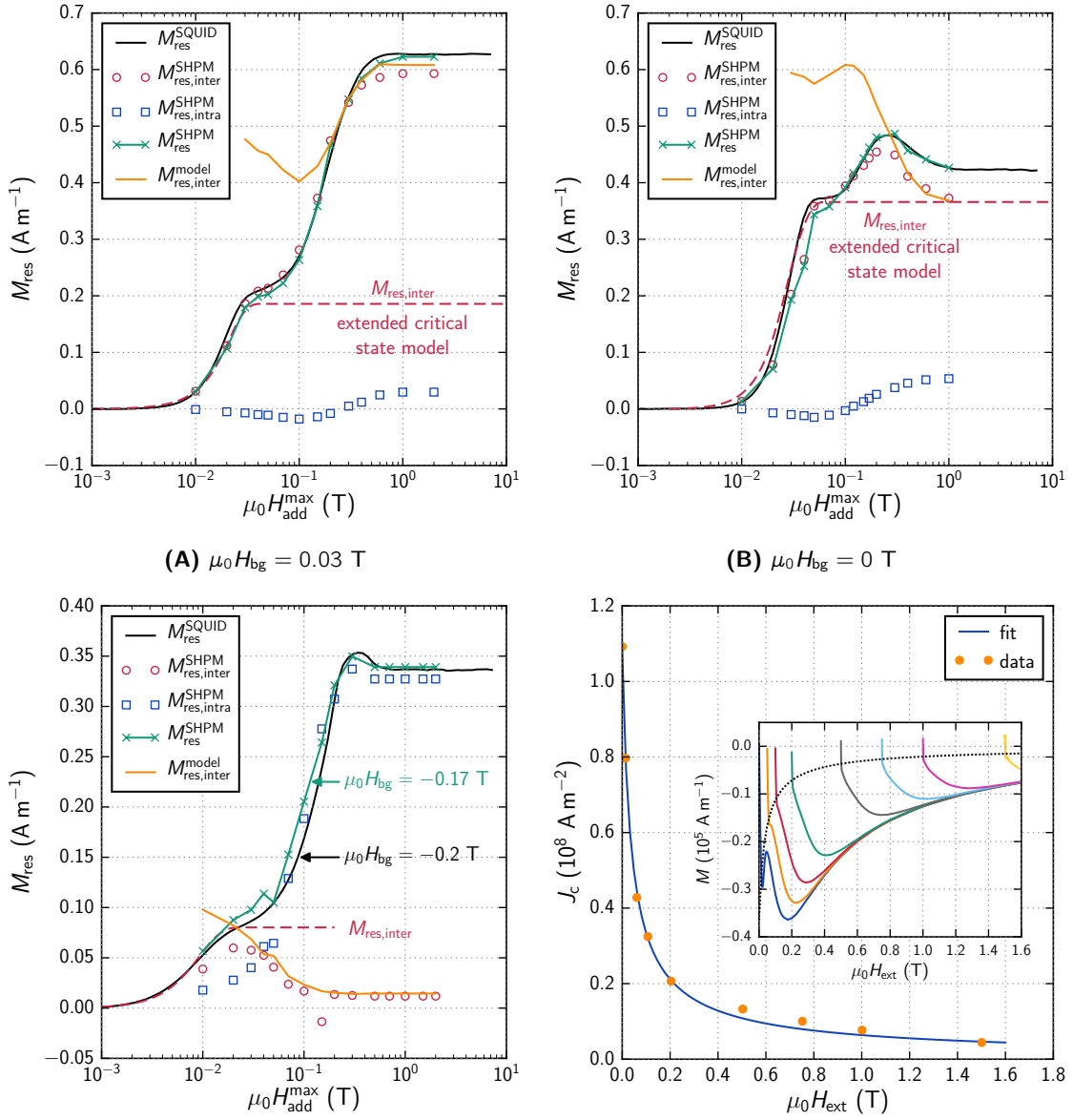
The comparison between the evaluated inter- ($M_{\text{res,inter}}^{\text{SHPM}}$) and intra-grain ($M_{\text{res,intra}}^{\text{SHPM}}$) contributions from figure 6.17 and the corresponding M_{res} from figure 6.16A is presented in figures 6.18A to 6.18C.† Figure 6.18D shows the field dependence of J_c evaluated from magnetization loops such as those in figure 6.14, i. e. the sample was cooled below T_c at different H_{bg} and H_{ext} was increased subsequently. The inset in figure 6.18D display the utilized magnetization loops. The intersection of the magnetization curves and the dotted line indicates the points that were used to calculate the data in the main panel. The fit to these points was then utilized to calculate $M_{\text{res,inter}}$ according to the extended critical state model in the other plots (dashed curves). $M_{\text{res,inter}}^{\text{model}}$ simulates the expected residual magnetization originating from J_c of the inter-grain field profile according to the presented model.

The intermediate saturation in M_{res} can be observed in all measurements, except in the -0.05 T. On the decreasing field branch, this saturation can be associated with the inter-grain field profile, because the contribution of J^G to the field profiles is small in the 0 and 0.03 T measurements, but in figure 6.18C the intermediate saturation is a result of the simultaneous decrease of J_c and increase of J^G .

$M_{\text{res,intra}}^{\text{SHPM}}$ exhibits a peak in figure 6.18C, that is hardly visible in figure 6.17 but a corresponding behavior is observed in M_{res} . The contribution of J^G to the residual field profile is small compared to J_c in figures 6.18A and 6.18B, while the contribution of J^G is large compared to J_c in figure 6.18C. This is most likely the reason why M_{res} according to the critical state model shows the worst agreement in this figure, while the match of $M_{\text{res,inter}}^{\text{SHPM}}$ and $M_{\text{res,inter}}^{\text{model}}$ occurs at smaller $H_{\text{add}}^{\text{max}}$ compared to the 0 and 0.03 T measurements.

* No SHPM scans were carried out for the $\mu_0 H_{\text{bg}} = -0.05$ T measurement. Therefore, the arrow is missing.

† No data is available for $\mu_0 H_{\text{add}}^{\text{max}} > 1$ T in figure 6.18B, due to problems with the Hall-probe.



(C) $\mu_0 H_{bg} = -0.17$ T (SHPM) and -0.2 T (SQUID) (D) Fit of $J_c(H_{ext})$ to developing magnetization curves

Figure 6.18: Data of the residual magnetization (M_{res}) from figure 6.16 and the inter- ($M_{res,inter}^{SHPM}$) and intra-grain contribution ($M_{res,intra}^{SHPM}$), which were evaluated from the scanning Hall-probe microscope (SHPM) measurements in figure 6.17 for selected background fields (H_{bg}). M_{res}^{SHPM} represent their combined value. The curve labeled $M_{res,inter}^{model}$ denotes the expected residual magnetization according to the presented model, where the evaluated representative intra-grain current density (J_c^G) from the SHPM measurements was used in equation (4.21) to calculate the inter-grain current density (J_c). The dashed curves show the expected residual magnetization originating from J_c ($M_{res,inter}$) according to the extended critical state model, where the field dependence of J_c was determined by fitting the evaluated current densities from developing magnetization curves.

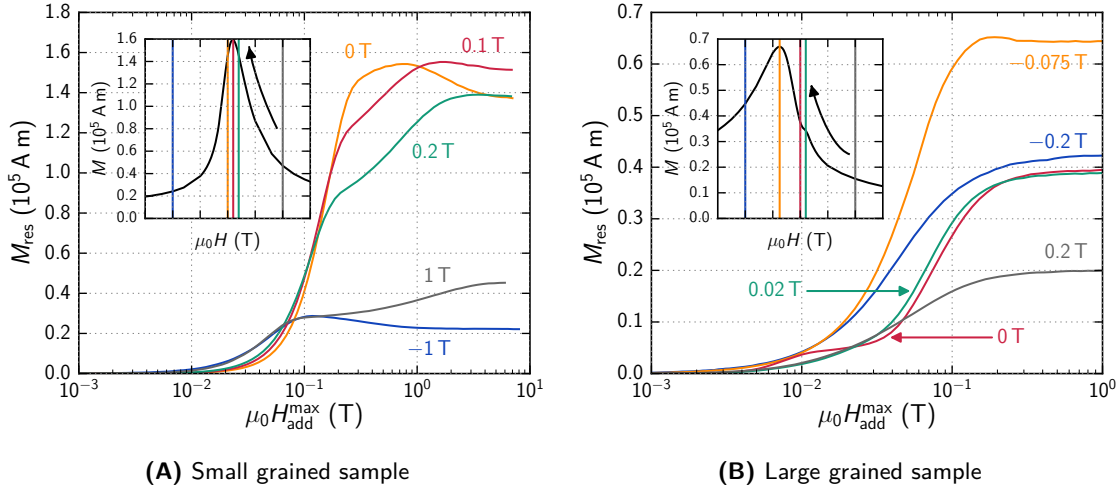


Figure 6.19: Residual magnetization (M_{res}) of the small (geometry: $3.90 \times 0.68 \times 0.47 \text{ mm}^3$) and large grained sample as a function of the maximum additional applied field ($H_{\text{add}}^{\text{max}}$). The background fields in which the samples were cooled are written next to the curves and are indicated in the insets, where a magnetization loop from 7 to -7 T is displayed for the respective sample.

All M_{res} measurements in figure 6.18 have a certain field range where either the critical state model or the presented model describe $M_{\text{res,inter}}^{\text{SHPM}}$ better. In the $\mu_0 H_{\text{bg}} = 0.03 \text{ T}$ measurement, $M_{\text{res,inter}}^{\text{SHPM}}$ increases after the intermediate saturation whereas $M_{\text{res,inter}}^{\text{SHPM}}$ increases at first and then decreases in figure 6.18B. Thereby, the peak position correlates with the first noticeable increase of $M_{\text{res,intra}}^{\text{SHPM}}$. $M_{\text{res,inter}}^{\text{SHPM}}$ does not reach the intermediate saturation in figure 6.18C, which is most likely the result of the large $M_{\text{res,intra}}^{\text{SHPM}}$. The evolution of $M_{\text{res,inter}}^{\text{SHPM}}$ and the simulated $M_{\text{res,inter}}$ according to the critical state model match at small $H_{\text{add}}^{\text{max}}$ in figures 6.18A and 6.18B, which indicates that well known mechanisms describe the SC in this region, while $M_{\text{res,inter}}^{\text{SHPM}}$ and $M_{\text{res,inter}}^{\text{model}}$ match at high $H_{\text{add}}^{\text{max}}$, indicating that the presented model becomes the determining mechanism.

A comparison between figures 6.15 and 6.18B shows that the extended critical state model works as long as only one slope is visible in the magnetization loops in figure 6.15, i. e. $\mu_0 H^{\text{max}} \lesssim 0.5 \text{ T}$. At larger H^{max} , three regions can be distinguished (cf. figure 6.12; reverse measurement), which are indicative for the presented model.

The development of $M_{\text{res,intra}}^{\text{SHPM}}$ exhibits qualitatively the same behavior as the modeled residual magnetization originating from all irreversible contributions of the grains ($M_{\text{res,irr}}^{\text{G}}$) in section 3.2.2, i. e. the signal becomes negative at small $H_{\text{add}}^{\text{max}}$ before it becomes positive, but a simulation of $M_{\text{res,irr}}^{\text{G}}$ showed that the development of $M_{\text{res,irr}}^{\text{G}}$ proceeds too slowly.

Figure 6.18 show that the observations made in the developing and reverse field profiles are also made in the residual field profiles, i. e. a good agreement between the presented model and the measurements for large $H_{\text{add}}^{\text{max}}$ despite the „strange“ behavior of J^{G} .

6.3.3 Small and Large Grained Samples

The observations of an intermediate saturation in M_{res} , i. e. the double step behavior, and a decrease of M_{res} before the final saturation of M_{res} in some measurements, are made in the small and large grained samples as well. The contribution of J^{G} to the total magnetic response is comparatively small in the small grained sample. Thus, the measurements in figure 6.19A mainly represent the behavior of the inter-grain field profile. The contribution of J^{G} is dominant in the large grained sample, so that the measurements represent the behavior of the intra-grain field profile.

The curves in figure 6.19A show qualitatively the same behavior as $M_{\text{res,inter}}^{\text{SHPM}}$ in figure 6.18D, i. e. the double step in the measurements at the right side of the peak and the decrease at large $H_{\text{add}}^{\text{max}}$ on the left side of the peak. The measurements in figure 6.19B resemble the $M_{\text{res,intra}}^{\text{SHPM}}$ curves in figure 6.18D, except for the 0 T measurement, where the double step is present.

The comparison of M_{res} of all grain sizes shows that a smaller grain size increases the field range where the decrease of $M_{\text{res,inter}}^{\text{SHPM}}$ at high $H_{\text{add}}^{\text{max}}$ is observable. For instance, the decrease is still present in the -1 T measurement of the small grained sample, whereas it is no longer observed in the -0.5 T measurement of the medium grained sample. The decrease in the -0.075 T measurement of large grained sample is related to $M_{\text{res,intra}}^{\text{SHPM}}$.

6.4 Behavior of the Intra-Grain Current Density

The presented model (equation (4.21)) describes J_c accurately with the experimentally determined values of J^G . Although the measured J_c and J^G correspond to the presented model, the behavior of J^G by itself is surprising. The change of J^G after the reversal of the field ramp and after H_{ext} crossed zero proceeds about an order of magnitude slower than expected. Furthermore, J^G is small and approximately constant on the decreasing field branch, and this constant value is influenced by the magnetic history, i. e. J^G is larger when the sample was cooled in a high field and then ramped to zero, than when the field ramp was reversed at the same field and then ramped to zero.

A theoretical description of J^G is not part of this thesis. Nonetheless, the slow change of J^G indicates the presence of a mechanism, that prevents FLs from entering and exiting the grains or requires J^G to adopt a certain value.

The presented model reduces the description of the GB network in a polycrystal by integration of the DC Josephson current density over the grain size distribution which results in an analytical function, where the individual parameters are average values that characterize the sample. This function is derived without restrictions for the phase, however, the GBs form a JJ network in a weakly linked polycrystalline SC that shares one global current (J_c), which forces the phases of the individual JJs to be coupled. Thus, the development of the field profile depends on the restrictions that are imposed by the (shared) phase of the system, which may limit the maximal possible change of J^G (and J_c), that would have to be taken into account in the integration.

The presented model used the macroscopic parameter J_c and an averaged J^G to describe the JJ network. From a microscopic point of view, the polycrystal is penetrated with FLs which are either located at a GB or inside a grain. The FL distribution at the GBs relates to J_c while the FLs in the grains describe J^G . In equilibrium the FLs at the GBs and inside the grains are distributed in such a way that the „optimal“ phase is present in the sample. The change of H_{ext} necessitates the redistribution of the FLs, which can only happen without the violation of the global phase relations. The repositioning of the FL change the FL distribution locally. In a system with no global phase relation the FLs can redistribute without restrictions. A weakly linked polycrystalline SC has to manage the global distribution of the FLs in accordance with the global phase and as a result the repositioning of the FL may be inhibited, so that the change of J^G and J_c requires more time than in isolated grains.

6.5 Neutron Irradiation

Figure 6.20 displays the impact of fast neutron irradiation on the magnetic response of a small grained K doped Ba-122 polycrystal. Fast neutrons induce defects in the SC as a result of the collisions of high energy neutrons with lattice atoms. These additional defects increase pinning inside the grains and thereby J_{irr}^G .

The magnetization loops in figure 6.20A show that $|M|$ at the peak position decreases with increasing fluence ($\Phi\Delta t$) and its position is shifted to higher fields on the decreasing field branch.

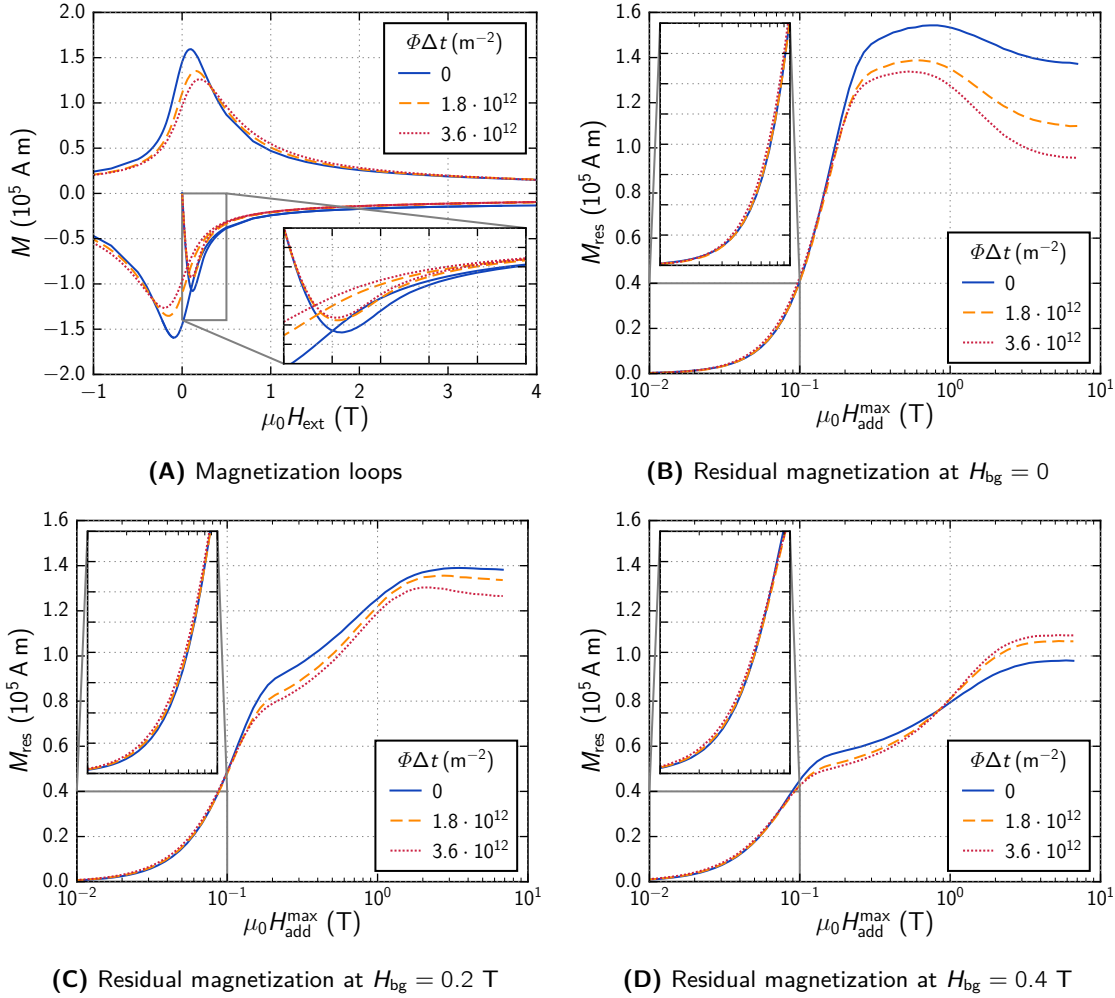


Figure 6.20: Magnetization loops (A) and measurements of the residual magnetization (M_{res}) at various background fields (H_{bg}) of a small grained K doped Ba-122 sample ($3.90 \times 0.68 \times 0.47$ mm³) before and after exposing it to different fast neutron fluences ($\Phi\Delta t$). The measurements were carried out at 5 K.

The magnetic signal is reduced on the entire increasing field branch, while it is more or less unchanged on the decreasing field branch for $\mu_0|H_{ext}| > 2$ T after neutron irradiation. M increases with rising fluence between 0.5 and 2 T.

The shift of the peak is a result of the increased pinning, which causes the peak to appear at higher $|H_{ext}|$. The magnitude of this shift is remarkable. The peak occurs at 0.1 T in the pristine state and increases to 0.15 and finally 0.2 T after the respective irradiation steps. This shift of the peak from approximately 0.1 to 0.2 T corresponds to an increase of J^G by a factor 2 according to the presented model, i. e. $J^G \approx 6 \cdot 10^9$ A m⁻² on the decreasing field branch.

The smaller signal on the increasing field branch and the larger signal on the decreasing field branch are expected by the presented model, but the decrease of M at the peak position is unexpected. Thereby, the peak has about 80% of its initial height after the last irradiation step, which is much more than the expected degeneration of the sample with time (about 3% in this case). The decrease could be caused by an accumulation of the newly induced defects at the GBs. These additional defects increase the tunneling barrier and thereby decrease J_{c0} .

Figures 6.20B to 6.20D display a comparison of M_{res} between the different irradiation steps. The observed behavior is similar to the one found in the medium grained sample, i. e. the double step and the decrease of M_{res} at high $H_{\text{add}}^{\text{max}}$. The dependence of M_{res} on $H_{\text{add}}^{\text{max}}$ is approximately the same at small $H_{\text{add}}^{\text{max}}$ (see insets) but the curves split at about 0.1 T. The splitting of the curves is caused by the shift of the magnetization curve, the decrease of the peak, and the increase of M at higher fields due to pinning.

No clear double step is visible in figure 6.20B. This is mainly an effect of the stronger decrease of M_{res} at higher $H_{\text{add}}^{\text{max}}$ after the neutron irradiation, i. e. the peak shift and the smaller magnitude of the peak. The data in figure 6.20C exhibit the double step behavior, where the magnitude of the first step decreases, while the second step becomes larger with increasing fluence. At the end of the measurements the decrease of M_{res} is still present. The M_{res} curves are smaller after each irradiation step in figures 6.20B and 6.20C. This changes in figure 6.20D, where M_{res} saturates at larger values. The decrease vanishes at this H_{bg} so that only the double step behavior remains. The first step becomes smaller and the second step larger with increasing fluence.

This result confirms the predictions of the model that a smaller value of J^{G} increase J_{c} on the increasing field branch, therefore the pinning in polycrystalline HTS with large angle GBs should be (reasonably) small.

6.6 Summary

The current transport mechanisms in polycrystalline Co and K doped BaFe_2As_2 bulks were investigated, with special emphasis on the dependence of J_{c} on the grain size.

A hysteresis of J_{c} was observed in the samples, which has been reported for other HTSs as well, i. e. J_{c} is larger on the decreasing field branch than on the increasing field branch. The commonly accepted explanation for this J_{c} hysteresis is based on the field arising from J^{G} , which leads to a reversed field component at the GBs. However, the J^{G} necessary to explain the behavior in the investigated samples was found to be unreasonably large.

Measurements on Co and K doped BaFe_2As_2 with three different grain sizes revealed that the hysteresis of J_{c} becomes larger when the grains are smaller and that the maximum J_{c} is found in the samples with the smallest grains. These observations are independent of the dopant and the temperature.

The samples were examined by magnetization measurements and a SHPM to determine the origin of this effect. J_{c} and J^{G} can be obtained from SHPM measurements, where J_{c} corresponds to a global field gradient, while the field gradients generated by J^{G} are localized at the sample edges. The data from magnetometer devices and the SHPM were found to be in good agreement.

J_{c} and J^{G} , evaluated from the SHPM measurements, were used to check the validity of the analytical function derived in chapter 4, which is based on the equations of a JJ and the statistical variation of the grain size. This model was fitted to the data from the SHPM to get values for the parameters in the function. These values were found to be in good agreement with those in the literature. Further measurements were conducted to validate the applicability and consistency of the model, i. e. after the reversal of H_{ext} at a certain field and after field cooling. Again the data and the model were in good agreement.

Special measurements were performed to study the development of J_{c} and J^{G} after cooling below the superconducting transition temperature and then applying an additional field and subsequently reducing it to its initial value. These measurements indicated a transition of the well known behavior according to the Bean model, which describes the field profiles after small field changes, to a mechanism that is governed by JJs, i. e. the presented model, after large field changes.

Neutron irradiation experiments were conducted in order to enhance the pinning within the grains. The resulting changes after the irradiation allowed the qualitative confirmation of models and its predictions.

References

- [Dau92] M. Däumling, E. Sarnelli, P. Chaudhari, A. Gupta, and J. Lacey (1992): „Critical current of a high- T_c Josephson grain boundary junction in high magnetic field“ *Appl. Phys. Lett.* **61**, 1355.
- [Eis10] M. Eisterer, M. Zehetmayer, H. W. Weber, J. Jiang, J. D. Weiss, A. Yamamoto, E. E. Hellstrom, D. C. Larbalestier, N. D. Zhigadlo, and J. Karpinski (2010): „Disorder effects and current percolation in FeAs-based superconductors“ *Supercond. Sci. Technol.* **23**, 054006.
- [Eve88] J. E. Evetts and B. A. Glowacki (1988): „Relation of critical current irreversibility to trapped flux and microstructure in polycrystalline $\text{YBa}_2\text{Cu}_3\text{O}_7$ “ *Cryogenics* **28**, 641.
- [Kih13] K. J. Kihlstrom, L. Fang, Y. Jia, B. Shen, A. E. Koshelev, U. Welp, G. W. Crabtree, W.-K. Kwok, A. Kayani, S. F. Zhu, and H.-H. Wen (2013): „High-field critical current enhancement by irradiation induced correlated and random defects in $(\text{Ba}_{0.6}\text{K}_{0.4})\text{Fe}_2\text{As}_2$ “ *Appl. Phys. Lett.* **103**, 202601.
- [Kim14] Y. Kim, J. D. Weiss, E. E. Hellstrom, D. C. Larbalestier, and David N. Seidman (2014): „Evidence for composition variations and impurity segregation at grain boundaries in high current-density polycrystalline K- and Co-doped BaFe_2As_2 superconductors“ *Appl. Phys. Lett.* **105**.
- [Kun98] M. N. Kunchur and T. R. Askew (1998): „Hysteretic internal fields and critical currents in polycrystalline superconductors“ *J. Appl. Phys.* **84**, 6763.
- [Kuw89] M. Kuwabara and H. Shimooka (1989): „Grain size dependence of the critical current density in $\text{YBa}_2\text{Cu}_3\text{O}_x$ superconductors“ *Appl. Phys. Lett.* **55**, 2781.
- [Li08] G. Li, W. Z. Hu, J. Dong, Z. Li, P. Zheng, G. F. Chen, J. L. Luo, and N. L. Wang (2008): „Probing the Superconducting Energy Gap from Infrared Spectroscopy on a $\text{Ba}_{0.6}\text{K}_{0.4}\text{Fe}_2\text{As}_2$ Single Crystal with $T_c = 37$ K“ *Phys. Rev. Lett.* **101**, 107004.
- [Lis97] F. A. List, D. M. Kroeger, and V. Selvamanickam (1997): „Hysteresis of the transport critical current of (Tl,Pb)-(Sr,Ba)-Ca-Cu-O and Bi-Sr-Ca-Cu-O conductors: effects of temperature and magnetic field“ *Physica C* **275**, 220.
- [McH89] M. E. McHenry, M. P. Maley, and J. O. Willis (1989): „Systematics of transport critical-current-density hysteresis in polycrystalline Y-Ba-Cu-O“ *Phys. Rev. B* **40**, 2666.
- [Mul94] K.-H. Müller, C. Andrikidis, H. K. Liu, and S. X. Dou (1994): „Intergranular and intragranular critical currents in silver-sheathed Pb-Bi-Sr-Ca-Cu-O tapes“ *Phys. Rev. B* **50**, 10218.
- [Pal07] A. Palau, T. Puig, X. Obradors, and Ch. Jooss (2007): „Simultaneous determination of grain and grain-boundary critical currents in $\text{YBa}_2\text{Cu}_3\text{O}_7$ -coated conductors by magnetic measurements“ *Phys. Rev. B* **75**, 054517.
- [Pal04] A. Palau, T. Puig, X. Obradors, E. Pardo, C. Navau, A. Sanchez, A. Usoskin, H. C. Freyhardt, L. Fernandez, B. Holzapfel, and R. Feenstra (2004): „Simultaneous inductive determination of grain and intergrain critical current densities of $\text{YBa}_2\text{Cu}_3\text{O}_{7-x}$ coated conductors“ *Appl. Phys. Lett.* **84**, 230.
- [Par04] E. Pardo, D.-X. Chen, and A. Sanchez (2004): „Demagnetizing factors for completely shielded rectangular prisms“ *J. Appl. Phys.* **96**, 5365.
- [Sha99] D. V. Shantsev, M. R. Koblishka, Y. M. Galperin, T. H. Johansen, L. Püst, and M. Jirsa (1999): „Central Peak Position in Magnetization Loops of High- T_c Superconductors“ *Phys. Rev. Lett.* **82**, 2947.

- [Sol07] V. F. Solovyov, H. J. Wiesmann, and M. Suenaga (2007): „Critical current densities and the structural quality of 3 and 4 micrometer-thick superconducting $\text{YBa}_2\text{Cu}_3\text{O}_7$ layers synthesized using the ex situ process“ *J. Appl. Phys.* **102**.
- [Wei12] J. D. Weiss, C. Tarantini, J. Jiang, F. Kametani, A. A. Polyanskii, D. C. Larbalestier, and E. E. Hellstrom (2012): „High intergrain critical current density in fine-grain $(\text{Ba}_{0.6}\text{K}_{0.4})\text{Fe}_2\text{As}_2$ wires and bulks“ *Nat. Mater.* **11**, 682.

Chapter 7

Conclusions and Outlook

Good scientists answer questions, excellent scientists ask them.

— Unknown

This work showed that the current transport mechanism in polycrystalline Co and K doped BaFe₂As₂ is based on the physics of Josephson junctions (JJs). The weakly linked character of the grain boundaries (GBs) manifests as a hysteresis of the inter-grain current density (J_c), which is commonly explained by the field arising from the intra-grain current density (J^G), which leads to a reversed field component at the GBs. This model alone is insufficient to describe the data obtained from the samples of this study. Thus, a model was derived that combines the equations of a JJ with the statistical variation of the grain size, where J_c depends on the external applied field, the thickness of the GB, the magnetic penetration depth, J^G , and the grain size. The model showed that the hysteresis of J_c is mainly caused by J^G and the corresponding changes of the phase differences across the GB, in the investigated samples.

J_c and J^G were evaluated from scanning Hall-probe microscope measurements utilizing a novel approach, where J_c corresponds to the global field gradient in a sample, while J^G generates a local field gradient at the sample edges. The derived values are in good agreement with the model. A closer investigation indicated a transition from the physics of the Bean model to a mechanism that is governed by JJs.

The good qualitative and quantitative agreement between the measurements and the model supports its validity and calls attention to a parameter that can help to increase the operable field range of BaFe₂As₂ wires—the grain size. According to the model, the operable field range of such wires can be increased by decreasing the grain size. This predication is not limited to the investigated iron-based materials and may be of interest for other superconductors, that are governed by weakly linked GBs.

The presented model used the macroscopic parameter J_c and an averaged J^G to describe the JJ network and neglects the phase coupling over the entire system, which places certain restrictions on J_c and J^G . This could be the reason why J^G was found to change slower than expected by the critical state model. A better modeling of JJ networks could be the next step to resolve the remaining issues in weakly linked polycrystalline superconductors.

Bibliography

Books

- [Bar82] A. Barone and G. Paternò (1982): *Physics and applications of the Josephson effect*. ISBN: 9780471014690.
- [Car12] D. A. Cardwell and D. C. Larbalestier (2012): *Handbook of Superconducting Materials, 2nd Edition*. ISBN: 9781439817308.
- [Cha13] A. Charnukha (2013): *Charge Dynamics in 122 Iron-Based Superconductors*. ISBN: 9783319011929.
- [See98] B. Seeber (1998): *Handbook of Applied Superconductivity*. ISBN: 9781420050271.

Articles

- [Abr04] A. A. Abrikosov (2004): „Nobel Lecture: Type-II superconductors and the vortex lattice“ *Rev. Mod. Phys.* **76**, 975.
- [Asw10] P. M. Aswathy, J. B. Anooja, P. M. Sarun, and U. Syamaprasad (2010): „An overview on iron based superconductors“ *Supercond. Sci. Technol.* **23**, 073001.
- [Avc12] S. Avci, O. Chmaissem, D. Y. Chung, S. Rosenkranz, E. A. Goremychkin, J. P. Castellan, I. S. Todorov, J. A. Schlueter, H. Claus, A. Daoud-Aladine, D. D. Khalyavin, M. G. Kanatzidis, and R. Osborn (2012): „Phase diagram of $\text{Ba}_{1-x}\text{K}_x\text{Fe}_2\text{As}_2$ “ *Phys. Rev. B* **85**, 184507.
- [Bae02] B. J. Baelus and F. M. Peeters (2002): „Dependence of the vortex configuration on the geometry of mesoscopic flat samples“ *Phys. Rev. B* **65**, 104515.
- [Bea62] C. P. Bean (1962): „Magnetization of Hard Superconductors“ *Phys. Rev. Lett.* **8**, 250.
- [Boe03] G. Boero, M. Demierre, P.-A. Besse, and R. S. Popovic (2003): „Micro-Hall devices: performance, technologies and applications“ *Sensors and Actuators A: Physical* **106**, 314
[Proceedings of the 4th European Magnetic Sensors and Actuators Conference].
- [Bot12] L. Bottura, G. de Rijk, L. Rossi, and E. Todesco (2012): „Advanced Accelerator Magnets for Upgrading the LHC“ *IEEE Trans. Appl. Supercond.* **22**, 4002008.
- [Bra95] E. H. Brandt (1995): „The flux-line lattice in superconductors“ *Rev. Mod. Phys.* **58**, 1465.
- [Bra03] E. H. Brandt (2003): „Properties of the ideal Ginzburg-Landau vortex lattice“ *Phys. Rev. B* **68**, 054506.
- [Bul92] L. N. Bulaevskii, J. R. Clem, L. I. Glazman, and A. P. Malozemoff (1992): „Model for the low-temperature transport of Bi-based high-temperature superconducting tapes“ *Phys. Rev. B* **45**, 2545.

- [Chu09] J.-H. Chu, J. G. Analytis, C. Kucharczyk, and I. R. Fisher (2009): „Determination of the phase diagram of the electron-doped superconductor $\text{Ba}(\text{Fe}_{1-x}\text{Co}_x)_2\text{As}_2$ “ *Phys. Rev. B* **79**, 014506.
- [Cle98] J. R. Clem (1998): „Anisotropy and two-dimensional behaviour in the high-temperature superconductors“ *Supercond. Sci. Technol.* **11**, 909.
- [Dau92] M. Däumling, E. Sarnelli, P. Chaudhari, A. Gupta, and J. Lacey (1992): „Critical current of a high- T_c Josephson grain boundary junction in high magnetic field“ *Appl. Phys. Lett.* **61**, 1355.
- [Dew01] D. Dew-Hughes (2001): „The critical current of superconductors: an historical review“ *Low Temp. Phys.* **27**, 713.
- [Dur11] J. H. Durrell, C.-B. Eom, A. Gurevich, E. E. Hellstrom, C. Tarantini, A. Yamamoto, and D. C. Larbalestier (2011): „The behavior of grain boundaries in the Fe-based superconductors“ *Rev. Mod. Phys.* **74**, 124511.
- [Eis10] M. Eisterer, M. Zehetmayer, H. W. Weber, J. Jiang, J. D. Weiss, A. Yamamoto, E. E. Hellstrom, D. C. Larbalestier, N. D. Zhigadlo, and J. Karpinski (2010): „Disorder effects and current percolation in FeAs-based superconductors“ *Supercond. Sci. Technol.* **23**, 054006.
- [Eng13] J. Engelmann, V. Grinenko, P. Chekhonin, W. Skrotzki, D. V. Efremov, S. Oswald, K. Iida, R. Hühne, J. Hänisch, M. Hoffmann, F. Kurth, L. Schultz, and B. Holzapfel (2013): „Strain induced superconductivity in the parent compound BaFe_2As_2 “ *Nat. Commun.* **4**, 2877.
- [Eve88] J. E. Evetts and B. A. Glowacki (1988): „Relation of critical current irreversibility to trapped flux and microstructure in polycrystalline $\text{YBa}_2\text{Cu}_3\text{O}_7$ “ *Cryogenics* **28**, 641.
- [Fis89] M. V. Fistul' (1989): „Mesoscopic behavior of Josephson junctions with randomly disposed Abrikosov vortices“ *J. Exp. Theor. Phys.* **96**, 209
[*Zh. Eksp. Teor. Fiz.* **96**, 369].
- [Gin04] V. L. Ginzburg (2004): „Nobel Lecture: On superconductivity and superfluidity (what I have and have not managed to do) as well as on the ‚physical minimum‘ at the beginning of the XXI century“ *Rev. Mod. Phys.* **76**, 981.
- [Gon01] J. L. Gonzalez, E. V. L. Mello, M. T. D. Orlando, E. S. Yague, and E. Baggio-Saitovitch (2001): „Transport critical current in granular samples under high magnetic fields“ *Physica C* **364–365**, 347.
- [Gra10] S. Graser, P. J. Hirschfeld, T. Kopp, R. Gutser, B. M. Andersen, and J. Mannhart (2010): „How grain boundaries limit supercurrents in high-temperature superconductors“ *Nat. Phys.* **6**, 609.
- [Gur11] A. Gurevich (2011): „To use or not to use cool superconductors?“ *Nat. Mater.* **10**, 255.
- [Hay14] Y. Hayashi, A. Yamamoto, H. Ogino, J. Shimoyama, and K. Kishio (2014): „Influences of material processing on the microstructure and inter-granular current properties of polycrystalline bulk $\text{Ba}(\text{Fe},\text{Co})_2\text{As}_2$ “ *Physica C* **504**, 28
[Proceedings of the 26th International Symposium on Superconductivity].
- [Hec16] J. Hecher, T. Baumgartner, J. D. Weiss, C. Tarantini, A. Yamamoto, J. Jiang, E. E. Hellstrom, D. C. Larbalestier, and M. Eisterer (2016): „Small grains: a key to high-field applications of granular Ba-122 superconductors?“ *Supercond. Sci. Technol.* **29**, 025004.
- [Hec14] J. Hecher, M. Zehetmayer, and H. W. Weber (2014): „How the macroscopic current correlates with the microscopic flux-line distribution in a type-II superconductor: an experimental study“ *Supercond. Sci. Technol.* **27**, 075004.

- [Hen09] F. Hengstberger, M. Eisterer, M. Zehetmayer, and H. W. Weber (2009): „Assessing the spatial and field dependence of the critical current density in YBCO bulk superconductors by scanning Hall probes“ *Supercond. Sci. Technol.* **22**, 025011.
- [Hil02] H. Hilgenkamp and J. Mannhart (2002): „Grain boundaries in high- T_c superconductors“ *Rev. Mod. Phys.* **74**, 485.
- [Jos62] B. D. Josephson (1962): „Possible new effects in superconductive tunnelling“ *Phys. Lett.* **1**, 251.
- [Kam06] Y. Kamihara, H. Hiramatsu, M. Hirano, R. Kawamura, H. Yanagi, T. Kamiya, and H. Hosono (2006): „Iron-Based Layered Superconductor: LaOFeP“ *J. Am. Chem. Soc.* **128**, 10012.
- [Kam08] Y. Kamihara, T. Watanabe, M. Hirano, and H. Hosono (2008): „Iron-Based Layered Superconductor La(O_{1-x}F_x)FeAs ($x = 0.05$ – 0.12) with $T_c = 26$ K“ *J. Am. Chem. Soc.* **130**, 3296.
- [Kat11] T. Katase, Y. Ishimaru, A. Tsukamoto, H. Hiramatsu, T. Kamiya, K. Tanabe, and H. Hosono (2011): „Advantageous grain boundaries in iron pnictide superconductors“ *Nat. Commun.* **2**, 409.
- [Kei15] B. Keimer, S. A. Kivelson, M. R. Norman, S. Uchida, and J. Zaanen (2015): „From quantum matter to high-temperature superconductivity in copper oxides“ *Nature* **518**, 179.
- [Kih13] K. J. Kihlstrom, L. Fang, Y. Jia, B. Shen, A. E. Koshelev, U. Welp, G. W. Crabtree, W.-K. Kwok, A. Kayani, S. F. Zhu, and H.-H. Wen (2013): „High-field critical current enhancement by irradiation induced correlated and random defects in (Ba_{0.6}K_{0.4})Fe₂As₂“ *Appl. Phys. Lett.* **103**, 202601.
- [Kim14] Y. Kim, J. D. Weiss, E. E. Hellstrom, D. C. Larbalestier, and David N. Seidman (2014): „Evidence for composition variations and impurity segregation at grain boundaries in high current-density polycrystalline K- and Co-doped BaFe₂As₂ superconductors“ *Appl. Phys. Lett.* **105**.
- [Kun98] M. N. Kunchur and T. R. Askew (1998): „Hysteretic internal fields and critical currents in polycrystalline superconductors“ *J. Appl. Phys.* **84**, 6763.
- [Kuw89] M. Kuwabara and H. Shimooka (1989): „Grain size dependence of the critical current density in YBa₂Cu₃O_x superconductors“ *Appl. Phys. Lett.* **55**, 2781.
- [Lar01] D. C. Larbalestier, A. Gurevich, M. D. Feldmann, and A. Polyanskii (2001): „High- T_c superconducting materials for electric power applications“ *Nature* **414**, 368.
- [Lar97] D. C. Larbalestier, J. Jiang, U. P. Trociewitz, F. Kametani, C. Scheuerlein, M. Dalban-Canassy, M. Matras, P. Chen, N. C. Craig, P. J. Lee, and E. E. Hellstrom (1997): „Isotropic round-wire multifilament cuprate superconductor for generation of magnetic fields above 30 T“ *Nat. Mater.* **13**, 375.
- [Li08] G. Li, W. Z. Hu, J. Dong, Z. Li, P. Zheng, G. F. Chen, J. L. Luo, and N. L. Wang (2008): „Probing the Superconducting Energy Gap from Infrared Spectroscopy on a Ba_{0.6}K_{0.4}Fe₂As₂ Single Crystal with $T_c = 37$ K“ *Phys. Rev. Lett.* **101**, 107004.
- [Lik79] K. K. Likharev (1979): „Superconducting weak links“ *Rev. Mod. Phys.* **51**, 101.
- [Lis97] F. A. List, D. M. Kroeger, and V. Selvamanickam (1997): „Hysteresis of the transport critical current of (Tl,Pb)-(Sr,Ba)-Ca-Cu-O and Bi-Sr-Ca-Cu-O conductors: effects of temperature and magnetic field“ *Physica C* **275**, 220.
- [Lon35] F. London and H. London (1935): „The Electromagnetic Equations of the Supraconductor“ *Proc. R. Soc. A* **149**, 71.

- [Ma08] F. Ma and Z.-Y. Lu (2008): „Iron-based layered compound LaFeAsO is an antiferromagnetic semimetal“ *Phys. Rev. B* **78**, 033111.
- [Mar94] I. Martini, J. Bechtold, M. Majoros, V. Ottoboni, J.-C. Vallier, and S. Zannella (1994): „Superconducting properties of multilayered Bi(Pb)-2223/Ag tapes“ *Supercond. Sci. Technol.* **7**, 24.
- [McH89] M. E. McHenry, M. P. Maley, and J. O. Willis (1989): „Systematics of transport critical-current-density hysteresis in polycrystalline Y-Ba-Cu-O“ *Phys. Rev. B* **40**, 2666.
- [Mei33] W. Meißner and R. Ochsenfeld (1933): „Ein neuer Effekt bei Eintritt der Supraleitfähigkeit“ *Naturwissenschaften* **21**, 787.
- [Min14] S. Minniberger, F. Diorico, S. Haslinger, C. Hufnagel, C. Novotny, N. Lippok, J. Majer, C. Koller, S. Schneider, and J. Schmiedmayer (2014): „Magnetic conveyor belt transport of ultracold atoms to a superconducting atomchip“ *Appl. Phys. B* **116**, 1017.
- [Min99] R. G. Mints and V. G. Kogan (1999): „Josephson junction between anisotropic superconductors“ *Phys. Rev. B* **60**, 1394.
- [Mul94] K.-H. Müller, C. Andrikidis, H. K. Liu, and S. X. Dou (1994): „Intergranular and intragranular critical currents in silver-sheathed Pb-Bi-Sr-Ca-Cu-O tapes“ *Phys. Rev. B* **50**, 10218.
- [Ni10] B. Ni, J. Ge, M. Kiuchi, E. S. Otabe, Z. Gao, L. Wang, Y. Qi, X. Zhang, and Y. Ma (2010): „Critical current characteristics and history dependence in superconducting SmFeAsOF bulk“ *JPCS* **234**, 012028.
- [Ni11] B. Ni, J. Ge, Y. Tanaka, E. S. Otabe, M. Kiuchi, T. Matsushita, Z. Gao, L. Wang, Y. Qi, X. Zhang, and Y. Ma (2011): „Estimation of Critical Current Densities in Polycrystalline Sr_{0.6}K_{0.4}Fe₂As₂ Superconductors“ *IEEE Trans. Appl. Supercond.* **21**, 2862.
- [Pag10] J. Paglione (2010): „High-temperature superconductivity in iron-based materials“ *Natur Phys.* **6**, 645.
- [Pal07] A. Palau, T. Puig, X. Obradors, and Ch. Jooss (2007): „Simultaneous determination of grain and grain-boundary critical currents in YBa₂Cu₃O₇-coated conductors by magnetic measurements“ *Phys. Rev. B* **75**, 054517.
- [Pal04] A. Palau, T. Puig, X. Obradors, E. Pardo, C. Navau, A. Sanchez, A. Usoskin, H. C. Freyhardt, L. Fernandez, B. Holzapfel, and R. Feenstra (2004): „Simultaneous inductive determination of grain and intergrain critical current densities of YBa₂Cu₃O_{7-x} coated conductors“ *Appl. Phys. Lett.* **84**, 230.
- [Par04] E. Pardo, D.-X. Chen, and A. Sanchez (2004): „Demagnetizing factors for completely shielded rectangular prisms“ *J. Appl. Phys.* **96**, 5365.
- [Pol96] A. A. Polyanskii, A. Gurevich, A. E. Pashitski, N. F. Heinig, R. D. Redwing, J. E. Nordman, and D. C. Larbalestier (1996): „Magneto-optical study of flux penetration and critical current densities in [001] tilt YBa₂Cu₃O_{7-δ} thin-film bicrystals“ *Phys. Rev. B* **53**, 8687.
- [Put10] M. Putti, I. Pallecchi, E. Bellingeri, M. R. Cimberle, M. Tropeano, C. Ferdeghini, A. Palenzona, C. Tarantini, A. Yamamoto, J. Jiang, J. Jaroszynski, F. Kametani, D. Abramov, A. Polyanskii, J. D. Weiss, E. E. Hellstrom, A. Gurevich, D. C. Larbalestier, R. Jin, B. C. Sales, A. S. Sefat, M. A. McGuire, D. Mandrus, P. Cheng, Y. Jia, H. H. Wen, S. Lee, and C. B. Eom (2010): „New Fe-based superconductors: properties relevant for applications“ *Supercond. Sci. Technol.* **23**, 034003.
- [Rot08] M. Rotter, M. Tegel, and D. Johrendt (2008): „Superconductivity at 38 K in the Iron Arsenide (Ba_{1-x}K_x)Fe₂As₂“ *Phys. Rev. Lett.* **101**, 107006.

- [Sef08] A. S. Sefat, R. Jin, M. A. McGuire, B. C. Sales, D. J. Singh, and D. Mandrus (2008): „Superconductivity at 22 K in Co-Doped BaFe₂As₂ Crystals“ *Phys. Rev. Lett.* **101**, 117004.
- [Sha99] D. V. Shantsev, M. R. Koblishka, Y. M. Galperin, T. H. Johansen, L. Püst, and M. Jirsa (1999): „Central Peak Position in Magnetization Loops of High- T_c Superconductors“ *Phys. Rev. Lett.* **82**, 2947.
- [Shi13] Y. Shiohara, M. Yoshizumi, Y. Takagi, and Izumi T. (2013): „Future prospects of high- T_c superconductors-coated conductors and their applications“ *Physica C* **484**, 1.
- [Sol07] V. F. Solovyov, H. J. Wiesmann, and M. Suenaga (2007): „Critical current densities and the structural quality of 3 and 4 micrometer-thick superconducting YBa₂Cu₃O₇ layers synthesized using the ex situ process“ *J. Appl. Phys.* **102**.
- [Svi92] V. M. Svistunov and A. I. D'yachenko (1992): „A layered structure as a Josephson medium“ *Supercond. Sci. Technol.* **5**, 98.
- [Vin90] V. M. Vinokur and A. E. Koshelev (1990): „Collective pinning of soliton lattice in Josephson junctions“ *J. Exp. Theor. Phys.* **70**, 547
[*Zh. Eksp. Teor. Fiz.* **97**, 976].
- [Wei13] J. D. Weiss, J. Jiang, A. A. Polyanskii, and E. E. Hellstrom (2013): „Mechanochemical synthesis of pnictide compounds and superconducting Ba_{0.6}K_{0.4}Fe₂As₂ bulks with high critical current density“ *Supercond. Sci. Technol.* **26**, 074003.
- [Wei12] J. D. Weiss, C. Tarantini, J. Jiang, F. Kametani, A. A. Polyanskii, D. C. Larbalestier, and E. E. Hellstrom (2012): „High intergrain critical current density in fine-grain (Ba_{0.6}K_{0.4})Fe₂As₂ wires and bulks“ *Nat. Mater.* **11**, 682.
- [Wen97] H. Wen, T. J. Denison, R. W. Singerman, and R. S. Balaban (1997): „The Intrinsic Signal-to-Noise Ratio in Human Cardiac Imaging at 1.5, 3, and 4 T“ *J. Magn. Reson.* **125**, 65.
- [Wie92] H. P. Wiesinger, F. M. Sauerzopf, and H. W. Weber (1992): „On the calculation of J_c from magnetization measurements on superconductors“ *Physica C* **203**, 121.
- [Xu90] M. Xu, D. Shi, and R. F. Fox (1990): „Generalized critical-state model for hard superconductors“ *Phys. Rev. B* **42**, 10773.
- [Yan70] I. K. Yanson (1970): „Effect of Fluctuations on the Dependence of the Josephson Current on the Magnetic Field“ *J. Exp. Theor. Phys.* **31**, 800
[*Zh. Eksp. Teor. Fiz.* **58**, 1497].
- [Zeh09] M. Zehetmayer (2009): „Simulation of the current dynamics in superconductors: Application to magnetometry measurements“ *Phys. Rev. B* **80**, 104512.
- [Zeh04] M. Zehetmayer, M. Eisterer, J. Jun, S. M. Kazakov, J. Karpinski, B. Birajdar, O. Eibl, and H. W. Weber (2004): „Fishtail effect in neutron-irradiated superconducting MgB₂ single crystals“ *Phys. Rev. B* **69**, 054510.
- [Zhi08] R. Zhi-An, L. Wei, Y. Jie, Y. Wei, S. Xiao-Li, L. Zheng-Cai, C. Guang-Can, D. Xiao-Li, S. Li-Ling, Z. Fang, and Z. Zhong-Xian (2008): „Superconductivity at 55 K in Iron-Based F-Doped Layered Quaternary Compound Sm(O_{1-x}F_x)FeAs“ *Chin. Phys. Lett.* **25**, 2215.

Curriculum Vitae

Personal

<i>Full name</i>	Johannes Matthias Hecher
<i>Date of birth</i>	January 1 st , 1987
<i>Citizenship</i>	Austria

Education

DIPL.-ING.	2012	Fakultät für Physik, Technischen Universität Wien Diploma thesis: „Vortex lattice study of pristine and irradiated niobium deselenid by scanning tunneling microscopy“
B.Sc.	2010	Fakultät für Physik, Technischen Universität Wien
MATURA	2005	Bundesrealgymnasium, Gröhmühlgasse Wiener Neustadt
	1998–2005	Bundesrealgymnasium (lower and secondary education) Gröhmühlgasse Wiener Neustadt
	1994–1998	Volksschuhle (primary education) St.Egyden am Steinfeld

Publications

J. Hecher, M. Zehetmayer, and H. W. Weber (2014): „How the macroscopic current correlates with the microscopic flux-line distribution in a type-II superconductor: an experimental study“ *Supercond. Sci. Technol.* **27**, 075004

J. Hecher, T. Baumgartner, J. D. Weiss, C. Tarantini, A. Yamamoto, J. Jiang, E. E. Hellstrom, D. C. Larbalestier, and M. Eisterer (2016): „Small grains: a key to high-field applications of granular Ba-122 superconductors?“ *Supercond. Sci. Technol.* **29**, 025004